Studies of the Pulsar Wind Nebula Population observed with H. E. S. S.

Diplomarbeit

von

Michael Mayer

Erlangen Centre for Astroparticle Physics
Physikalisches Institut 2
Lehrstuhl für Physik
Friedrich-Alexander-Universität
Erlangen-Nürnberg

1. Gutachter: Prof. Dr. Christian Stegmann
2. Gutachter: Prof. Dr. Jörn Wilms

1. Dezember 2010

Abstract

The topic of this thesis is the non-thermal, very high energy γ-ray (> 0.1TeV) radiation from Pulsar Wind Nebulae (PWNe). The basis of this work are data, taken by the H.E.S.S. experiment, which is the best suited detector for the observation of extended galactic sources in this energy range. After six years of data-taking, H. E. S. S. has detected a large sample of PWN and PWN candidates. This sample allows population studies leading to a better understanding of the general features of TeV emitting PWNe. While more than 1800 pulsars are known from observations in the radio and X-ray regime, the investigations in this thesis reveal that only the youngest and those with the highest period derivative, are able to generate TeV nebulae. Great emphasis has been placed on the detailed analysis of the H. E. S. S. data. Using the currently most advanced analysis method (Model++), the spectral and morphological evolutions of all sources have been determined and compared with each other. The thesis also comprises the development of a simple model, describing the spectral evolution of a PWN with age. Systematics, performance and reliability of the model are discussed in detail. Fitting this model to the H. E. S. S. data allows to draw conclusions on features of the pulsar which are not directly observable, e.g. the initial period. Most of the considered sources are well described by the model, providing physically reasonable values. In cases where the model fails to describe the observed spectra, potential nonconformities are discussed and improvement opportunities for the model are presented. Moreover, the model is used to perform long-term simulations of the spectral evolution of PWNe. These simulations show that one of the widely spread identification criteria for a TeV PWN, i.e. the claim that the γ-ray luminosity must not exceed the present spin-down luminosity of the pulsar, must be rejected. Finally, it is examined whether the PWN scenario can be excluded for some of the candidates based on the results of the modeling.

Kurzfassung

In der vorliegenden Diplomarbeit wird die nicht-thermische, hochenergetische γ-Strahlung ($> 0.1\,\mathrm{TeV}$) von Pulsarwindnebeln (PWN) behandelt. Grundlage dieser Arbeit sind Daten des H. E. S. S. Experiments, das in diesem Energiebereich geeignetste Teleskopsystem zur Beobachtung von ausgedehnten galaktischen Quellen. In den letzten sechs Jahren hat H. E. S. S. eine große Anzahl von PWN und PWN-Kandidaten im TeV-Bereich entdeckt. Durch Populationsstudien ist es möglich, diese Objekte und ihre allgemeinen Eigenschaften besser zu verstehen. Von den mehr als 1800 durch Radio- und Röntgenbeobachtungen bekannten Pulsaren, erzeugen nur die besonders jungen und diejenigen mit einer hohen Änderungsrate ihrer Periode einen signifikanten TeV-Nebel. Ein Schwerpunkt dieser Arbeit ist die detaillierte Analyse der H. E. S. S.-Daten, welche mit der derzeit modernsten Analysemethode (Model++) durchgeführt wird. Die spektralen und morphologischen Entwicklungen können dadurch bestimmt und miteinander verglichen werden. Diese Arbeit umfasst außerdem die Erarbeitung eines Modells, welches die spektrale Entwicklung eines PWN beschreibt. Die Funktionsweise, Systematik sowie Vertrauenswürdigkeit der Ergebnisse dieses Modells werden genau diskutiert. Die freien Parameter des Modells werden an die H. E. S. S.-Daten angepasst. Dies ermoglicht es auf Eigenschaften des Pulsars rückzuschließen, die nicht beobachtbar sind, wie z.B. die Anfangsperiode. Ein Großteil der untersuchten Quellen wird durch das Modell mit physikalisch sinnvollen Parametern gut beschrieben. Wenn die Modellberechnungen scheitern das beobachtete Spektrum zu reproduzieren, werden die Ergebnisse diskutiert und Verbesserungsmöglichkeiten aufgezeigt. Des Weiteren wird mit dem Modell das Langzeitverhalten von PWN simuliert. Diese Berechnungen zeigen, dass ein weit verbreitetes Kriterium zur Identifikation von PWN nicht länger aufrecht erhalten werden kann. Dieses Kriterium besagt, dass der gemessene Energiefluss der Quelle nicht größer sein darf, als der Rotationsenergieverlust des Pulsares an sich. Schließlich werden mögliche PWN-Szenarien für PWN-Kandidaten auf Grundlage der Modellergebnisse diskutiert.

Contents

1. Introduction

During the last century our knowledge of the Universe and its energetics increased with imposing speed. Some discoveries have strongly contributed to this field of research. A very important one was made by Victor Hess, an Austrian physicist, in 1912 (Fig. 1.1). He measured an increase of ionization in the air with height over ground. It was a contradiction to the opinion that radioactivity from the ground is solely responsible for the atmosphere's ionization. He concluded that the radiation causing this ionization originates from the sky. Afterwards Robert Millikan coined the term "cosmic rays". Another fundamental discovery was made by Jocelyn Bell Burnell and Anthony Hewish in 1967. While studying compact radio sources like distant galaxies, the Ph.D. student Burnell (Fig. 1.1) discovered a periodic signal from a certain region in the sky returning every 1.338 seconds (Hewish et al. 1968). First, the signal was assumed to be man-made due to its astonishingly exact periodicity. A distance estimate resulted in a position within our Galaxy but outside the solar system. No astrophysical source class producing such a signal was known at that time. The guess of Burnell and Hewish was an extraterrestrial civilization trying to get in contact with the Earth. For that reason the source was nicknamed LGM1 (Little Green Man 1). As they continued their measurements, similar signals with different pulsations and from other directions in the sky were discovered. Moreover, the received data showed no evidence for a short-term variability of Doppler-shifts which would be produced by radiation emitted from a planet moving around its star. Therefore the hypothesis of extraterrestrial intelligence was dismissed.

Figure 1.1.: *Left*: Victor Hess in his hydrogen balloon[1] (1912). *Right*: Jocelyn Bell Burnell in front of the radio telescope[2] (1967).

A few years earlier Baade & Zwicky (1934) had already postulated the existence of neutron stars assuming a fast-rotating compact object as remnant of a dying star. Due to its small and dense structure, a representative of this class of objects could produce such high frequency pulses generated by a fast rotation speed. Soon after Burnell and Hewish detected pulsed signals the idea of a fast-rotating neutron star powering this emission was established

[1] `http://www.astroteilchenphysik.de`
[2] `http://www.nmsi.ac.uk/`

calling the object pulsar, derived from "pulsating radio source". Hewish received the Nobel Prize for his work in 1974.

Serendipitous discoveries like cosmic rays or pulsars motivate scientists to continue astrophysical research. The technical progress during the last decades, increasing sensitivity and resolution of detectors, enabled a more detailed study of the universe respectively its sources of high-energy cosmic rays. Fast calculating computers are able to support the data analysis and accelerate the application of complex models describing the nature of astrophysical processes appropriately.

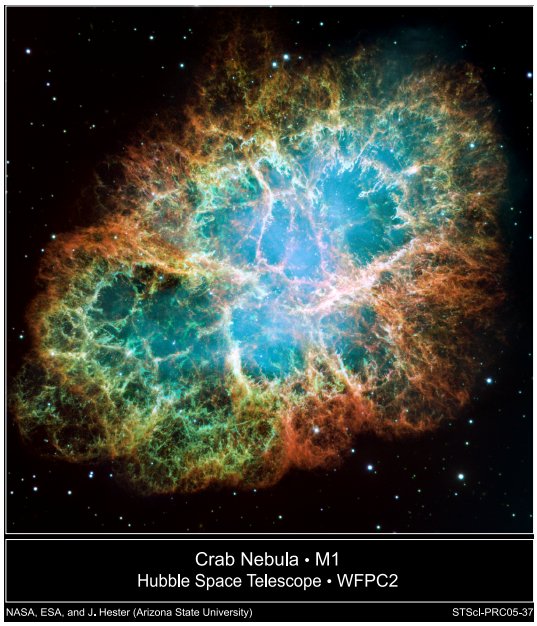

Figure 1.2.: The Crab Nebula in visible light shows an impressive structure. The energy source of this emission is the Crab Pulsar in its center but too small to see. Image taken by the Hubble Space Telescope (Image Credit: NASA, ESA, J. Hester and A. Loll (Arizona State University)).

Many astrophysical objects have already been discovered in several wavelengths. Detailed observations of e.g. fast-rotating neutron stars revealed emission in spectral ranges from the radio band up to very high energy (VHE) γ-rays. The most famous representative of this particular class of sources is the Crab Pulsar (Fig. 1.2) whose nebula is visible in many wavelengths. Its birth was seen in 1054 by Chinese astronomers observing a bright explosion of an old star. Today, the nebula has a diameter of about ten light years. Its energy source, responsible for the bright emission, is the Crab Pulsar located in the center. Objects like this example are called Pulsar Wind Nebula. Since 1967 about 1880 pulsars of different ages, periods and energetics have been discovered in the Milky Way or in nearby galaxies. Some of them, like the Crab Pulsar, produce nebulae emitting γ-rays up to 100 TeV. Imaging Air Cerenkov Telescopes (IACT), such as H. E. S. S., are suitable to detect this VHE radiation from these and other objects. Fig. 1.3 shows the spatial distribution of the different source classes detected with the H. E. S. S. telescopes. Beside unidentified sources, Pulsar Wind Nebulae (henceforth PWN) are the most common γ-ray emitting objects in the Galactic Plane. After six years of data-taking with H. E. S. S. enough PWNe are accessible in the VHE regime

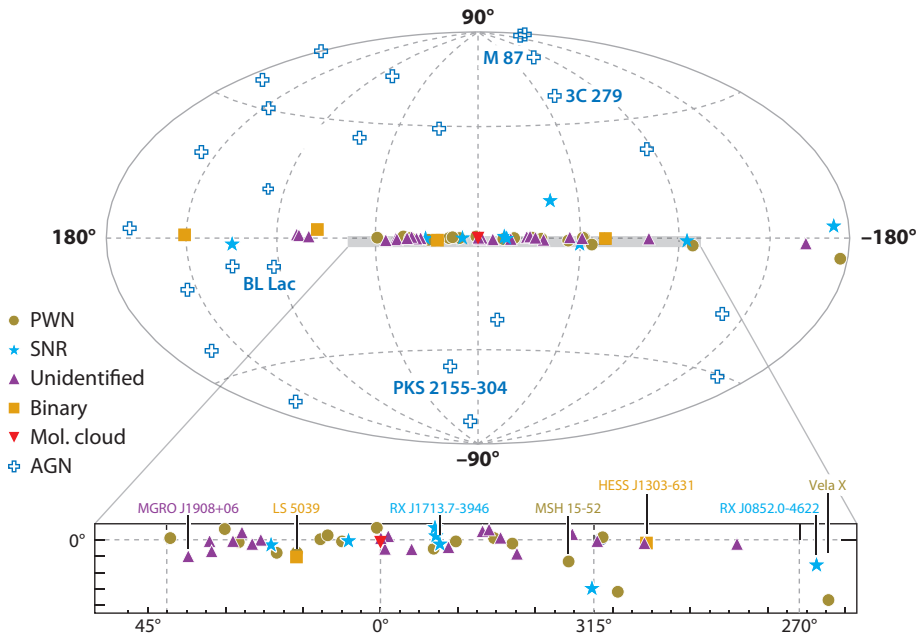

Figure 1.3.: TeV sky map in galactic coordinates. The indicated sources were detected with the H. E. S. S. experiment in the VHE regime. Figure adopted from Hinton & Hofmann (2009).

to perform population studies in order to understand their physics and evolutionary behavior.

This thesis will reflect on pulsars and the production of PWNe in general with a special focus on the most energetic radiation (Chap. 2), first. Subsequently, Chap. 3 will give a brief introduction on the detection technique of the H. E. S. S. telescopes and on data analysis. The sources contributing to the population of PWNe are presented in Chap. 4, which also points out some facts about the properties of pulsars generating TeV nebulae. In order to understand the evolutionary behavior of the PWNe, Chap. 5 introduces a simple time-dependent model attempting to describe the spectral evolution of a nebula produced by a fast-rotating neutron star. Subsequent chapters compare the results of this model to the measured data and discuss some predictions for the spectral evolution of PWNe.

2. Pulsar Wind Nebulae (PWNe)

Stars with sufficiently large mass which have burnt all their material to maintain the fusion processes will explode in bright supernovae. Such happenings are clearly visible in all spectral wave bands. These supernova events are rare on human timescales. About three stars will collapse during one century in the Milky Way. A recently detected supernova in a nearby galaxy can be seen in Figure 2.1. It is assumed that a pulsar was formed during the core collapse. First, this Chapter will reflect on pulsars and their evolution in general. Afterwards an overview of the giant population of already detected pulsars is given. Finally, the mechanisms of forming PWNe are explained.

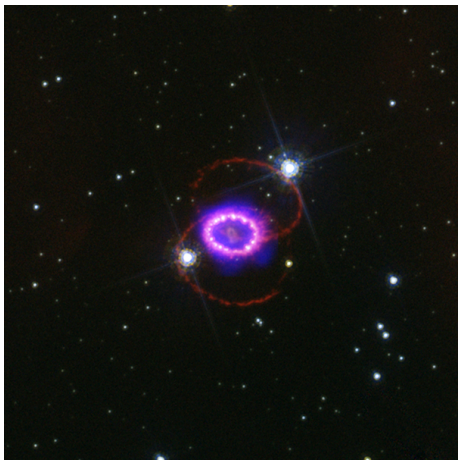

Figure 2.1.: A multiwavelength image of the supernova SN 1987A in the Large Magellanic Cloud (LMC) composed of optical data by the Hubble Space Telescope (red and white) and of a view in X-rays by the Chandra Observatory (blue and purple). The visible region has a diameter of 12 arc min. (Image Credit: X-ray: NASA/CXC/PSU/S.Park & D.Burrows., Optical: NASA/STScI/CfA/P.Challis)

2.1. Formation of pulsars

Neutron stars are the remnants of old stars whose nuclear fusion processes stopped. Either the star's core temperature was too low to initiate the burning of the element synthesized by the previous reactions or there was only iron left in the core. Nuclear fusion of iron or heavier elements does not release energy. Thus the radiation pressure from the inside of the star ceases and the whole matter will collapse under its own gravitational pressure. The inner core is compressed to a small compact object while the outer envelope is blown away in the form of a shell. An increasing pressure inside the core leads to very high densities inducing the inverse β-decay

$$\mathrm{p} + \mathrm{e}^- \longrightarrow \mathrm{n} + \nu_\mathrm{e}, \tag{2.1}$$

forming a neutron and neutrino by the interaction of electron and proton. The remaining neutrons are compressed to a compact object with about 20 km in diameter. A further and more detailed review of the formation and structure of pulsars is given by Lyne & Graham-Smith (2006). A rotating star decreasing its radius, e.g. due to a collapse, gains rotation speed by the conservation of its angular momentum. Therefore periods of about 10 ms and smaller are possible and have already been measured for neutron stars. Compressed to a small region, the magnetic flux is also conserved reaching values of up to 10^8 T and higher. These extreme conditions are typical for neutron stars after their birth. To form such an object the progenitor star must at least have 1.4 solar masses (Chandrasekhar 1931). Otherwise the gravity is not strong enough, forming a white dwarf which still consists of normal atoms. Should the compact remnant be heavier than about 3 solar masses, the star's gravity is too strong. The neutron star will continue collapsing to a black hole.

The pulsed emission detected by Jocelyn Bell Burnell and Anthony Hewish in 1967 has its origin in a misalignment of the rotation axis from the magnetic dipole axis of the neutron star, as illustrated in Fig. 2.2. To understand the evolution of these pulses and the whole energetics of a pulsar it is necessary to study the whole population of these objects. Therefore an introduction to the evolution of a pulsar is given first.

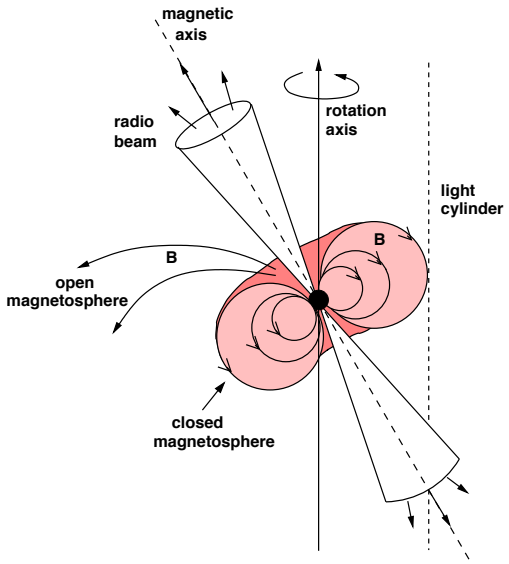

Figure 2.2.: Schematic view of a pulsar. In a general case the rotation axis and magnetic axis are misaligned. The magnetic field moves through the ambient medium and induces synchrotron radiation from particles located there. The pulsar can be detected if the light cone, respectively the radio beam sweeps across the Earth. Figure adopted from S. Carrigan (2007).

2.1.1. Spin-down evolution

The period P of a pulsar is very constant. However, long-term observations revealed that the period increases slowly with time. The period derivative $\dot{P} = {}^{\mathrm{d}P}/_{\mathrm{d}t}$, e.g. for the Crab Pulsar is in the order of $10^{-13}\,\mathrm{s\,s^{-1}}$. Thus, pulsars are constantly losing rotational energy. The amount

of energy released from a pulsar can be calculated by knowing P and $\dot{P}$. Explanations in this Chapter are based on Gaensler & Slane (2006). The rotational energy of any solid object is given by the following equation:

$$E_{rot} = \frac{1}{2} I \omega^2 = \frac{2\pi^2 I}{P^2}, \tag{2.2}$$

where I is the moment of inertia. Assuming a spherical object with a mass of $1.4\,\mathrm{M}_\odot$ and a radius of 10 km, the moment of inertia can be estimated as $I = 10^{45}\,\mathrm{g\,cm^{-2}}$. The energy output of the pulsar, the so-called "spin-down luminosity" $\dot{E}$ is then defined as

$$\dot{E} = -\frac{\mathrm{d}E_{rot}}{\mathrm{d}t} = 4\pi^2 I \frac{\dot{P}}{P^3}. \tag{2.3}$$

The values of approximated $\dot{E}$ range from $3 \cdot 10^{28}\,\mathrm{erg\,s^{-1}}$ for PSR J2144−3933 up to $4.9 \cdot 10^{38}\,\mathrm{erg\,s^{-1}}$ for PSR J0537−6910. Gaensler & Slane (2006) introduced the spin-down of a pulsar with birth period P_0 as a differential equation

$$\dot{\omega} = -k\omega^n, \tag{2.4}$$

where n is the "braking index" and $\omega = {}^{2\pi}/_{P}$. Under the assumption that k is a constant, $n \neq 1$ and $\dot{n} = 0$, the age of the system is defined as

$$\tau = \frac{P}{(n-1)\dot{P}} \left(1 - \left(\frac{P_0}{P} \right)^{n-1} \right). \tag{2.5}$$

Only for a few pulsars the braking index has been measured. These values fall in the range from $n = 1.4$ for the Vela Pulsar (PSR J0835−4510) to $n = 2.84$ for MSH 15−52 (PSR J1513−5908). For the rest of the population $n = 3$ is assumed (Gaensler & Slane 2006). This value corresponds to spin down via magnetic dipole radiation. Taking into account that $P_0 \ll P$, Eq. 2.5 reduces to an expression which is called "characteristic age" of the pulsar,

$$\tau_c \equiv \frac{P}{2\dot{P}}\,. \tag{2.6}$$

This formula is just an indicator for the real age because P_0 is often not much smaller than P. Therefore τ_c will often represent an overestimation of the true age. Suppose a pulsar was born with an initial spin-down luminosity $\dot{E}_0$. Than $\dot{E}$ evolves with time as

$$\dot{E}(t) = \dot{E}_0 \left(1 + \frac{t}{\tau_0} \right)^{-\frac{n+1}{n-1}}, \tag{2.7}$$

where τ_0 is the initial spin-down timescale and given by

$$\tau_0 = \frac{P_0}{(n-1)\dot{P}_0} = \frac{2\tau_c}{n-1} - \tau = \frac{2\tau_c}{n-1} \left(\frac{P_0}{P} \right)^{n-1}. \tag{2.8}$$

The pulsar located in the Crab Nebula with a known braking index of $n = 2.5$ and an estimated initial period $P_0 \approx 18\,\mathrm{ms}$, e.g. has a spin-down timescale of about 0.7 kyr.

Properties of the spin-down evolution of a pulsar were shown in this Section. Assumptions like a time-independent braking index were necessary for further calculations. Studying the population of TeV nebulae induced by fast rotating neutron stars requires investigations on the entire sample of already discovered pulsars first.

2.1.2. Appearance and distribution of pulsars

Lots of pulsars have been discovered, representing a population which might be distributed all over the universe. Measurements of P, $\dot{P}$ and the pulsar's position in the sky allow to give an overview on some characteristic parameters of the sample. Fast rotating neutron stars appear in regions where supernovae are possible, i.e. where stars are located. The densest region of stars surrounding the Earth is the galactic plane and the Large and Small Magellanic Clouds (LMC and SMC).

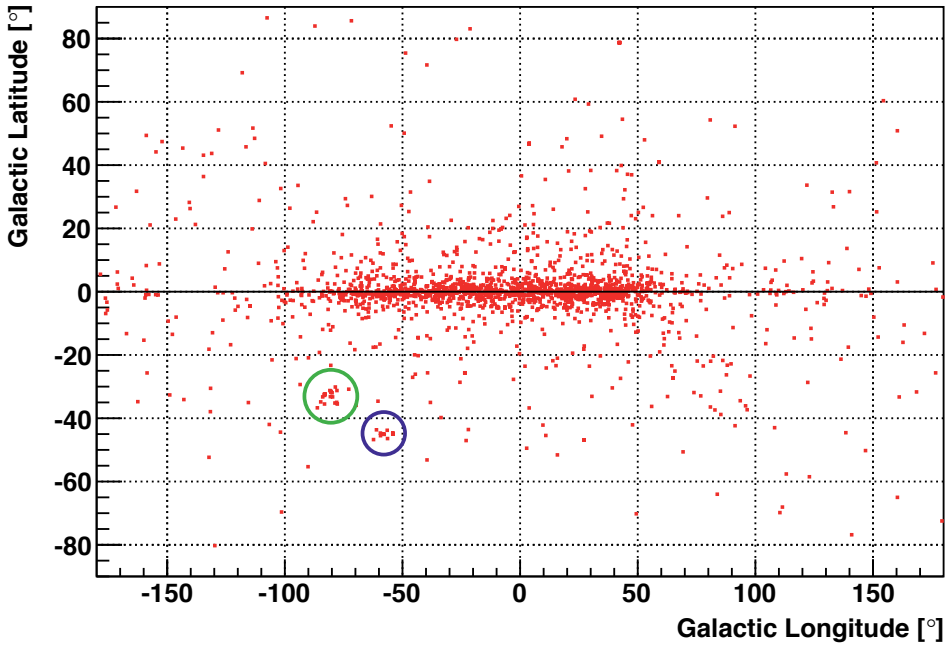

Figure 2.3.: Spatial distribution of the pulsars in galactic coordinates. Obviously many of them are located in the Galactic Plane. Note: The Galactic Longitudes within $[180°, 360°]$ have been mapped to $[-180°, 0°]$ for the purpose of visualization. Marked with a circle are the nearby galaxies LMC (green) and the SMC (blue).

Fig. 2.3 shows the pulsars clustering similar to the matter distribution. Of course the plot shows just a small selection of the whole population, due to technically limited instruments which only detect the nearest and strongest pulsars. Besides, the Earth has to be located inside the rotating light cone otherwise it is not possible to measure the pulsed signal.
To visualize evolutionary states one can investigate parameters changing with time. There are no long-term observations of pulsars which allow to follow these objects on large timescales. Therefore a parameter with respect to the pulsars' age may give a snapshot of its temporal evolution. The best existing estimate for the age of a pulsar is the characteristic age (defined in Eq. 2.6) because the braking index and the initial period, required to determine the true age, are unknown in nearly all cases. The values of the pulsars are taken from the ATNF Pulsar Database (Manchester et al. 2005). Neutron stars can exist as solitary objects and also in binary systems with companion stars. Since the latter show a different behavior, e.g. their period decreases due to accretion, they are excluded from the sample.

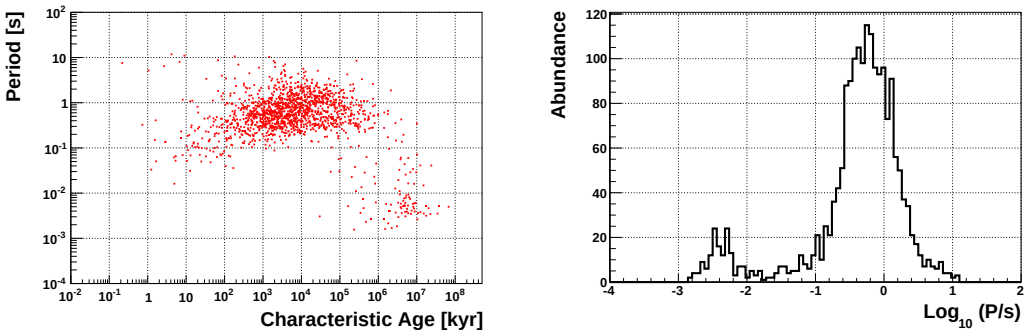

Figure 2.4.: The left image shows the development of the periods with age, pointing out a slight increase over time. Their distribution (shown right) is peaked at about 0.5 s.

Most known pulsars rotate with periods smaller than 1 s (see Fig. 2.4). Binaries with undiscovered companion stars should be responsible for the second maximum in the distribution at $10^{-2.5}\,\mathrm{s} \approx 3\,\mathrm{ms}$. Old, but still fast-rotating pulsars also belong to such binary systems. Apart from that, the periods show a slight increase with their age corresponding to the spin-down evolution.

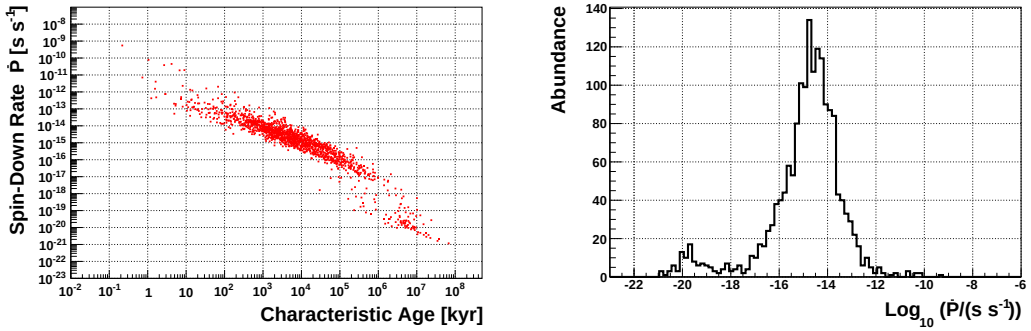

Figure 2.5.: The left figure shows the period derivative plotted over the characteristic age. Higher aged pulsars have a smaller $\dot{P}$ corresponding to a decrease in the energy output. Wrong classified binaries still contributing to this sample might be responsible for the jump at $10^6\,\mathrm{kyr}$. A distribution of the $\dot{P}$ values is illustrated right. A prominent peak at $10^{-15}\,\mathrm{s\,s^{-1}}$ can be recognized.

The distribution of the period derivatives has a sharp maximum in the order of $10^{-15}\,\mathrm{s\,s^{-1}}$ (see Fig. 2.5). This pulsar parameter decreases with time but is stronger correlated to the characteristic age as the periods themselves. Small values of $\dot{P}$ for unresolved binary pulsars still contributing to this sample lead to a probable overestimation of the age. The spin-down luminosity is derived from the period and period derivative (Eq. 2.3). Its behavior with respect to the pulsars age is shown in Fig. 2.6 confirming Eq. 2.7 as a good approximation for the temporal evolution of many pulsars. Most of the estimated spin-down luminosities fall in the range between $10^{30}\,\mathrm{erg\,s^{-1}}$ and $10^{34}\,\mathrm{erg\,s^{-1}}$.

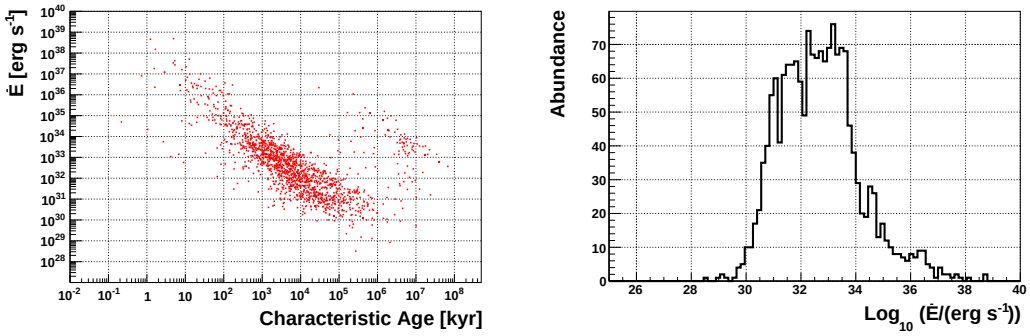

Figure 2.6.: The Spin-down luminosity over the characteristic age is shown left. A decrease of the energy output with age is clearly visible as described in Eq. 2.7. The high aged objects with a significantly higher $\dot{E}$ than the rest of the sample might be binary pulsars whose companion is not detected yet. The distribution of the spin-down luminosities (right) shows a maximum at about $10^{33}\,\mathrm{erg\,s^{-1}}$. Smaller values may occur more often than presented here, but they are more unlikely to be detected.

This section reflected the theoretical and experimental knowledge of the evolution of pulsars. The population of all discovered pulsars was investigated with respect to their temporal evolution. It has been pointed out that the periods increase for pulsars at higher ages. However, the period derivatives are decreasing with time. Combining both effects reveals a strongly decreasing energy output with respect to the pulsar's characteristic age. The amount of energy released by the fast-rotating neutron star during its life powers highly energetic phenomena, e.g. like the strong magnetic field or relativistic particles, as discussed in the next Section.

2.2. Pulsars powering high energy particles

The emphasis of this thesis is VHE radiation from pulsars and their surroundings. The origin of this emission are high energy particles accelerated by or near the central energy source. In fact, processes regarding the acceleration of particles up to some TeV and beyond are not well understood. However, diffusive shock acceleration is assumed to dominate the energy gain of the particles. Due to irregularities in the magnetic fields, so called "magnetic mirrors" are formed, moving with a velocity V. A low energy particle with energy E, crossing a section of many mirrors, gets reflected several times. The energy ΔE gained by each reflection is given by

$$\frac{\Delta E}{E} = \frac{V}{c}. \tag{2.9}$$

Having a non-negligible escape probability from the magnetic accelerators the particles show an energy spectrum with power law shape

$$\frac{\mathrm{d}N(E)}{\mathrm{d}E} \propto E^{-p}, \tag{2.10}$$

with an index of $p \approx 2$. This mechanism is called first order Fermi acceleration (Fermi 1949) and can explain many measured energy spectra in high energy astrophysics. Relativistic

particles in the surroundings of a pulsar are forming the Pulsar Wind. The maximum energy for an accelerated lepton at a Vela-like pulsar is about 350 TeV, depending on the Wind parameters (de Jager & Djannati-Ataï 2009). Fig. 2.7 shows an image of the Crab Nebula.

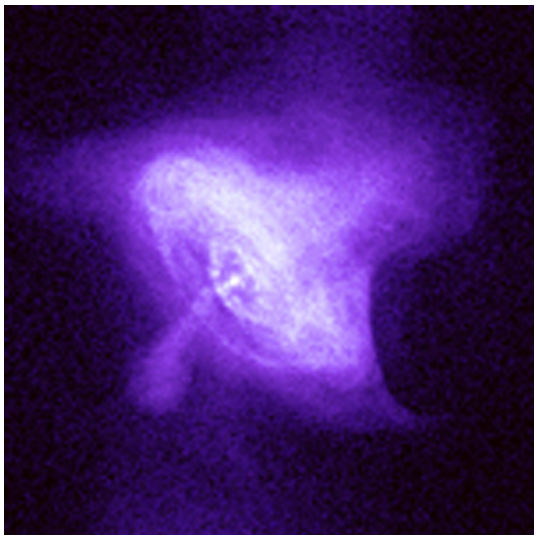

Figure 2.7.: A close look at the Crab Pulsar in X-rays. Around the pulsar the termination shock, induced by the fast rotation, can be seen. Also, there are jets coming out of the polar caps of the pulsar. Image taken by the Chandra X-ray observatory. (Image Credit: NASA/CXC/SAO)

The rotating region around the pulsar is called termination shock. Particles get accelerated up to highly relativistic energies there. An extensive review of the formation of such a shock is given by Gaensler & Slane (2006). Propagating to the outer edges of the Pulsar Wind the particles can not keep their energy. The next Section will introduce the main particle and energy loss mechanism inside this relativistic bubble.

2.3. Cooling effects on the particle spectrum

Particles injected into the Pulsar Wind are not moving freely without interacting with their surroundings. There are physical processes which force them to lose energy in different ways.

Diffusion, escape losses High energy particles do not stay for a long time in the Pulsar Wind. Either they are cooled by energy losses or they just diffuse far away from their origin. The timescale on which a lepton covers the distance of one Pulsar Wind radius is given by (Zhang et al. 2008)

$$\tau_{\mathrm{esc}} = 34 \cdot \left[\frac{B}{10\,\mu\mathrm{G}}\right] \cdot \left[\frac{E_{\mathrm{e}}}{10\,\mathrm{TeV}}\right]^{-1} \cdot \left[\frac{R}{1\,\mathrm{pc}}\right]^{2} \mathrm{kyr}, \tag{2.11}$$

where R is the radius of the Pulsar Wind evolving with time as derived by Chevalier (1977)

$$R_{\mathrm{PWN}} = 1.1\,\mathrm{pc} \left(\frac{\dot{E}_0}{10^{38}\,\mathrm{erg\,s^{-1}}}\right)^{1/5} \left(\frac{E_{\mathrm{SN}}}{10^{51}\,\mathrm{erg}}\right)^{3/10} \left(\frac{M_{\mathrm{ej}}}{10\,M_{\odot}}\right)^{-1/2} \left(\frac{t}{10^{3}\,\mathrm{yr}}\right)^{6/5}, \tag{2.12}$$

where $\dot{E}_0$ is the initial spin down luminosity and E_{SN} and M_{ej} are the released energy and ejected mass in the supernova explosion. Eq. 2.12 is only valid for a spherically symmetric case and a young PWN with an age up to some thousand years. A small radius causes high particle losses to the Pulsar Wind. Especially pulsars at lower ages are affected by this process.

Synchrotron cooling The ambient magnetic field B has the biggest influence on the particles' energy. An electrically charged particle deflected by a magnetic field loses energy by radiating photons. The energy loss rate due to this effect for the special case of an electron was derived by Blumenthal & Gould (1970) to

$$\left(\frac{\mathrm{d}E_{\mathrm{e}}}{\mathrm{d}t}\right)_{\mathrm{Sy}} = -\frac{2r_{\mathrm{e}}^2}{3c}\gamma^2 B^2 v^2 \sin^2\alpha, \tag{2.13}$$

with the classical electron radius $r_{\mathrm{e}} = 2.8 \cdot 10^{-13}\,\mathrm{cm}$, $\gamma = {}^{E_e}/_{m_e c^2}$ the Lorentz factor and α the pitch angel between the magnetic field and the direction of the particle's motion. Using the Thomson cross section

$$\sigma_{\mathrm{T}} = \frac{8\pi}{3} r_{\mathrm{e}}^2 = 6.65 \cdot 10^{-25}\,\mathrm{cm}^2 \tag{2.14}$$

and the energy density of the magnetic field $U_{\mathrm{B}} = {}^{B^2}/_{8\pi}$, this expression changes to

$$\left(\frac{\mathrm{d}E_{\mathrm{e}}}{\mathrm{d}t}\right)_{\mathrm{Sy}} = -\frac{4}{3}\sigma_{\mathrm{T}} U_{\mathrm{B}} \beta^2 \gamma^2, \tag{2.15}$$

with $\beta = {}^{v}/_{c}$. Thus the energy loss of a lepton scales as $\Delta E_e \sim B^2 \cdot E_e^2$. Photons emitted by magnetic deflected particles ranging from Radio to X-rays are forming the Pulsar Wind Nebula. IACTs (e.g. H. E. S. S., see Chap. 3) have additionally measured γ-rays up to 100 TeV extending the spectrum of PWNe to the VHE regime. Another physical process is responsible for the emission in this spectral range.

2.4. Production of VHE γ-rays via Inverse Compton emission

The Pulsar Wind is continuously interacting with ambient photon fields. In such a physical interaction a high energy particle can scatter a low energy photon up to some TeV. The most prominent example of a photon population distributed all over the galaxy is the Cosmic Microwave Background (CMB) following a blackbody spectrum with a temperature $T = 2.725\,\mathrm{K}$. But also other photon fields may serve as target for the relativistic particles, e.g. infrared photons from dust or visible radiation produced by stars in the pulsars vicinity. Even synchrotron photons, generated in the wind itself, may serve as a target for high energy leptons. This process is called synchrotron self-Compton (SSC), which is only important for younger PWNe, still having a strong magnetic field which is responsible for intense synchrotron emission. An example for such a PWN is the Crab Nebula, see e.g. Horns & Aharonian (2004). In the case of a non-relativistic lepton the cross section for these interactions is defined by the Thomson cross section from Eq. 2.14. However, high energy particles injected by a pulsar must be considered relativisticly ($\gamma \gg 1$), i.e. the corresponding cross section in the Klein-Nishina limit **?** must be used. As target a general radiation field with a differential density of

$$n(\varepsilon) = \frac{\mathrm{d}n}{\mathrm{d}\varepsilon \mathrm{d}V} \tag{2.16}$$

is assumed. The energy of the upscattered photon ε_1 can be expressed as a fraction E_1 of the initial lepton energy E_e

$$\varepsilon_1 = E_\mathrm{e} E_1 = \gamma m_\mathrm{e} c^2 E_1. \tag{2.17}$$

The photon spectrum for a single electron and a certain number of target photons $\mathrm{d}n = n(\varepsilon)\,\mathrm{d}\varepsilon$ within $\mathrm{d}\varepsilon$ was derived by Blumenthal & Gould (1970) to

$$\left(\frac{\mathrm{d}N_{\gamma,\varepsilon}}{\mathrm{d}t\mathrm{d}E_1}\right)_\mathrm{IC} = \frac{2\pi r_\mathrm{e}^2 m_\mathrm{e} c^3}{\gamma}\,\frac{n(\varepsilon)\mathrm{d}\varepsilon}{\varepsilon}\left[2q\,\ln q + (1+2q)(1-q) + \frac{1}{2}\,\frac{(\Gamma_\mathrm{e} q)^2}{1+\Gamma_\mathrm{e} q}(1-q)\right], \tag{2.18}$$

where $\Gamma_\mathrm{e} = {}^{4\varepsilon\gamma}/_{m_\mathrm{e}c^2}$ and $q = {}^{E_1}/_{\Gamma_\mathrm{e}(1-E_1)}$. Knowing the leptonic energy distribution $\mathrm{d}N_\mathrm{e} = N_\mathrm{e}(\gamma)\mathrm{d}\gamma$, the total energy spectrum can be calculated by integrating over ε and γ (Blumenthal & Gould 1970)

$$\left(\frac{\mathrm{d}N_\mathrm{tot}}{\mathrm{d}t\mathrm{d}\varepsilon_1}\right)_\mathrm{IC} = \int\int N_\mathrm{e}(\gamma)\mathrm{d}\gamma \left(\frac{\mathrm{d}N_{\gamma,\varepsilon}}{\mathrm{d}t\mathrm{d}\varepsilon_1}\right)_\mathrm{IC}. \tag{2.19}$$

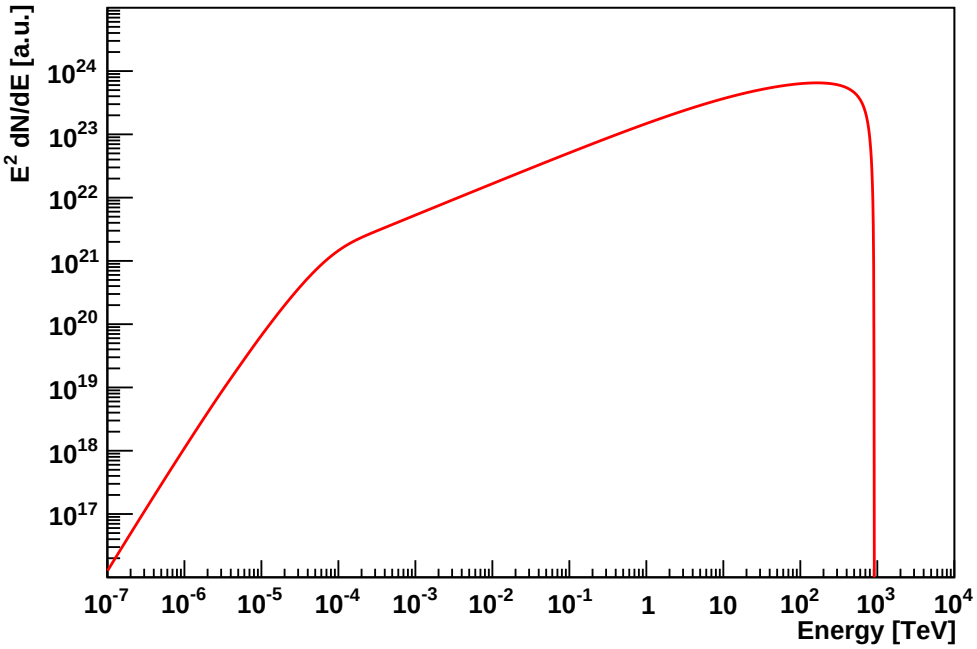

Figure 2.8.: Spectral energy distribution for up-scattered photons. This simulation assumes a leptonic population between 100 GeV and 1000 TeV following a power law with a spectral index of 2. The target photon field is the CMB described by a blackbody spectrum with $T = 2.725\,\mathrm{K}$.

The influence on the energy losses of relativistic particles by the Inverse Compton Effect is quite low compared to synchrotron cooling, despite generating the highest energy photons ever measured. Fig. 2.8 shows a spectral energy distribution from a lepton spectrum as introduced in Sect. 2.2. Combined with the radiation in other wavelengths the γ-rays contribute to a nebula around the pulsar, the PWN, and allow conclusions about the present lepton spectrum.

This Chapter summarized the current understanding of pulsars and PWNe. The evolution of the pulsar population was studied in detail. A non-negligible period derivative results in rotational energy losses of the pulsars. The released energy can be converted to relativistic particles powering a TeV nebula via the Inverse Compton Effect. An opportunity of measuring this VHE radiation of the pulsars' surroundings is introduced in the next Chapter.

3. The High Energy Stereoscopic System (H. E. S. S.)

Focussing on the measurement of the produced γ-rays from this source class, this Chapter presents the measuring technique of H. E. S. S. and gives a short introduction to the data analysis. Afterwards some results of the analyzed data are shown.

A direct measurement of VHE γ-rays can not be realized in space due to the small fluxes of photons requiring a very large detector volume. According to Aharonian et al. (2006a), the flux of the Crab Nebula, the standard candle of γ-ray astronomy (also the strongest steady TeV source), above 1 TeV is determined to $(2.26 \pm 0.08_{\text{stat}}) \cdot 10^{-11}\,\text{cm}^{-2}\,\text{s}^{-1}$. The Earth's atmosphere is opaque to radiation with such high energies. However, the energy deposited by these particles in the atmosphere can be used for an indirect measurement.

3.1. Particle induced air showers

A high energy photon, or any other relativistic particle, hitting the upper parts of the Earth's atmosphere can generate a lepton and an anti lepton via pair production. These particles, also highly energetic, can themselves induce photons via Bremsstrahlung in the electrical field of an atomic nucleus. These photons in turn can produce a lepton and an antilepton via pair production again. Due to those alternating effects, more and more particles are created until absorption processes are starting to dominate in the more dense layers at lower altitudes or the photons reaching the threshold for pair production. This minimum energy is twice the mass of the electron

$$E_{\text{thres}} = 2m_{\text{e}}c^2 = 1.022\,\text{MeV}. \tag{3.1}$$

The mean free path of a photon and the radiation length[1] of an electron are quite similar. Thus a simple model of the development of an electromagnetic air shower (shown in Fig. 3.1) calculates one interaction of the shower after covering one radiation length. The energy of the primary photon is equally distributed to the secondary particles. Such an air shower, which can also be initiated by an energetic electron, differs from particle cascades generated by a hadron (e.g. protons or nuclei). Both types of showers disagree in size and extension facilitating their distinction (see Fig. 3.2). The hadronic shower is much broader by containing some electromagnetic subshowers.

A charged particle exceeding the speed of light in a medium induces the emission of Cherenkov light. The atoms of the medium are polarized by the passing charge which stimulates them to radiate photons interfering constructively. This phenomenon, illustrated in Fig. 3.3, is called Cherenkov Radiation. The emitted light has a maximum intensity at a wavelength of $\lambda \approx 330\,\text{nm}$. Air showers containing high energy particles also emit Cherenkov light, allowing the indirect measurement of the energy and direction of the primary particle.

[1] An electron has only $1/e$ of its primary energy left after covering one radiation length.

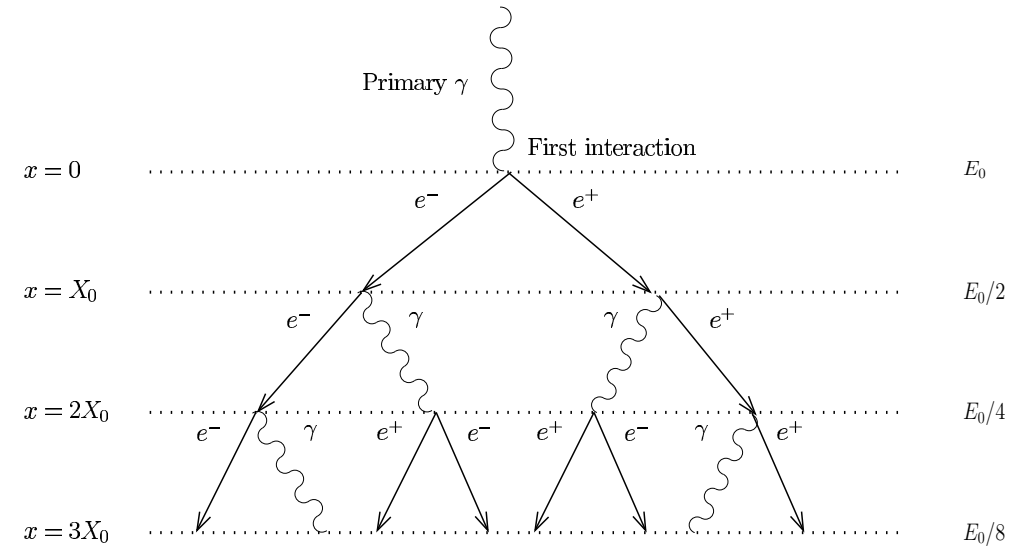

Figure 3.1.: Air shower formation by a primary photon. X_0 is the radiation length which is $7/9$ of the mean free path of a γ-ray. Image taken from Funk (2005).

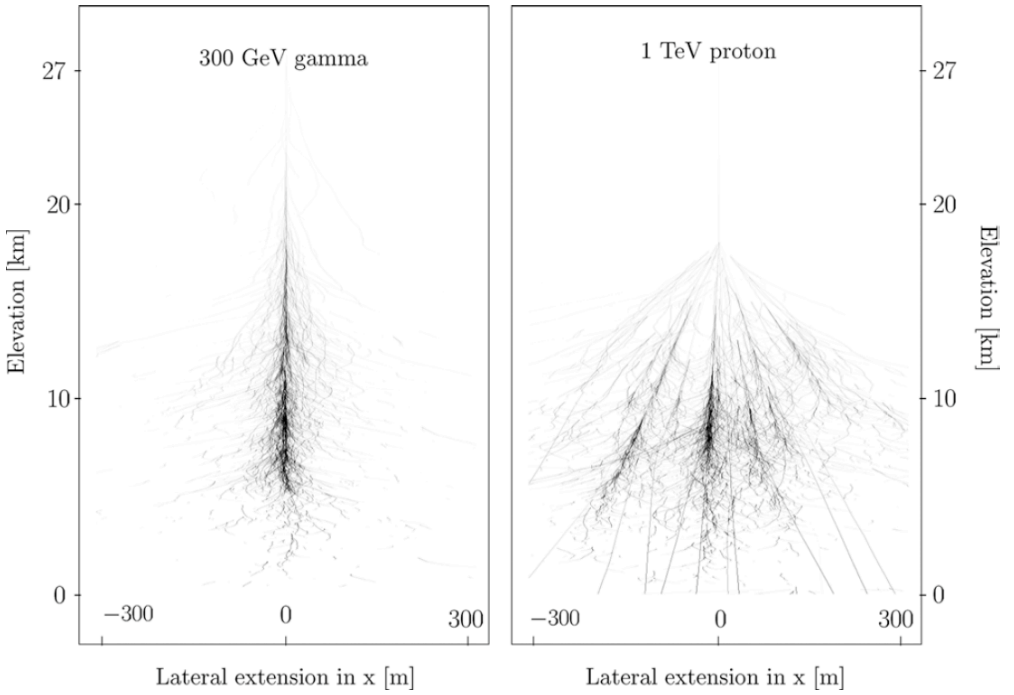

Figure 3.2.: Monte Carlo simulations of air showers of a 300 GeV photon (left) and a 1 TeV proton (right) showing the shower evolution with increasing atmospheric depth. Image taken from Bernlöhr (2010).

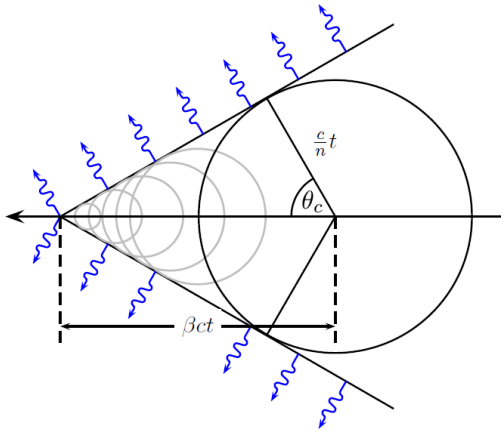

Figure 3.3.: Illustration of the formation of a Cherenkov wave front. The opening angle is given by $\cos\theta = (n\beta)^{-1}$, with n being the refractive index of the local medium and $\beta = v/c$. Image adopted from Göring (2008).

3.2. The H. E. S. S. telescopes

Designed to collect the Cherenkov light, described in the previous Section, the H. E. S. S. Experiment is located in the Khomas Highland in Namibia which provides good observation conditions. It consists of four Imaging Atmospheric Cherenkov Telescopes (IACT) operating since 2004. They are arranged in a square of 120 m length. Every single telescope has mounted 382 mirrors with a diameter of 60 cm each, with a total reflecting area to focus the Cherenkov light of 108 m^2. A camera is placed in the focal plane to record the collected photons. For a detailed review on the camera's functionality, systematics and calibration, see Balzer (2010). To perform azimuthal movements the telescope is mounted on a circular rail. Simultaneously the dish can be elevated up to 90°. One of the telescopes with its characteristic red steel structure is shown in Fig. 3.4. The whole array looking towards the sky is presented in Fig. 3.5. Increasing the number of telescopes allows a stereoscopic reconstruction of the event's direction and energy. A larger effective area also obtains a higher sensitivity. Therefore H. E. S. S. consists of four detectors pointing at the same direction in the sky. The superposition of at least two camera images leads to a better direction estimate of the primary particle. A point source detected with this telescopes has a projected angular size of about 0.1°. This value still depends on the zenith angle of the observation. Due to this Point-Spread-Function (PSF), H. E. S. S. is limited in resolving morphologies of sources of that size or smaller. In contrast, the field of view is very large ($\approx 5°$) and allows studies on sources with a high angular extension. The experiment is able to reconstruct particle energies between about 100 GeV and 100 TeV. Reaching the boundaries of this interval the estimated errors become higher. The error ΔE of the reconstructed energy E_{reco} changing with true energy E_{true} of the primary particle can be defined as

$$\Delta E = \frac{E_{\mathrm{reco}} - E_{\mathrm{true}}}{E_{\mathrm{true}}}. \tag{3.2}$$

Depending on E_{true}, ΔE is also called the relative energy bias (shown in Fig. 3.6). The accessible energy range depends strongly on the zenith angle of the observation. Especially the lower threshold is affected by this parameter. High energies are well reconstructed up to

Figure 3.4.: A single telescope of the array, The camera is parked in a shelter to protect the sensitive instruments from the sunlight and rain.

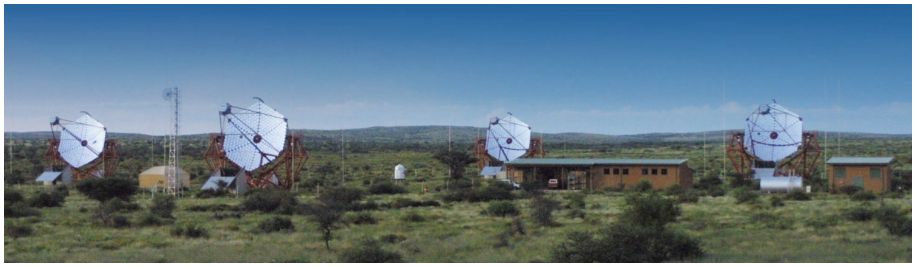

Figure 3.5.: The H. E. S. S. telescopes after their completion in 2004, picture taken from Berge (2006).

$E_{\text{true}} \approx 60\,\text{TeV}$.

The properties of the H. E. S. S. experiment have been described briefly. One main part of this work was analyzing large data sets taken with this stereoscopic system. The next Section introduces the technique of the data analysis and shows some results.

3.3. Data analysis

A short overview of the analysis technique, called Model++, applied in this thesis is given in this Section. Furthermore the way to derive energy spectra and morphology shapes are presented. Finally some results produced with this analysis method are shown.

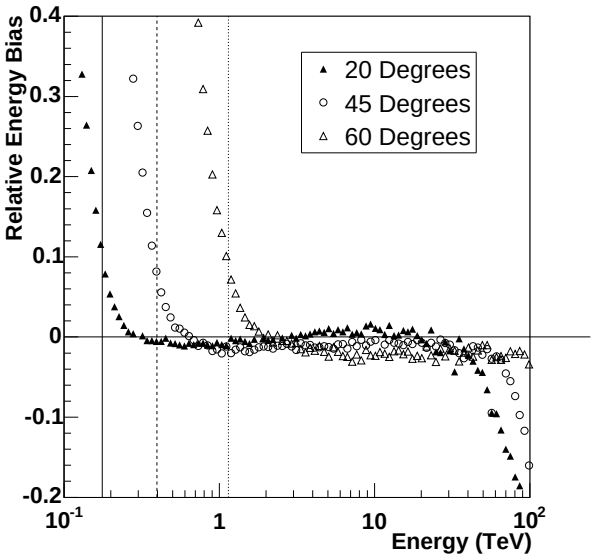

Figure 3.6.: The energy bias of the H. E. S. S. telescopes shows the useful energy range where uncertainties are small. Figure adopted from Aharonian et al. (2006a).

3.3.1. Analysis method

The main information about the primary photon derived by the Cherenkov light distribution in the camera are the direction and the energy. An air shower leaves a certain distribution of Cherenkov light in the camera depending on energy, zenith angle and other parameters of the primary particle. Extensive Monte Carlo simulations of different air showers lead to an analytical expression of Cherenkov light recorded by the camera. After subtracting detector effects, e.g the acceptance, and light from the night sky background, the Model++ analysis method compares the measured camera image with the shower model derived by the simulations. The parameters of the initial photons are then determined by a log-likelihood minimization on the χ^2 value between the simulated and the recorded images. Hadronic showers are responsible for most of the background producing Cherenkov light. The Model++ analysis technique is trained to distinguish efficiently between these shower types. According to de Naurois & Rolland (2009) 95 % of the hadronic background can be rejected while keeping 70 % of the γ-like events. A more detailed description of this analysis technique is also given by de Naurois & Rolland (2009).

3.3.2. Background estimation, spectrum generation and morphology fits

After applying cuts on the signal to reduce the hadronic background, it is necessary to estimate the level of background γ-like events in the field of view caused by diffuse emission, electrons or wrongly classified hadronic showers. An estimate of this level allows to extract the real signal originating from the observed source and to determine an energy spectrum. First one has to define the source size in the sky, called on-region. The most common shape is a circular target with a certain radius. Smaller than 0.1° is not useful due to the limited accuracy of the directional reconstruction of the telescopes known as the PSF. The off-region can be determined by different background models applied in γ-ray astronomy. One of them

is the ring-background model using a ring-shaped region around the target to estimate the background level. The reflected-background model defines several off-regions arranged in a circle around the observation position to determine the background in the on-region. For a further, more detailed review on these background models see Berge et al. (2007). Avoiding other sources to contaminate the background estimation, one has to define exclusion regions in the sky where high emission is expected. These do not contribute to the calculation of the background as they are not representative for the level at the on-region. The energy spectrum is derived by a method using a log-likelihood comparison of the reconstructed energies with an expected theoretical rate. This method, named forward-folding (de Naurois 2010), allows to determine the expected flux with different models. This thesis applies three different theoretical spectrum models which differ in numbers of free parameters and show different behaviors.

Power law

$$\frac{\mathrm{d}N}{\mathrm{d}E} = \Phi_0 \left(\frac{E}{E_0}\right)^{-\alpha}, \tag{3.3}$$

with the reference energy E_0 (usually set to 1 TeV) and the flux normalization Φ_0 given in units of $\mathrm{TeV}^{-1}\,\mathrm{cm}^{-2}\,\mathrm{s}^{-1}$. The spectral index of the source is α. This is the most simple type of a differential spectrum with just two free parameters. The spectrum of most sources is well described by this model, but especially at higher energies ($E > 10\,\mathrm{TeV}$) it often differs too much from the measured flux.

Curved power law

$$\frac{\mathrm{d}N}{\mathrm{d}E} = \Phi_0 \left(\frac{E}{E_0}\right)^{-(\alpha+\beta\log(E/E_0))}, \tag{3.4}$$

where β is the curvature of the index. This model is more complex, providing an energy-dependent spectral index by introducing an additional free parameter in comparison to Eq. 3.3.

Broken power law

$$\frac{\mathrm{d}N}{\mathrm{d}E} = \Phi_0 \cdot \begin{cases} \left(\frac{E}{E_0}\right)^{-\alpha_0} & E \leq E_{\mathrm{cut}} \\ \left(\frac{E_{\mathrm{cut}}}{E_0}\right)^{\alpha_1-\alpha_0} \left(\frac{E}{E_0}\right)^{-\alpha_1} & E \geq E_{\mathrm{cut}} \end{cases} \tag{3.5}$$

Four parameters are free to fit in this model combined of two power laws (Eq. 3.3). The two spectral indices are α_1 and α_2. The spectrum changes its shape at the energy E_{cut}.

To point out the best spectrum fit for a single source, one has to compare the reduced χ^2 values calculated for every model. The smallest $\chi^2/\mathrm{d.o.f.}$ is assumed to be the best description of the observed data. If these values are similar to each other, the model with less free parameters is preferred.

Another option provided by Model++ is the determination of the source morphology. The shape of an emission region can be fit by several models. The most general case for sources

like PWNe is a two dimensional asymmetrical Gaussian following

$$L(x,y) = \frac{N}{2\pi\sigma_1\sigma_2} \cdot \exp\left(-\frac{((x-X_0)\cos\beta\cos\phi + (y-Y_0)\sin\phi)^2}{2\sigma_1^2}\right) \cdot \exp\left(-\frac{(-(x-X_0)\cos\beta\cos\phi + (y-Y_0)\sin\phi)^2}{2\sigma_2^2}\right),$$

where the free parameters are

- N the normalization
- X_0 and Y_0 the coordinates of the center of gravity of the emission
- σ_1 and σ_2 the widths of the source in the two directions at which the emission decreased to $1/2$ of its maximum
- β the declination of the source
- ϕ the angle between the x-axis and main axis of the asymmetrical Gaussian.

This is the only morphological model used in this thesis allowing the unification of the sources. Point-like or radially symmetric sources are also well described by an asymmetrical Gaussian. One condition for this model to fit is a central peak and no ring shape of the source, e.g. like a shell of a SNR. The center of gravity of emission can easily be read out from the fit values X_0 and Y_0. σ_1 and σ_2 are the 68 % containment widths of the fitted source, used to interpret its size.

3.3.3. Analysis results

For an overview of the results of Model++ two exemplary analyses are shown in this Section. The considered sources are the Crab Nebula which is the standard candle in γ-ray astronomy and HESS J1825−137, an extended PWN with an observable energy dependent morphology (Aharonian et al. 2006d). Fig. 3.7 shows analysis results of the bright TeV source HESS J0534+220 associated with the Crab Nebula. It has the same extension as the instrument PSF, i.e. for H. E. S. S. it seems to be a point source. Another result of the Model++ analysis of a source, associated with a PWN, is shown in Fig. 3.8. Again spectral and morphological fits were performed. The same procedure has been performed for every known PWN and sources whose origin also might be an energetic pulsar. Tab. 3.1 shows the results of the characteristic fit parameters from the different spectrum models. Morphology analysis results derived from the asymmetrical Gaussian are listed in Tab. 3.2.

An efficient way to measure VHE γ-rays was introduced in this Chapter. The analyzed sources contribute to a sample of PWNe and PWN candidates. Its properties and evolution are introduced in the next Chapter.

H. E. S. S. source	best fit	α	β	E_{cut}	$I(1\,\mathrm{TeV})$
HESS J0534 + 220	BPL	2.87 ± 0.01	0.16 ± 0.02	3.59 ± 0.37	17.35 ± 0.36
HESS J0536−691	CPL	2.8 ± 0.14	0.58 ± 0.26	6.2 ± 3.15	0.55 ± 0.07
HESS J0835−455	CPL	1.9 ± 0.04	0.11 ± 0.04	2.65 ± 0.92	8.69 ± 0.65
HESS J1018−589	PL	2.82 ± 0.33	3.17 ± 2.09	0.88 ± 0.44	0.24 ± 0.07
HESS J1119−614	PL	2.75 ± 0.15	0.38 ± 0.25	5.15 ± 3.12	0.58 ± 0.06
HESS J1303−631	BPL	2.52 ± 0.03	0.12 ± 0.04	4.21 ± 1.03	2.75 ± 0.14
HESS J1356−645	PL	2.2 ± 0.1	0.32 ± 0.14	3.56 ± 1.4	2.67 ± 0.24
HESS J1406−613	PL	2.81 ± 0.44	-0.14 ± 0.17	1.38 ± 0.84	0.45 ± 0.15
HESS J1418−609	PL	2.72 ± 0.12	0.09 ± 0.13	2.09 ± 2.53	1.09 ± 0.1
HESS J1420−607	CPL	2.68 ± 0.1	0.22 ± 0.13	3.46 ± 0.89	1.51 ± 0.18
HESS J1503−582	PL	2.75 ± 0.19	0.1 ± 0.23	5.39 ± 17.76	0.46 ± 0.08
HESS J1514−591	CPL	2.43 ± 0.04	0.12 ± 0.04	3.05 ± 0.93	4.41 ± 0.24
G327.1−1.1	PL	2.44 ± 0.19	-0.02 ± 0.15	1.96 ± 6.6	0.27 ± 0.05
HESS J1614−518	CPL	2.39 ± 0.05	0.24 ± 0.07	0.39 ± 0.07	6 ± 0.53
HESS J1616−508	CPL	2.37 ± 0.05	0.16 ± 0.05	2.49 ± 0.7	7.18 ± 0.61
HESS J1702−420	PL	2.47 ± 0.08	0.09 ± 0.09	2.84 ± 0.83	4.29 ± 0.42
HESS J1708−443	PL	2.14 ± 0.16	0.1 ± 0.15	20.52 ± 54.37	0.82 ± 0.16
HESS J1718−385	CPL	2.02 ± 0.08	0.32 ± 0.12	5.22 ± 1.78	0.68 ± 0.1
HESS J1745−303	BPL	2.77 ± 0.05	-0.09 ± 0.03	0.31 ± 0.03	3.26 ± 0.79
HESS J1747−281	CPL	2.37 ± 0.05	0.26 ± 0.06	1.13 ± 0.22	0.37 ± 0.04
HESS J1804−216	CPL	2.63 ± 0.03	0.21 ± 0.05	0.85 ± 0.17	3.73 ± 0.27
HESS J1809−193	CPL	2.21 ± 0.04	0.1 ± 0.04	3.04 ± 0.89	2.79 ± 0.23
HESS J1813−178	CPL	2.23 ± 0.04	0.16 ± 0.05	1 ± 0.28	3.11 ± 0.25
HESS J1825−137	BPL	2.4 ± 0.03	0.09 ± 0.03	2.03 ± 0.49	0.52 ± 0.03
HESS J1831−095	PL	2.24 ± 0.21	0.51 ± 0.43	1.13 ± 0.49	0.22 ± 0.05
HESS J1832−084	PL	2.65 ± 0.2	0.15 ± 0.26	3.4 ± 3.22	0.16 ± 0.04
HESS J1833−105	PL	2.27 ± 0.17	0.01 ± 0.13	2.36 ± 7.71	0.31 ± 0.06
HESS J1834−087	PL	2.57 ± 0.05	0 ± 0.04	7.57 ± 7.1	1.97 ± 0.13
HESS J1837−069	CPL	2.6 ± 0.03	0.09 ± 0.04	1.79 ± 0.58	7.68 ± 0.43
HESS J1846−029	PL	2.77 ± 0.15	0.19 ± 0.21	0.98 ± 0.48	0.32 ± 0.05
HESS J1857 + 026	CPL	2.39 ± 0.05	-0.05 ± 0.04	4.89 ± 12.53	2.81 ± 0.23
HESS J1858 + 020	PL	2.32 ± 0.14	0.21 ± 0.17	5.9 ± 2.22	0.56 ± 0.08
HESS J1908 + 063	PL	2.23 ± 0.07	0.04 ± 0.06	2.48 ± 3.57	5.98 ± 0.37
HESS J1912 + 101	CPL	2.49 ± 0.12	0.22 ± 0.16	8.05 ± 5.82	2.1 ± 0.36
HESS J1930 + 186	PL	3.08 ± 0.37	0.59 ± 0.78	2.86 ± 4.11	0.19 ± 0.04

Table 3.1.: Spectral analysis of the considered sources with three different spectral models. α is the photon index of a power-law fit (PL), β the curvature of the curved power-law model (CPL) and E_{cut} the spectral break fitted by the broken power law (BPL) in units of TeV. $I(1\,\mathrm{TeV})$ gives the flux above 1 TeV in units of $\mathrm{cm}^{-2}\,\mathrm{s}^{-1}$.

H. E. S. S. source	RA [°]	DEC [°]	σ_1 [°]	σ_2 [°]
HESS J0534 + 220	83.63 ± 0	22.02 ± 0	0.02 ± 0	0.02 ± 0
HESS J0536−691	84.44 ± 0.01	-69.17 ± 0	0.01 ± 0.01	0.03 ± 0.01
HESS J0835−455	128.69 ± 0.02	-45.69 ± 0.02	0.52 ± 0.02	0.48 ± 0.01
HESS J1018−589	154.67 ± 0.07	-58.93 ± 0.02	0.15 ± 0.05	0.09 ± 0.02
HESS J1119−614	169.71 ± 0.02	-61.45 ± 0.01	0.07 ± 0.01	0.11 ± 0.01
HESS J1303−631	195.72 ± 0.01	-63.21 ± 0	0.13 ± 0	0.2 ± 0
HESS J1356−645	208.88 ± 0.05	-64.46 ± 0.03	0.14 ± 0.03	0.2 ± 0.03
HESS J1406−613	211.87 ± 0.09	-61.35 ± 0.05	0.2 ± 0.05	0.26 ± 0.06
HESS J1418−609	214.82 ± 0.04	-60.85 ± 0.01	0.24 ± 0.02	0.14 ± 0.01
HESS J1420−607	214.94 ± 0.02	-60.81 ± 0.01	0.13 ± 0.01	0.18 ± 0.01
HESS J1503−582	225.95 ± 0.08	-58.27 ± 0.03	0.24 ± 0.06	0.19 ± 0.03
HESS J1514−591	228.51 ± 0.01	-59.17 ± 0	0.1 ± 0	0.11 ± 0
G327.1−1.1	238.66 ± 0.03	-55.09 ± 0.02	0.06 ± 0.02	0.05 ± 0.02
HESS J1614−518	243.57 ± 0.02	-51.84 ± 0.01	0.19 ± 0.01	0.25 ± 0.01
HESS J1616−508	244.12 ± 0.01	-50.88 ± 0.01	0.18 ± 0.01	0.19 ± 0.01
HESS J1702−420	255.64 ± 0.03	-41.97 ± 0.03	0.26 ± 0.02	0.49 ± 0.03
HESS J1708−443	257.16 ± 0.1	-44.37 ± 0.05	0.25 ± 0.08	0.16 ± 0.05
HESS J1718−385	258.3 ± 0.01	-39.73 ± 0	0.37 ± 0	0.34 ± 0
HESS J1745−303	266.30 ± 0	-30.45 ± 0	0.38 ± 0	0.38 ± 0
HESS J1747−281	266.85 ± 0	-28.16 ± 0	0.04 ± 0	0.05 ± 0
HESS J1804−216	271.17 ± 0.01	-21.68 ± 0.01	0.22 ± 0.01	0.24 ± 0.01
HESS J1809−193	272.44 ± 0.02	-19.43 ± 0.02	0.41 ± 0.02	0.24 ± 0.01
HESS J1813−178	273.4 ± 0	-17.84 ± 0	0.06 ± 0	0.08 ± 0
HESS J1825−137	276.26 ± 0.01	-14.04 ± 0.01	0.45 ± 0.01	0.52 ± 0.01
HESS J1831−095	278.65 ± 0.01	-8.77 ± 0.01	0.3 ± 0.01	0.28 ± 0.01
HESS J1832−084	278.14 ± 0.01	-8.47 ± 0.01	0.03 ± 0.03	0.03 ± 0.01
HESS J1833−105	278.4 ± 0.01	-10.57 ± 0.01	0.02 ± 0.01	0.04 ± 0.01
HESS J1834−087	278.68 ± 0.01	-8.78 ± 0.01	0.22 ± 0.01	0.2 ± 0.01
HESS J1837−069	279.31 ± 0.01	-6.96 ± 0.01	0.3 ± 0.01	0.28 ± 0.01
HESS J1846−029	281.61 ± 0	-2.97 ± 0	0.03 ± 0.01	0.04 ± 0.01
HESS J1857 + 026	284.34 ± 0.01	2.66 ± 0.01	0.2 ± 0.01	0.27 ± 0.01
HESS J1858 + 020	284.35 ± 0.01	2.64 ± 0.02	0.19 ± 0.01	0.28 ± 0.02
HESS J1908 + 063	286.97 ± 0.03	6.41 ± 0.04	0.36 ± 0.03	0.49 ± 0.04
HESS J1912 + 101	288.26 ± 0.03	10.13 ± 0.03	0.36 ± 0.03	0.31 ± 0.03
HESS J1930 + 186	54.09 ± 0.01	0.27 ± 0.01	0.1 ± 0.01	0.1 ± 0.02

Table 3.2.: Morphological analysis with an asymmetrical Gaussian model. RA is the right ascension, while DEC represents the declination of the center of gravity of the source. σ_1 and σ_2 represent the widths of the source in both directions. Some errors are listed to be zero, which is a rounding effect. Uncertainties smaller than an absolute value of 0.005 are set to zero. If σ_1 and σ_2 are smaller than 0.1° the source is considered point-like.

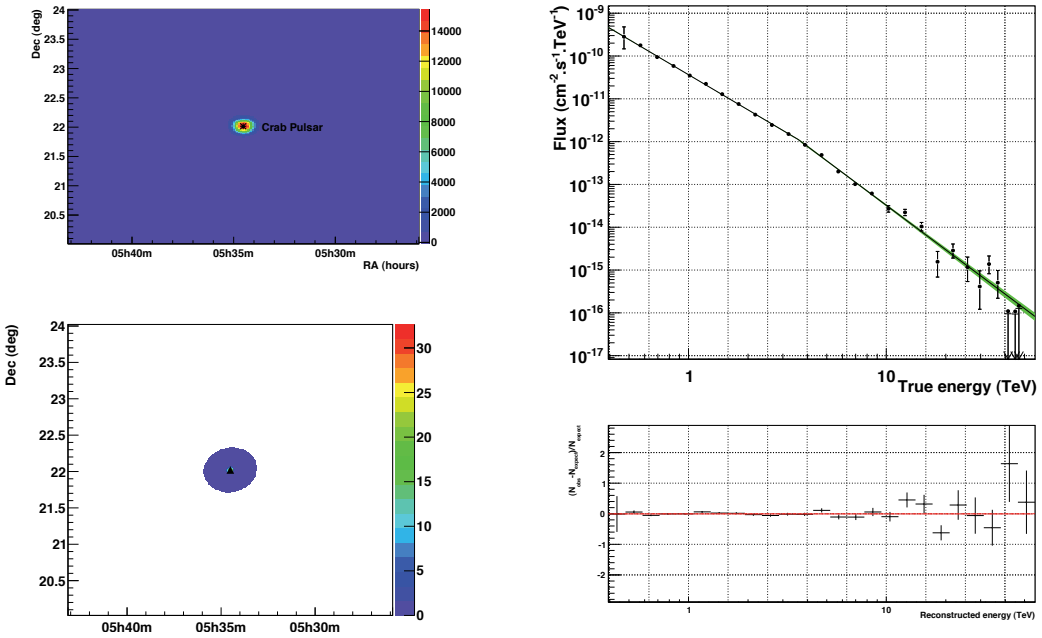

Figure 3.7.: γ-ray excess map (upper left) of the Crab Nebula with an exposure of 50.4 hours (41 hours acceptance corrected due to zenith angle and effective area effects) leading to a significance level of 260 σ. The position of the pulsar is marked by a black star. The fit of the emission with an asymmetrical Gaussian (lower left) shows the position of the center of gravity of emission marked by a black triangle. The spectrum of this source (upper right) can be fit by a broken power law with $\chi^2/\text{d.o.f} = {}^{37.1}/_{23}$. The residuals of the fit are shown on the lower right panel.

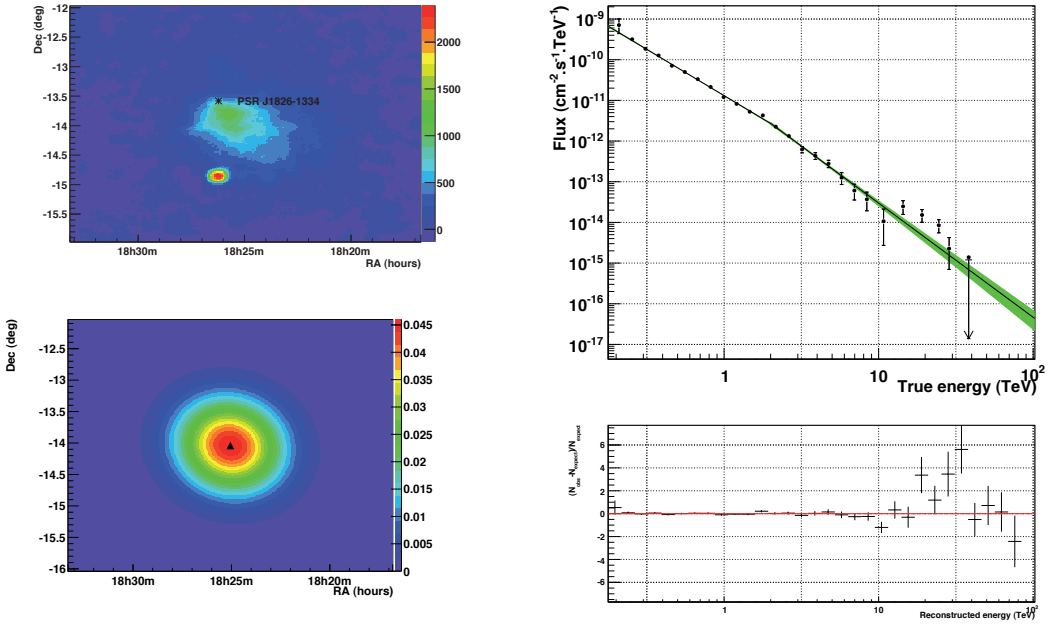

Figure 3.8.: Excess map (upper left) of the extended source HESS J1825−137 after 62.3 hours of observation time (33.5 hours acceptance corrected) providing a significance of $56.9\,\sigma$. About 1.5° to the south of the pulsar position, marked by a black star, the bright point-like binary system LS 5039 is located. The morphology fit (lower left) shows clear evidence of an extended source. A black triangle marks the position of the center of gravity of emission. The spectrum of this source (upper right) is well described by a broken power law model ($\chi^2/\text{d.o.f} = {}^{39.9}/_{27}$). On the lower right panel the residuals of the fit are shown.

4. The PWN Sample

The previous Chapters already gave an overview of PWNe in general and a technique to measure their VHE γ-rays. The following Sections will focus on H.E.S.S. sources that have been identified as PWN or are likely candidates. The Chapter shows pulsars producing TeV nebulae as part of the whole pulsar population and addresses the question why only few of them cause radiation in the VHE regime. Similar work was done before by S. Carrigan (2007) who tried to constrain the attributes of energetic pulsars, generating TeV emission. First the identified PWNe and possible PWN candidates with the parameters of the associated pulsars are presented. Then this work will focus on general characteristics and the evolution of the whole PWN sample.

4.1. Composition of the PWN sample

The most common identified source class in the TeV sky are PWNe (compare Fig. 1.3). Strong criteria for their identification are:

- An energetic pulsar is located near the center of gravity of emission.
- The source luminosity does not exceed the spin down power of the pulsar which would lead to an efficiency higher than 100 %. This criterion was applied in former times but it is questionable (see Sect. 4.3.3).
- The source has to be centrally filled, indicating a small but strong energy source.
- If the VHE emission can be resolved as an extended source, its morphology should be energy dependent, i.e. the spectrum should be steeper at larger distances to the pulsar. In a PWN scenario this is explained by the electrons, being subject to cooling effects while propagating away from the pulsar, see e.g. Aharonian et al. (2006d).
- An X-ray counterpart should be present, originating from synchrotron emission of the relativistic particles.

Tab. 4.1 shows a list of all PWNe detected and identified by H. E. S. S. including the characteristic attributes of the associated pulsars. Only sources published as PWN contribute to this table.
Many of the sources detected with H. E. S. S. are still unidentified (as seen in Fig. 1.3). However, some of them show evidence to be powered by a pulsar. A clear identification was not possible by different reasons. Either the luminosity of the source exceeds the pulsar's spin down power or the rotating neutron star is located offset from the VHE emission region. Every so far unidentified H. E. S. S. source with a centrally filled morphology next to an energetic pulsar known from the ATNF Pulsar Database, is considered to be PWN candidate. A numerous sample gives chance to exclude PWN scenarios for some sources if their properties differ significantly from the rest of the population. The sample of PWN candidates is listed

H. E. S. S. -source	associated pulsar	period [s]	$\dot{E}$ [erg/s]	t_c [kyr]	d [kpc]	reference
HESS J0534+220	PSR J0534+2200	0.0331	$4.6 \cdot 10^{38}$	1.24	2	[1]
HESS J0536−691	PSR J0537−6910	0.0161	$4.9 \cdot 10^{38}$	4.93	48.1	[2]
HESS J0835−455	PSR J0835−4510	0.0893	$6.9 \cdot 10^{36}$	11.3	0.29	[3]
HESS J1018−589	PSR J1016−5857	0.1074	$2.6 \cdot 10^{36}$	21	9.31	[4]
HESS J1119−614	PSR J1119−6127	0.4077	$2.3 \cdot 10^{36}$	1.61	8.4	[5]
HESS J1303−631	PSR J1301−6305	0.1845	$1.7 \cdot 10^{36}$	11	15.84	[6]
HESS J1356−645	PSR J1357−6429	0.1661	$3.1 \cdot 10^{36}$	7.31	4.09	[2]
HESS J1418−609	PSR J1418−6058	0.1106	$5.0 \cdot 10^{36}$	10.3	5	[7]
HESS J1420−607	PSR J1420−6048	0.0682	$1.0 \cdot 10^{37}$	13	6.09	[7]
HESS J1514−591	PSR J1513−5908	0.1507	$1.8 \cdot 10^{37}$	1.55	5.81	[8]
HESS J1708−443	PSR J1709−4429	0.1025	$3.4 \cdot 10^{36}$	17.5	1.82	[9]
HESS J1718−385	PSR J1718−3825	0.0747	$1.3 \cdot 10^{36}$	89.5	4.24	[10]
HESS J1747−281	PSR J1747−2809	0.0522	$4.3 \cdot 10^{37}$	5.31	13	[11]
HESS J1825−137	PSR J1826−1334	0.1015	$2.8 \cdot 10^{36}$	21.4	4.12	[12]
HESS J1833−105	PSR J1833−1034	0.0619	$3.4 \cdot 10^{37}$	4.85	4.3	[13]
HESS J1837−069	PSR J1837−0604	0.0963	$2.0 \cdot 10^{36}$	33.8	6.19	[14],[15]
HESS J1846−029	PSR J1846−0258	0.3257	$8.1 \cdot 10^{36}$	0.728	5.1	[13]
HESS J1857+026	PSR J1856+0245	0.0809	$4.6 \cdot 10^{36}$	20.6	10.28	[14],[16]
HESS J1930+186	PSR J1930+1852	0.1369	$1.2 \cdot 10^{37}$	2.89	5	[17]

Table 4.1.: PWNe detected with the H. E. S. S. telescopes sorted by ascending Right Ascension. Also listed, the parameters concerning the pulsar which are taken from the ATNF Pulsar database (Manchester et al. 2005). References: [1] Aharonian et al. (2006a), [2] paper in preparation by the HESS-Collaboration, [3] Aharonian et al. (2006b), [4] Camilo et al. (2004), [5] Chaves & Djannati-Atai (in prep.), [6] Aharonian et al. (2005b), [7] Aharonian et al. (2006e), [8] Aharonian et al. (2005c), [9] Hoppe et al. (2009), [10] Aharonian et al. (2007), [11] Qiao et al. (2009), [12] Aharonian et al. (2006d), [13] Djannati-Ataĭ et al. (2008), [14] Aharonian et al. (2005a), [15] Gotthelf & Halpern (2008), [16] Hessels et al. (2008), [17] Acciari et al. (2010).

H. E. S. S. -source	associated pulsar	period [s]	$\dot{E}$ [erg/s]	t_c [kyr]	d [kpc]
HESS J1406−613	PSR J1406−6121	0.2131	$2.2 \cdot 10^{35}$	61.7	9.11
HESS J1503−582	PSR J1502−5828	0.6681	$4.8 \cdot 10^{33}$	291	12.21
G327.1−1.1	PSR J1554−5512	3.4180	$3.1 \cdot 10^{31}$	1740	8.05
HESS J1614−518	PSR J1613−5211	0.4575	$7.9 \cdot 10^{33}$	377	6.14
HESS J1616−508	PSR J1617−5055	0.0694	$1.6 \cdot 10^{37}$	8.13	6.46
HESS J1702−420	PSR J1702−4128	0.1821	$3.4 \cdot 10^{35}$	55.1	5.18
HESS J1745−303	PSR J1745−3040	0.3674	$8.5 \cdot 10^{33}$	546	2.08
HESS J1804−216	PSR J1803−2137	0.1337	$2.2 \cdot 10^{36}$	15.8	3.94
HESS J1809−193	PSR J1809−1917	0.0828	$1.8 \cdot 10^{36}$	51.3	3.71
HESS J1813−178	PSR J1813−1749	0.0447	$6.8 \cdot 10^{37}$	4.6	4.5
HESS J1831−095	PSR J1831−0952	0.0673	$1.1 \cdot 10^{36}$	128	4.32
HESS J1832−084	PSR J1832−0827	0.6473	$9.3 \cdot 10^{33}$	161	4.75
HESS J1833−087	PSR J1834−0827	0.0853	$5.8 \cdot 10^{35}$	147	5.67
HESS J1858+020	PSR J1857+0143	0.1398	$4.5 \cdot 10^{35}$	71	5.18
HESS J1908+063	PSR J1907+0602	0.1066	$2.8 \cdot 10^{36}$	19.5	3.01
HESS J1912+101	PSR J1913+1011	0.0359	$2.9 \cdot 10^{36}$	169	4.48

Table 4.2.: Candidates of PWNe listed by ascending Right Ascension. Manchester et al. (2005) referring to the ATNF Pulsar Database provided the parameters of the associated pulsars.

in Tab. 4.2.

Many PWNe and candidates were detected during the H. E. S. S. survey of the Galactic Plane (Aharonian et al. 2006c). Kargaltsev & Pavlov (2010) correlated the γ-ray emission with X-ray data to find possible PWNe in the VHE regime. It has to be noted that the best distance estimates for the pulsars might still contain large errors. The ATNF Pulsar Database (Manchester et al. 2005) does not provide these values. Thus for further investigations the distance error is set to zero. The periods are actually measured with higher precision than shown in Tab. 4.1 and 4.2.

4.2. PWN sample with respect to the whole pulsar population

Analyzing the VHE emission seen by H.E.S.S. from the above PWN and PWN candidate sample with 35 members was one of the main parts of this work. Pulsars thought to power these sources represent only a small fraction of the giant population of fast rotating neutron stars (shown in 2.1.2). This section will point out important properties of pulsars powering PWNe that are bright in VHE γ-rays. Fig. 4.1 indicates that PWNe as well as the whole pulsar population are equally distributed over the Galactic plane. Thus the location in the galaxy has no influence and other criteria for pulsars developing PWNe observed with H. E. S. S. must be important. So far, only young pulsars could be associated with significant γ-ray emission. Therefore, a short rotation period might be an important criterion for a TeV bright PWN. Fig. 4.2 confirms this suggestion, but many pulsars with similar periods are dark in the TeV sky. Thus a high rotation frequency alone is not a useful criterion either. However, the period derivative gives evidence to a certain group of pulsars producing prominent nebulae in the VHE regime. As shown in Fig. 4.3 only high spin down rates $\dot{P}$ lead to energetic PWNe. Lower values do not provide enough energy output to power a relativistic

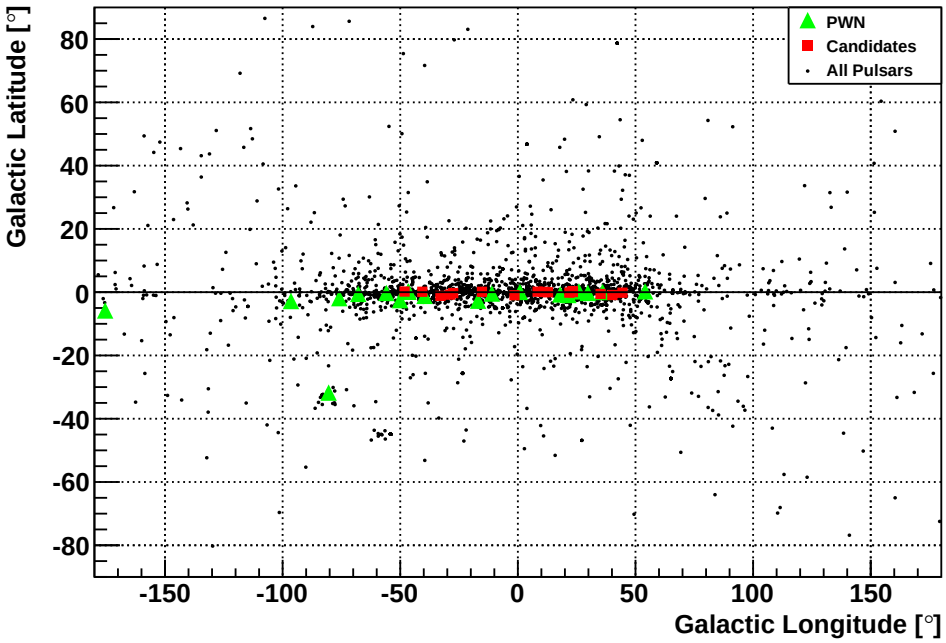

Figure 4.1.: Comparison with Fig. 2.3 shows the distribution of PWNe in the Galaxy. Note: one PWN has already been identified in the LMC. The same mapping as in Fig. 2.3 was used.

particle wind. Following Eq. 2.3 the spin-down luminosity of pulsars generating PWNe must be rather high compared to the TeV dark pulsars for conditions above (low period, high spin-down rate). Fig. 4.4 depicts this assumption. The most energetic pulsars are likely to produce VHE γ-ray emission. Many PWN candidates are older and hence have a lower energy output which makes their detection more challenging in the VHE regime. A P-$\dot{P}$-diagram clarifies why H. E. S. S. does not see much more PWNe. The pulsars responsible for VHE emission have low periods and high period derivatives. But this combination is seldom, as illustrated in Fig. 4.5. Only few pulsars fulfill both criteria at the same time. A large fraction of the whole population is clustering at $\dot{P} \approx 10^{-15}\,\mathrm{s\,s^{-1}}$ and $P \approx 1\,\mathrm{s}$. But the high energy sample has smaller periods and higher period derivatives. Therefore, pulsars powering this energetic emission are rare and very special. In order to enlarge the sample of known PWNe, H. E. S. S. could observe the pulsars with similar parameters. But specific conditions might also prevent their detection. Some pulsars might be too far away, leading to fluxes below the detection threshold of current IACT. Also, some of these pulsars are located too far north and are therefore not observable with the H. E. S. S. experiment. Trying to establish a connection between pulsars and VHE emission was already investigated before (Carrigan 2007).

This Section discussed properties of pulsars generating PWNe. Small periods and high period derivatives pointed out to be a necessary criterion. The following Section focuses on the measured data listed in Tab. 3.1 and 3.2.

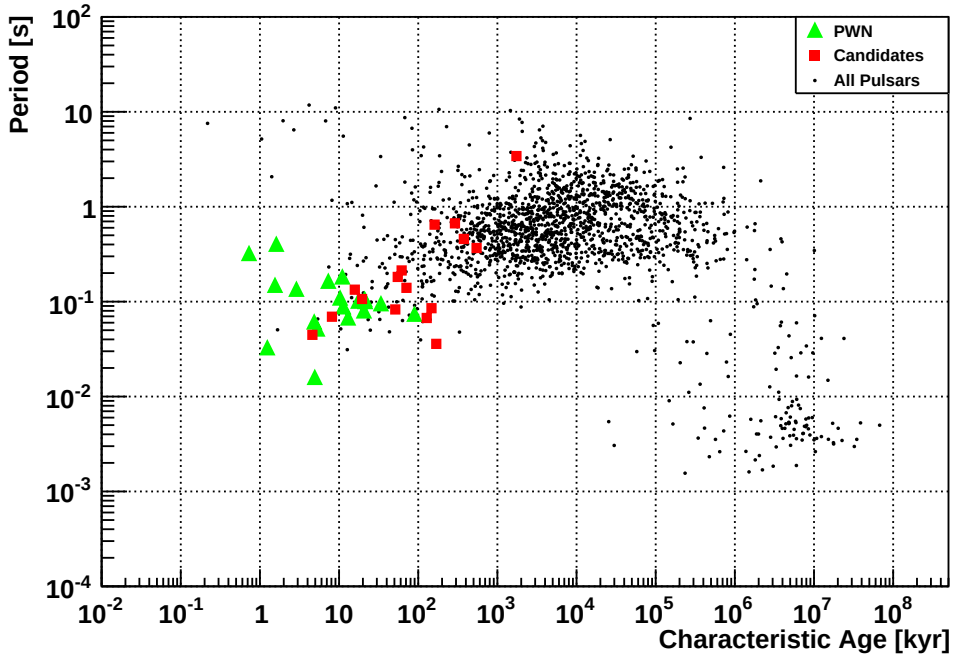

Figure 4.2.: Period of the pulsars plotted against their age. Low aged pulsars with small periods are causing the PWNe seen with the H. E. S. S. telescopes.

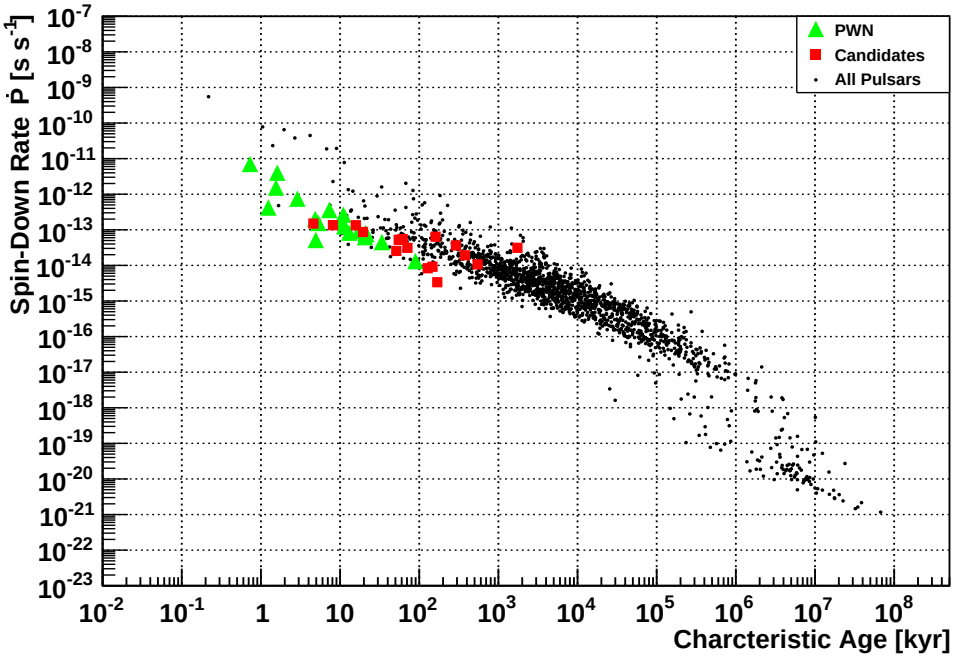

Figure 4.3.: The period derivatives of the populations shown against the respective characteristic age. All TeV PWNe correspond to young pulsars with a high spin-down rate.

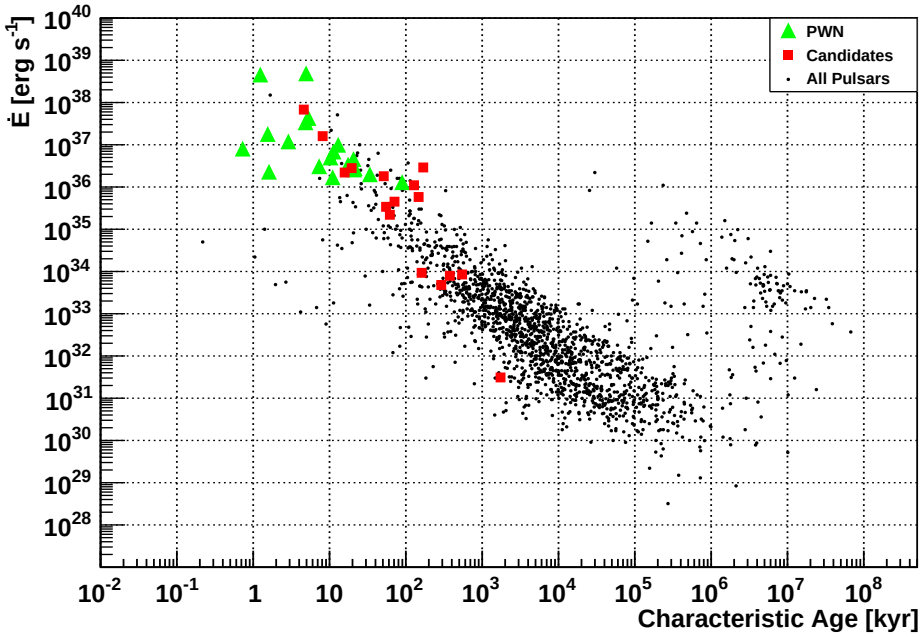

Figure 4.4.: As shown in Fig. 2.6 the spin-down luminosity depends on the characteristic age. The PWNe and candidates are highlighted in green and red, respectively. Their counterparts are young and energetic pulsars.

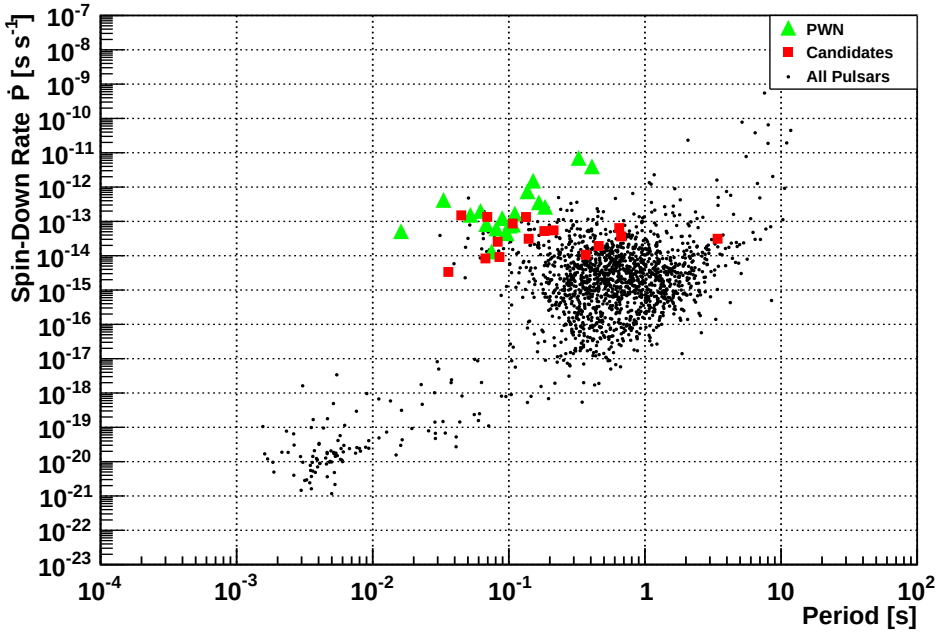

Figure 4.5.: Period derivative plotted over the period. Most of pulsars cluster in a compact region at $P \approx 1\,\mathrm{s}$ and $\dot{P} \approx 10^{-15}\,\mathrm{s\,s^{-1}}$. The PWNe are only seen at the top left edge of this cluster.

4.3. The sample in the VHE regime

As already mentioned in Sect. 3.3.3 spectral and morphological analyses have been performed for all members of the sample. The results allow conclusions on the evolutionary behavior of a PWN. Long-term observations of pulsars powering a TeV nebula do not existing yet. Thus one has to regard each pulsar with its characteristic age as an evolutionary state of the same source type.

4.3.1. Morphological evolution

Asymmetrical Gaussians provide the most general analytical case of a source morphology (explained in Sect. 3.3.2). The fitted peak can be used to calculate the apparent offset from the pulsar. Most pulsars have high space velocities up to $1000\,\mathrm{km\,s^{-1}}$, resulted from a kick

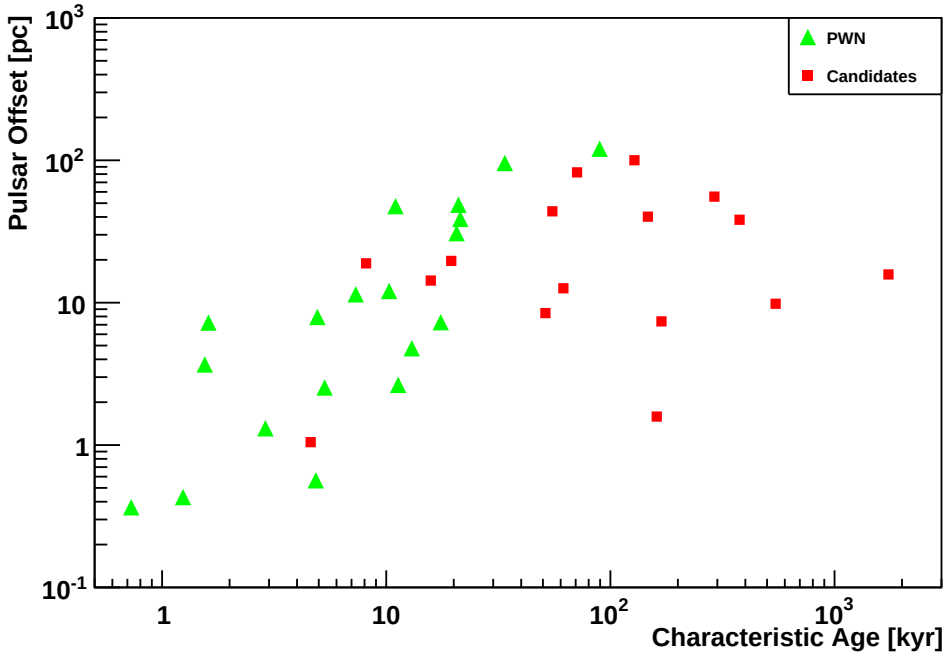

Figure 4.6.: The offset of the pulsar to its associated source of VHE radiation is shown here. A slight increase with the characteristic age can be recognized, especially for identified PWNe.

during the core collapse, leaving their own PWN behind (Gaensler & Slane 2006). But the source still shows emission due to relic electrons which still have enough energy to produce VHE emission. The distance d_{offset} of the pulsar from the center of gravity of the VHE source can be calculated by

$$d_{\mathrm{offset}} = D \sin\theta, \tag{4.1}$$

where D is the estimated distance from the pulsar to Earth and θ is the angular distance between center of gravity of emission and the rotating energy source. Fig. 4.6 shows the offset of the pulsars for different ages. The expected increase of the offset can be confirmed. It has to be noted that the offset is just a projection of a three dimensional distribution. Thus high

aged pulsars can still have small offsets if their motion is along the line of sight.
The parameters σ_1 and σ_2 of the morphology fit can be used to calculate the size of the source. Projected in two dimensions an asymmetrical Gaussian has an elliptical shape. Assuming a circle with the same area, an equivalent radius of the source can be defined as

$$R_{\text{equiv}} = \frac{1}{2}\sqrt{\sigma_1 \sigma_2}\,, \tag{4.2}$$

which allows to study the sources depending on size but not on the structure. A simple transformation as done in Eq. 4.1 returns the radii in units independent from the distance of the source. According to Gaensler & Slane (2006), young PWNe expand freely into their

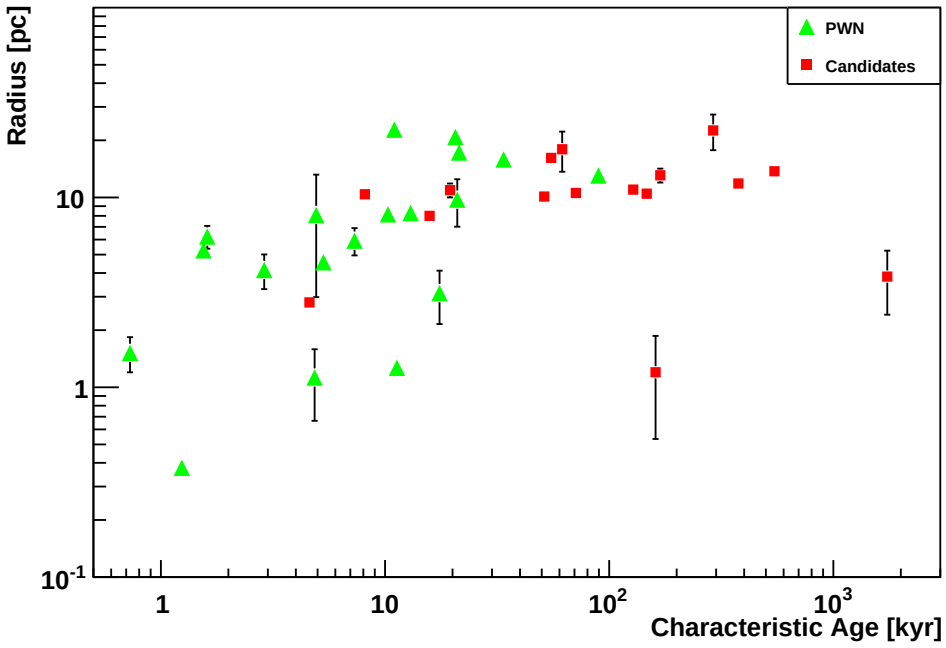

Figure 4.7.: The radii of the PWNe and candidates in units of parsec developing with the age. An increase up to the age of about 10 kyr can be seen. Large errors for some sources can be explained with low statistics on some sources.

surroundings. Following Blondin et al. (2001), interactions between the relativistic Pulsar Wind and the supernova remnant (SNR) Reverse Shock may cause an evolution as seen in Fig. 4.7. This Reverse Shock is formed when the shell of the SNR moves through the interstellar medium (ISM). Heading back, towards the center of the shell, this shock crushes the Pulsar Wind after about 10 kyr resulting in complex structures of the emission regions. A detailed discussion of this phenomenon is given by van der Swaluw et al. (2001). Fig. 4.7 shows an increasing radius for young PWNe associated with the free expansion state. Aged higher than $t_c \approx 10\,\text{kyr}$, the radii of the nebulae stay constant due to a counter pressure by the ISM. The PSF of H. E. S. S. does not allow to resolve some of the considered sources. These point-like PWNe are assumed to have the true size of 0.1° which corresponds to the PSF. The PWN candidate HESS J1832−087 shows a significantly smaller radius compared to the rest of the population with a similar age. Either its distant estimate provided by

radio data contains large uncertainties or the source is not powered by a pulsar leading to a different morphological evolution.

4.3.2. Spectral evolution

The spectral shape may also change during the life of a PWN. As explained in Sect. 3.3.2 three different spectrum shapes were applied to the data. Every model has a characterizing parameter as the photon index for the power law, the curvature for the curved power law and the spectral break energy for the broken power law. These values are listed in Tab. 3.1. Fig. 4.8 shows the evolution of these three parameters. Due to large errors on curvatures and spectral breaks, it is reasonable to regard only the variability of the photon index. Pulsars might have different intrinsic properties responsible for the largely scattered photon indices. About 10 kyr old PWNe show very different steepness of the spectrum ranging from 1.9 to 2.8. One possibility which could explain the large scatter is the index of the injection spectrum differing from $p = 2$ (motivated in Sect. 2.2). Also the present magnetic field inside the PWN has much influence on the spectral behavior. High magnetic fields would cause a strongly cooled lepton population affecting the measured photon index. Probably the initial conditions of a PWN are quite different so that a spectral evolution can not be seen with the present amount of sources. Fig. 4.9 shows the abundance of the measured spectrum parameters. To increase the statistics PWN and PWN candidates are unified for these considerations. The photonindex of the power-law model seems to be distributed uniformly over a range of $[2, 3]$. The curvature, which is the characteristic parameter of the curved power-law, reveals a slight but not significant peak at about $\beta = 0.1$. Statistical limits on the flux may cause large fluctuations on this value ($\beta \in [-0.2, 0.6]$). The spectral break, fitted by the broken power law, constains larger errors (Tab. 3.1). However, most of the fitted break energies are smaller than 4 TeV. There is no clear evidence that pulsars have a certain spectral appearance more often. A higher number of of sources is necessary to manifest trends of the spectrum parameters.

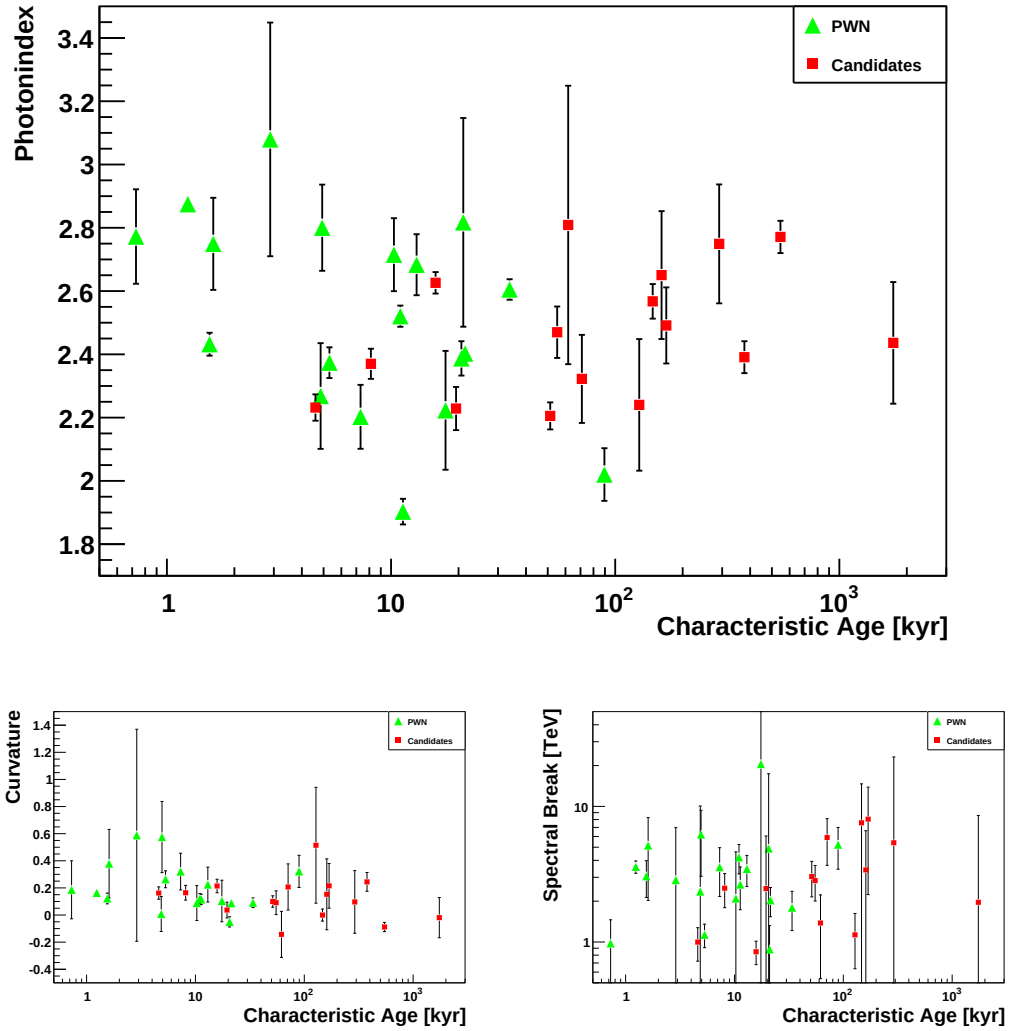

Figure 4.8.: The upper plot shows the spectral index of the photon spectrum fitted by a power law. Its values are plotted against the respective characteristic ages of the pulsars. No evidence for a change with time can be recognized. The development of the parameter curvature of a curved power law is shown bottom, left. The spectral break fitted by the broken power law against the characteristic age is shown bottom, right.

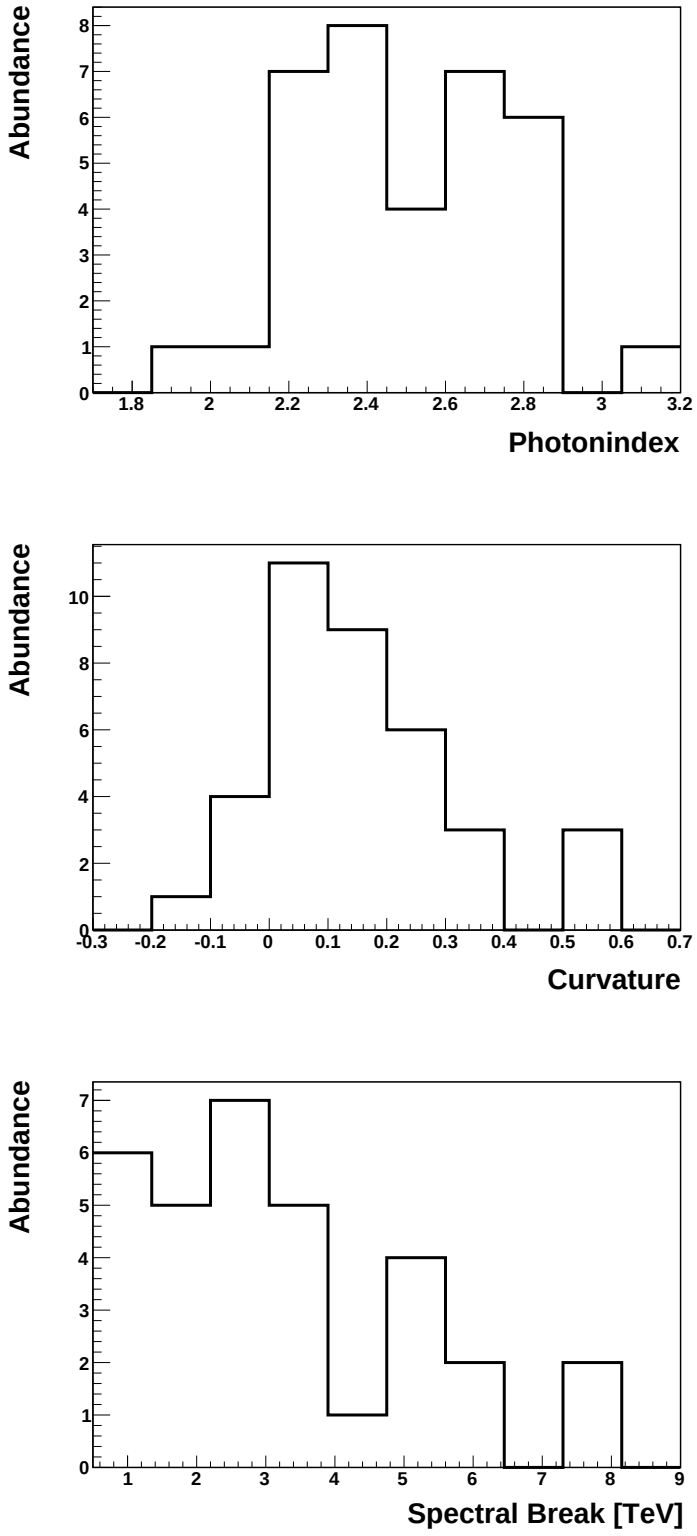

Figure 4.9.: Distribution of the fitted spectral parameters. The abundance of the photonindex is shown in the upper panel. The curvature, fitted by the curved power-law (Eq. 3.4) can be seen in the centr panel. A broken power-law model provides the spectral break energy as characteristic parameter for which the fitted values are shown in the lower panel.

4.3.3. Spin-down luminosity versus photon efficiency

Spectral analyses also allow the determination of the luminosity L_γ of a PWN. The energy range, used to calculate this value, is chosen between 0.5 TeV and 5 TeV which is motivated by relatively small uncertainties within this interval (compare with depicted spectra and residuals in Sect. 3.3.3). Since the spin-down luminosity derived in Eq. 2.7 decreases with

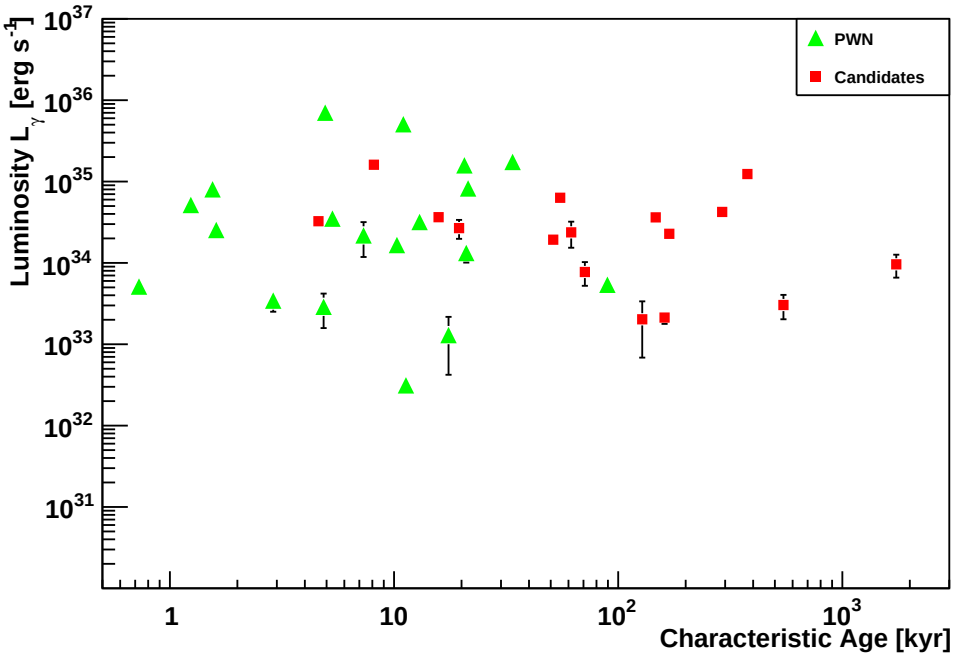

Figure 4.10.: The luminosity of the PWNe and PWN candidates is plotted against their respective characteristic ages.

time it is expected that the source luminosity also decreases. But no significant dependence of the source luminosity on the age of the pulsar can be detected (Fig. 4.10). The reason might be quite simple. PWNe which are darker in the VHE regime can not be detected by H. E. S. S., i.e. only the strongest sources independent from age can contribute to the sample. The conversion efficiency from spin-down power to γ-rays is given by

$$\epsilon = \frac{L_\gamma}{\dot{E}}. \tag{4.3}$$

This parameter of a PWN is influenced by many circumstances such as the density of the ambient photon fields or the conversion efficiency from spin-down luminosity to relativistic particles. Nevertheless this value is expected to increase with time due to relic particles. Accelerated thousands of years ago some leptons could have survived the cooling processes and still contribute to the relativistic Pulsar Wind. Therefore the efficiency would seem higher reflecting an integrated history over the pulsar's spin down (Gaensler & Slane 2006). Fig. 4.11 shows the efficiency dependent on the pulsar's age. Taking the candidates into account reveals older pulsars to have a higher efficiency. But the small amount of identified PWNe does not allow such a conclusion. A larger sample of identified PWNe might help to clarify this effect.

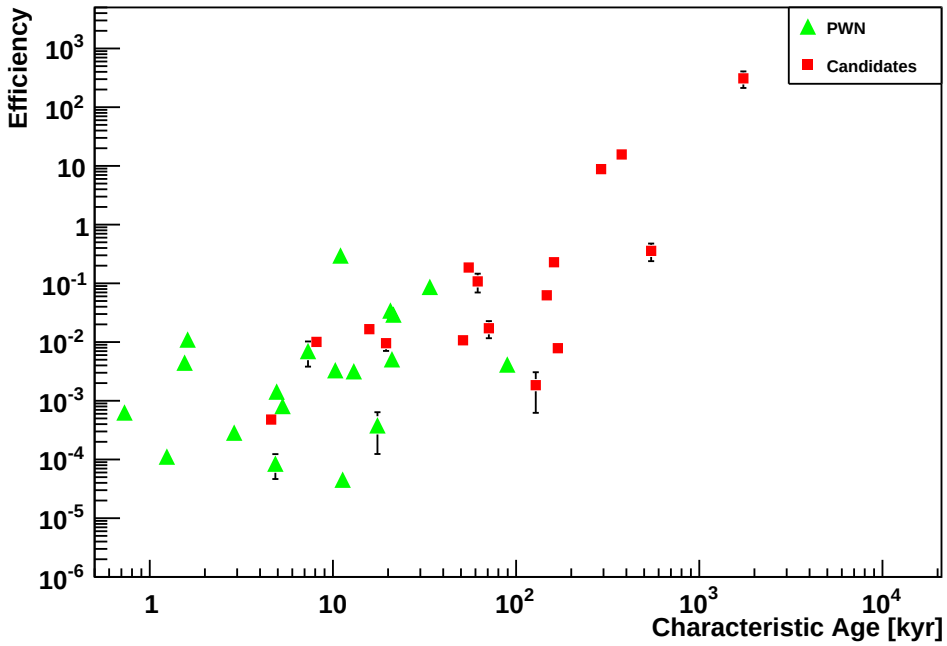

Figure 4.11.: The efficiencies of the PWNe are plotted against their respective characteristic ages. Older Pulsars have higher efficiencies by exceeding the younger ones of some orders of magnitudes.

This Chapter gave an overview of PWNe in the high energy regime. Some criteria for pulsars to generate significant TeV emission were shown, e.g. a small period coincident with a high period derivative. The evolution of the extension of PWNe seems to be dominated by the Reverse Shock above 10 kyr (Fig. 4.7). Remarkably, for some PWN candidates the conversion efficiency exceeds 100 % (Fig. 4.11). However, this could be explained by a large population of relic electrons still contributing to the observed γ-ray emission. The next Chapter will present a simple model of the time evolution of PWNe, helping to understand the development of some parameters and show trends of possible efficiencies.

5. Modeling the evolution of a PWN

To improve the understanding of a PWN and the PWN population in general a model has been constructed to describe the spectral evolution of such a source in the VHE regime. It is based on previous work conducted by Gaensler & Slane (2006), Zhang et al. (2008) and a model developed by Brucker (in prep.). The model is fitted to every PWN and PWN candidate of the sample from Chap. 4 in order to determine starting conditions, like e.g. the period or the magnetic field strength at the pulsar's birth. The first Section of this Chapter explains basic principles of the model. The subsequent Section describes the procedure to calculate the lepton spectrum and the resulting photon spectrum inside the PWNe. Finally, the performance of the model and binning effects are discussed at the end of this Chapter.

5.1. Physics of the model

The model predicts the spectral evolution of a PWN from its birth until today or even beyond if necessary. Time dependent phenomena, e.g. the spin-down luminosity, contribute to the spectrum determination, while spatial evolutions are not considered. The latter depend strongly on specific environmental conditions, e.g. variations of the ambient density of the interstellar medium and can not be reproduced by a general model. Thus the model presented in this thesis is a so called "one-zone model". The particle population forming the relativistic Pulsar Wind is assumed to consist of electrons and positrons only (so called leptonic scenario), while hadrons are not taken into account. The disregard of the hadrons is motivated by the small Klein-Nishina cross section (Eq. 2.18) of protons or atomic nuclei for the Inverse Compton Effect. The model has four free parameters:

- the initial period of the pulsar P_0
- the initial magnetic field B_0 inside the PWN
- the braking index n
- the conversion efficiency η, denoting the fraction of $\dot{E}$ that is converted to relativistic particles.

P_0 and B_0 are free start values serving only to calculate initial conditions of the PWN. The parameters n and η are assumed to be constant with time but different for each PWNe. Starting with these four values the true age τ and the initial spin-down timescale τ_0 can be determined, using Eq. 2.5 and Eq. 2.8, respectively. Additionally, the initial spin-down luminosity $\dot{E}_0$ can be derived, transforming Eq. 2.7 to

$$\dot{E}_0 = \dot{E}(\tau) \cdot \left(1 + \frac{\tau}{\tau_0}\right)^{\frac{n+1}{n-1}}, \tag{5.1}$$

where $E(\tau)$ is the spin down luminosity as measured today. Thus all initial conditions are defined and the model can be used to predict the future development of the particle spectrum.

5.1.1. Determination of the lepton spectrum

The main purpose is to derive the amount of leptons in the Pulsar Wind having a certain energy E at a certain time t. Starting at the birth of the pulsar ($t = 0$), the model will proceed in time stepwise. The step size Δt should be as small as possible to have the maximum accuracy, but must not be too small in order to minimize computation time. Finding suitable values for Δt for different starting conditions will be discussed in detail in Sect. 5.2.2. The energy released by the pulsar within the time interval $[t, t + \Delta t]$ is given by

$$E_{\mathrm{rel}}(t, t + \Delta t) = \int_t^{t+\Delta t} \dot{E}(t')\mathrm{d}t'. \tag{5.2}$$

The fraction of this energy that is converted into kinetic particle energy E_{kin} is then defined as

$$\begin{aligned} E_{\mathrm{kin}}(t, t + \Delta t) &= \eta E_{\mathrm{rel}}(t, t + \Delta t) \\ &= \eta \dot{E}_0 \int_t^{t+\Delta t} \left(1 + \frac{t'}{\tau_0}\right)^{-\frac{n+1}{n-1}} \mathrm{d}t' \\ &= -\frac{1}{2}\eta \dot{E}_0 (n-1) \left[(\tau_0 + t') \left(1 + \frac{t'}{\tau_0}\right)^{-\frac{n+1}{n-1}}\right]_t^{t+\Delta t}. \end{aligned}$$

As introduced in Sect. 2.2, the energy distribution of the leptons follows a power law shape

$$\frac{\mathrm{d}N(E,t)}{\mathrm{d}E} = \Phi(t) \left(\frac{E}{E_{\mathrm{ref}}}\right)^{-p}. \tag{5.3}$$

The index of this lepton spectrum is approximated by $p = 2$, while the reference energy E_{ref} is set to 1 TeV. The normalization Φ can thus be derived in the following way:

$$\int_{E_{\mathrm{min}}}^{E_{\mathrm{max}}} E \underbrace{\Phi(t, t + \Delta t) E^{-2} \mathrm{d}E}_{\mathrm{d}N(E,t,t+\Delta t)} \stackrel{!}{=} E_{\mathrm{kin}}(t, t + \Delta t) \tag{5.4}$$

$$\begin{aligned} \Longleftrightarrow \Phi(t, t + \Delta t) &= E_{\mathrm{kin}}(t, t + \Delta t) \cdot \left(\int_{E_{\mathrm{min}}}^{E_{\mathrm{max}}} E^{-1} \mathrm{d}E\right)^{-1} \\ &= E_{\mathrm{kin}}(t, t + \Delta t) \cdot \left[\ln\left(\frac{E_{\mathrm{max}}}{E_{\mathrm{min}}}\right)\right]^{-1} \end{aligned}$$

During every time interval $[t, t + \Delta t]$ a new lepton population with the time-dependent normalization $\Phi(t, t + \Delta t)$ is injected to the Pulsar Wind. This model only considers leptons between 100 GeV and 1000 TeV. An extension of the spectrum to higher energies does not change the resulting photon spectrum due to a decrease of the Klein-Nishina cross section from Eq. 2.18. Also smaller energies do not contribute to the photons in the H. E. S. S. energy range. According to Zhang et al. (2008) there are only two main processes which affect the leptons: synchrotron cooling and escape losses. Due to ambient magnetic fields the particles loose energy by radiating synchrotron photons (see Sect. 2.3). The synchrotron lifetime τ_{synch} of a lepton is given by Zhang et al. (2008) as

$$\tau_{\mathrm{synch}}(E, t) = 12.5 \cdot \left[\frac{B(t)}{10\,\mu\mathrm{G}}\right]^{-2} \cdot \left[\frac{E_{\mathrm{e}}}{10\,\mathrm{TeV}}\right]^{-1} \mathrm{kyr}. \tag{5.5}$$

This value is time dependent due to a decreasing magnetic field inside the PWN caused by an expanding particle wind. $B(t)$ evolves by definition of Zhang et al. (2008) as

$$B(t) = \frac{B_0}{1 + \left(\frac{t}{\tau_0}\right)^{1/2}} + B_{\mathrm{ism}}, \tag{5.6}$$

where the free model parameter B_0 is the magnetic field at the pulsars birth inside the PWN. B_{ism} is the present magnetic field of the interstellar medium assumed to be $3\,\mu$G. The particle population also looses energy by leptons escaping the Pulsar Wind (see Sect. 2.3). The escaping lifetime (Zhang et al. 2008) is given by

$$\tau_{\mathrm{esc}}(E,t) = 34 \cdot \left[\frac{B(t)}{10\,\mu\mathrm{G}}\right] \cdot \left[\frac{E}{10\,\mathrm{TeV}}\right]^{-1} \cdot \left[\frac{R(t)}{1\,\mathrm{pc}}\right]^{2} \mathrm{kyr}. \tag{5.7}$$

The radius of the PWN $R(t)$ evolves with time in a spherically symmetric case as introduced by Gaensler & Slane (2006)

$$R(t) \propto \begin{cases} t^{11/15} & \text{, for } t \leq \tau_0 \\ t^{3/10} & \text{, for } t > \tau_0 \end{cases} \tag{5.8}$$

Assuming a PWN radius at birth $r_0 \approx 20\,\mathrm{km}$, the coefficients can be calculated considering the present radius of the PWN $R(\tau)$.

$$R(t) = \begin{cases} (R(\tau) - r_0) \cdot \left(\frac{\tau_0}{\tau}\right)^{3/10} \cdot \left(\frac{t}{\tau_0}\right)^{11/15} & \text{, for } t \leq \tau_0 \\ (R(\tau) - r_0) \cdot \left(\frac{t}{\tau}\right)^{3/10} & \text{, for } t > \tau_0 \end{cases} \tag{5.9}$$

The birth radius r_0 was introduced to avoid $R(t) = 0$ for $t = 0$. If the amount of leptons $Q(E,t)$ is given, the new amount of leptons at the time $t + \Delta t$ with the same energy can be determined in the following way:

$$Q(E, t+\Delta t) = \underbrace{Q(E,t) \cdot \exp\left(-\frac{\Delta t}{\tau_{\mathrm{eff}}(E,t)}\right)}_{\text{cooled particles}} + \underbrace{\Phi(t, t+\Delta t)\left(\frac{E}{1\,\mathrm{TeV}}\right)^{-2}}_{\text{new particles}}, \tag{5.10}$$

where $\tau_{\mathrm{eff}}^{-1} = \tau_{\mathrm{esc}}^{-1} + \tau_{\mathrm{synch}}^{-1}$ (Zhang et al. 2008). Starting with $Q(E,0) = 0$, a lepton spectrum can be calculated at an arbitrary time by repeating Eq. 5.10 as often as necessary. For the present spectrum the number of steps N_{time}, required to reach T_{age} is given by

$$\sum_{i=0}^{N_{\mathrm{time}}} \Delta t_i \stackrel{!}{=} T_{\mathrm{age}}. \tag{5.11}$$

In a case of equidistant steps ($\Delta t_i = \Delta t$) the number of steps is $N_{\mathrm{time}} = {}^{T_{\mathrm{age}}}/_{\Delta t}$.

The model allows to simulate time-dependent energy spectra, e.g. for different times in the life of a pulsar. Thus the spectral evolution of the leptonic component of the PWN can be investigated. To get an idea of the "typical" evolution of the lepton spectrum a fictive representative of a PWN will be analyzed in detail. To stay close to reality the values for P,

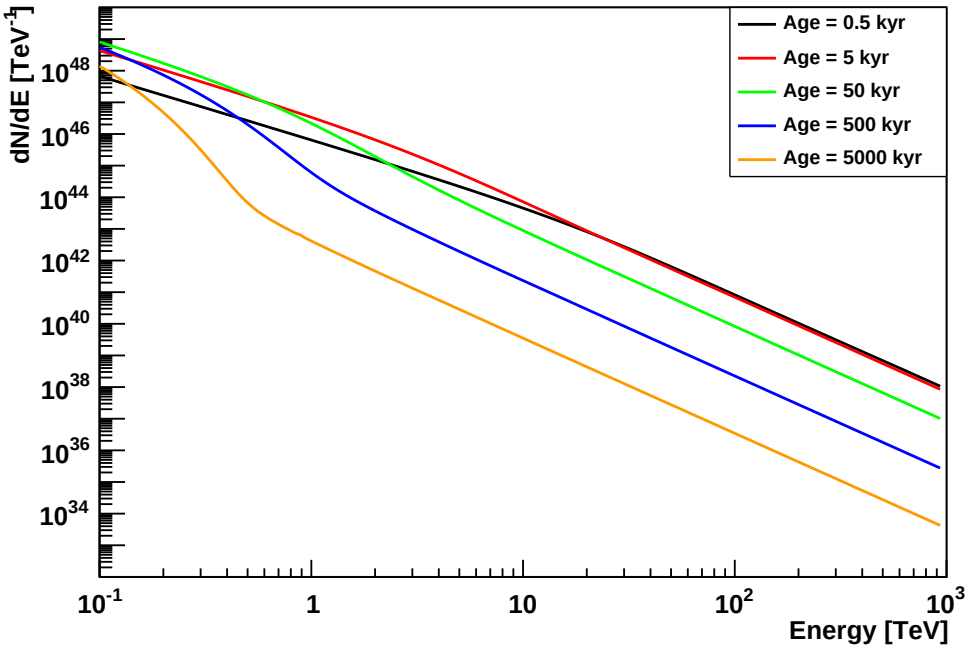

Figure 5.1.: The lepton spectra are shown qualitative for different ages. The cooling effects for higher ages are quite visible by reducing the amount of leptons very much for higher ages.

$\dot{E}(\tau)$, τ_c and $R(\tau)$ were chosen the same as for HESS J1825−137. The free parameters were chosen arbitrarily representing reasonable start values for a pulsar ($P_0 = 50\,\mathrm{ms}$, $B_0 = 50\,\mu\mathrm{G}$, $\eta = 0.2$ and $n = 2.5$). Fig. 5.1 shows the simulated evolution of the resulting lepton spectrum. The comparison of the two youngest spectra (black and red) reveals a strong increase of low energy particles short after birth. The spin-down luminosity is still large at 5 kyr providing enough energy to exceed the cooling effects. At 50 kyr the energy losses have already started to dominate the development of high energy particles (green) while the amount of leptons with less energy still shows a slight increase. Especially high aged distributions (blue and orange) are effected by fresh injected leptons which compensate the energy dependent cooling effects. This can be recognized by the flat component of the particle spectrum at higher energies.

5.1.2. Influence of the model parameters

Each of the parameter influences the resulting lepton spectrum in different ways. The initial period P_0 is expected to affect the results mainly by its impact on the pulsar's true age. The time evolution of the magnetic field probably influences the steepness of the spectrum. Contributing to the age calculation, the braking index n affects the pulsars released energy. In this Section the influence of the parameters on the spectral evolution on the spectral evolution is investigated. The fictive PWN representative introduced above serves again as example. Keeping all other parameters fixed, a single parameter is varied and the effect on the spectral energy distribution is studied after 10 kyr and 100 kyr respectively. Influencing the spectrum only in form of a trivial scaling factor the parameter η is excluded from the

study. As seen in Fig. 5.2 the influence of the braking index after 10 kyr is quite small but not

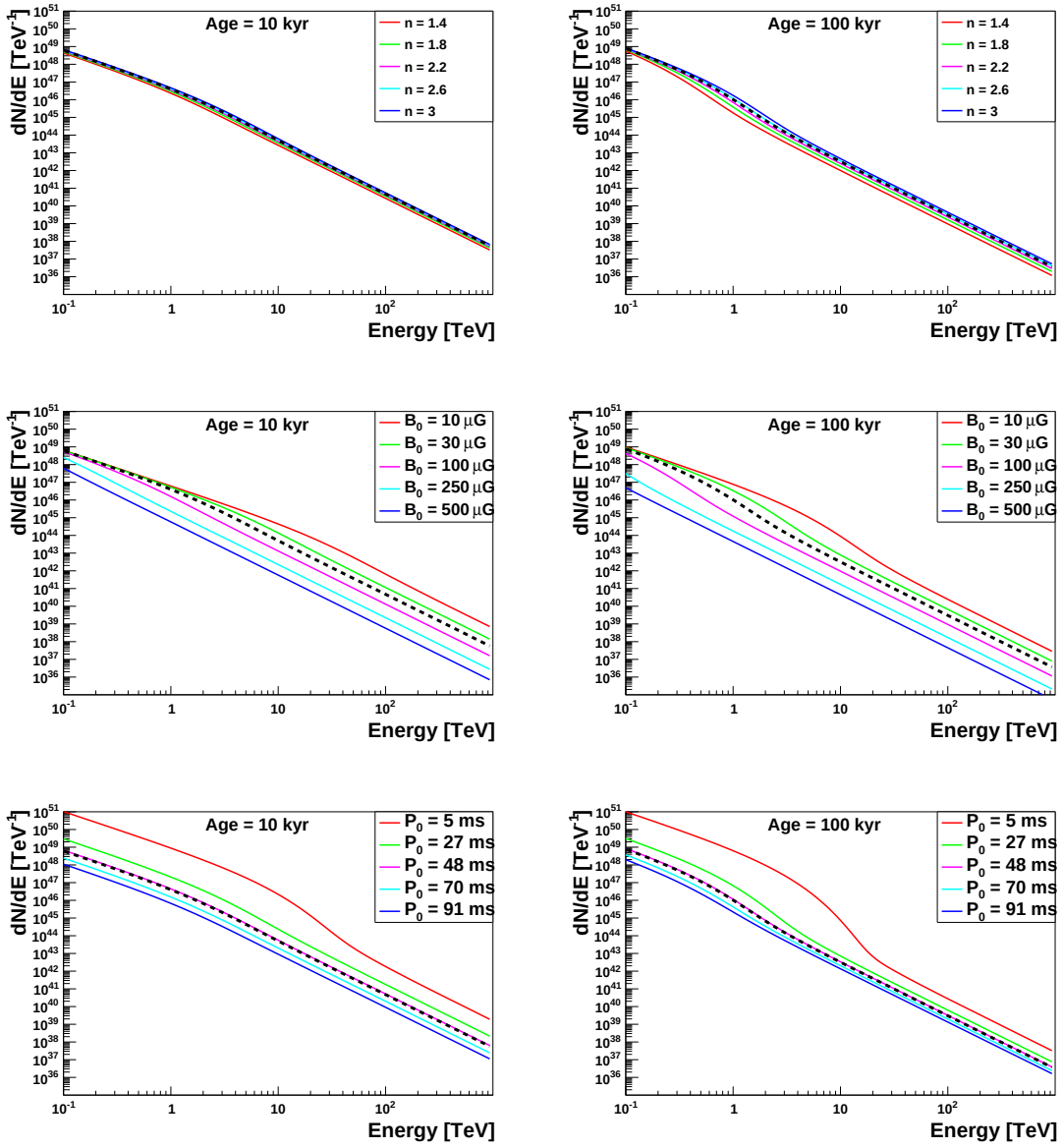

Figure 5.2.: The influence of the parameters braking index n (top), initial magnetic field B_0 (center) and initial period P_0 (bottom) is shown. Their impact after 10 kyr of evolution is shown in the left column while the lepton spectra in the right column are aged 100 kyr. The black dashed lines in every figure show the lepton spectra for the unchanged parameters ($P_0 = 50\,\mathrm{ms}$, $B_0 = 50\,\mu\mathrm{G}$ and $n = 2.5$).

negligible. If the lepton spectrum evolves 100 kyr its impact grows scattering the amount of leptons over more than one order of magnitude. As expected the initial magnetic field changes the shape of the spectrum. Its influence is relatively constant with time. Furthermore the initial period effects a large scattering of the amount of leptons inside the PWN. A small value of P_0 leads to a short initial spin-down timescale τ_0 affecting the energy output. A high

braking index amplifies this effect. A small braking index and a small period increases the true age strongly which leads to a different shape of the spectrum. Thus both parameters are slightly correlated. For the following Chapter, where the model will be fitted to real data, the range of the parameters must be restricted. Due to observational facts the braking index is reduced to an interval between 1.4 and 3. The initial period was determined to be larger than 5 ms but smaller than 90 % of the period today. Only the initial magnetic field can not be constrained. No observation in the VHE regime provides a good estimate for this value. Therefore are large range is chosen between 10 μG and 500 μG. The parameter η was constrained in the interval $[0.01, 0.3]$. After all calculations the lepton spectrum must be converted into a signal which can be detected with the H. E. S. S. telescopes.

5.1.3. Simulation of the photon spectrum in VHE γ-rays

Having determined the lepton spectrum, the next step is to calculate the measurable photon signal on Earth. As motivated in Chap. 2 the dominating process is Inverse Compton scattering of the leptons. In this thesis three different photon fields are taken into account:

- Cosmic Microwave Background (CMB), following a blackbody spectrum with a temperature of $T = 2.725\,\mathrm{K}$
- Starlight photons radiated in the PWN vicinity
- Thermal radiation from dust

The spectral energy distribution of the starlight and dust photon fields can be obtained from the GALPROP Code (Strong et al. 2000), which is a very powerful program for simulating cosmic-ray transport and diffuse emission within the Galaxy. Incorporating as much astrophysical input as possible, the GALPROP Code provides a sophisticated lookup of the photon fields (Porter & Strong 2005) for different positions in the Galaxy. Since the positions are given in radially symmetric cylindrical coordinates (r, z) with its origin in the Galactic Center, a simple geometric conversion of galactic coordinates (λ, β) to the required system is given by

$$r = \left[D^2 \cos^2(\beta) + r_0^2 - 2Dr_0 \cos(\lambda)\cos(\beta)\right]^{1/2} \tag{5.12}$$

$$z = D \sin(\beta), \tag{5.13}$$

where D is the pulsar's distance to Earth and $r_0 = 8.33\,\mathrm{kpc}$ the Earth's distance to the Galactic Center. The transformations allow the approximation of the photon fields for every pulsar located in the milky way. It has to be noted that one pulsar of the sample (PSR J0537−6910) is located in the LMC for which no information about the local photon fields is available. Therefore only CMB is considered in this specific case. Having determined the photon fields, the photon spectrum can be calculated by applying Eq. 2.19 to the lepton spectrum. Finally, the resulting photon spectrum is divided by $4\pi D^2$ to determine the flux detectable on Earth. The influence of the galactic position on the final photon spectrum will be investigated in more detail. Again the values of HESS J1825 − 137 will serve as an example. Fig. 5.3 shows the current spectrum and the spectral energy distribution of this source if these parameters are valid. The photon fields have different influence on the spectrum. Compared to the other radiation fields the influence of the starlight is rather small. The dust component, however, strongly influences the resulting photon field as it dominates the Inverse Compton emission.

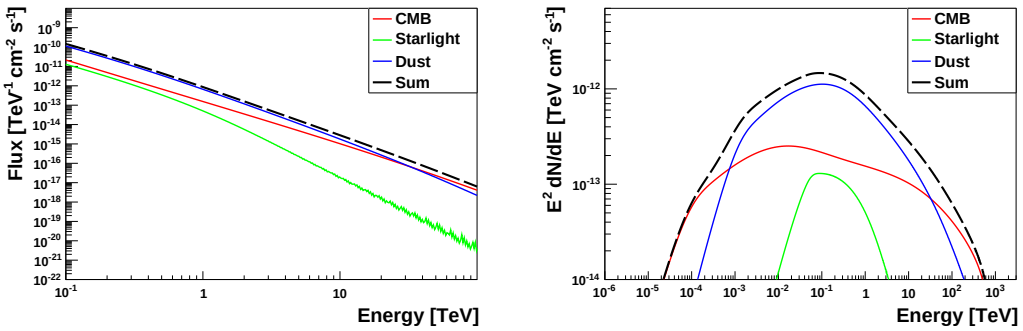

Figure 5.3.: Simulations of the VHE flux for a position near HESS J1825 − 137 for different photon fields. The spectrum in the energy range of H. E. S. S. for the given initial parameters is shown left. A spectral energy distribution plotted right points out the different influences of the radiation fields.

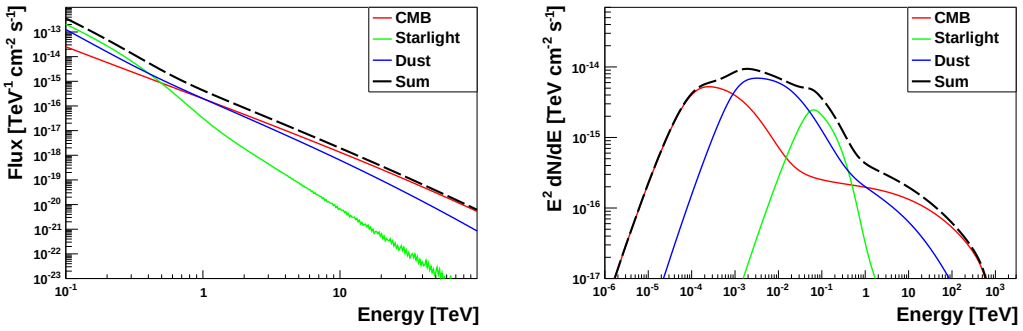

Figure 5.4.: *Left:* Simulated VHE spectrum generated from an older pulsar at the position of HESS J1503−582 with the H. E. S. S. energy range. *Right:* A spectral energy distribution with the parameters given in the text. Every single photon field contributes to the emission in different energy ranges.

The influence of the photon fields varies for different sources. In the case of HESS J1503−582 the starlight leads to a non-negligible contribution to the photon field (see Fig. 5.4). The associated pulsar is very old ($\tau_c = 591\,\mathrm{kyr}$). Therefore the cooling effects induce a plateau from $10\,\mathrm{MeV} - 100\,\mathrm{GeV}$ with a sharp cut off. Fresh injected leptons are responsible for the long tail ($E > 1\,\mathrm{TeV}$) with a low amount of photons.

The previous Sections gave an introduction of a one-zone model created to simulate the spectral evolution of a PWN. It assumes a constant energy range for the accelerated particles $100\,\mathrm{GeV} - 1000\,\mathrm{TeV}$ and a constant index ($p = 2$) of the injected leptons. The background photon fields necessary to simulate the Inverse Compton spectra are taken from the GALPROP Code. They show different energy densities dependent on the galactic position. Before applying the model to the PWN sample, the model's systematics must be analyzed. This will be done in the next Section.

5.2. Performance and binning effects

The goal of this model is to fit the free parameters of all PWNe and candidates. Therefore a fast calculating algorithm is required, yet keeping a maximum of accuracy. Understanding the impact of the calculation precision (binning) on the results is inevitable for finding the optimum balance between precision and computation time.

5.2.1. Energy binning

The energy spectra of the leptons are binned into a histogram. In order to have equidistant steps on a logarithmic scale the step size was also chosen to change with a logarithmic function. The boundaries of the histogram are then given by

$$e_{\min} = \log_{10}(E_{\min}) = -1 \tag{5.14}$$

$$e_{\max} = \log_{10}(E_{\max}) = +3 \tag{5.15}$$

On this logarithmic scale an equidistant binning with an amount of steps $N_{\text{bins}} = {}^{(e_{\max}-e_{\min})}/_{\Delta e}$ is possible. The value of N_{bins} is important for the precision of the resulting lepton spectrum. Fig. 5.5 shows a spectral energy distribution for different numbers of logarithmic energy steps

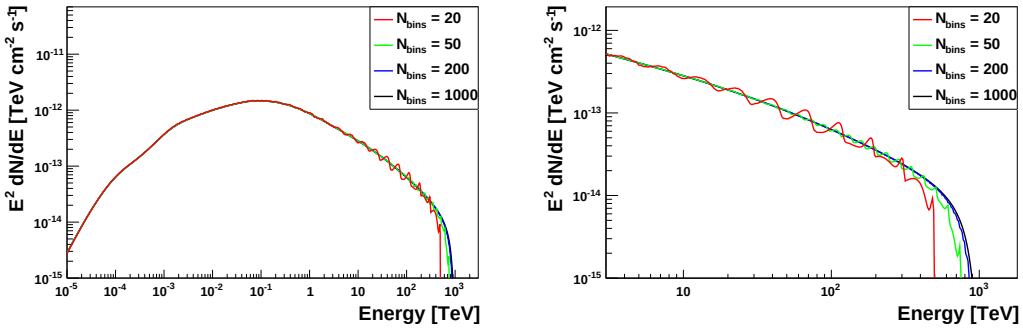

Figure 5.5.: Resulting spectral energy distributions produced with different energy bins. The left picture shows the distribution of the whole energy range. Depicted on the right is a zoom to the energy range where errors occur due to coarse binning.

Δe. A coarse binning results in large fluctuations around the fine binned shape. $N_{\text{bins}} = 200$ seems to be a good trade-off between computation time and precision. This was tested to be independent from the pulsar values and starting conditions.

5.2.2. Time binning

The time step size Δt introduced in Sect. 5.1.1 is free to adjust. A unification of this value for all sources would lead to extremely long calculation times for high aged pulsars. A possible solution is therefore to fix the total number of time steps N_{time} with equidistant sizes required to proceed until the requested age T_{age} is reached by repeating Eq. 5.10. As performed in Sect. 5.2.1 different values for N_{time} can be compared to find the most suitable one. Fig. 5.6 reveals that the deviation between two lepton spectra with different N_{bins} is energy dependent. Consequently, the precision varies within one spectrum, i.e. the inaccuracy increases

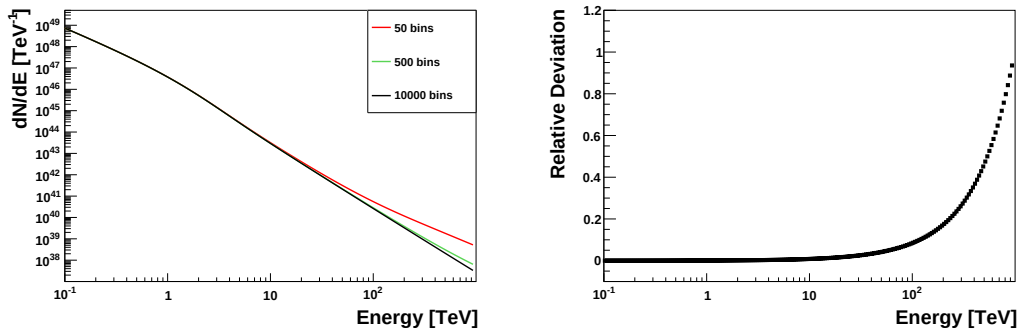

Figure 5.6.: *Left:* Lepton spectra of of a PWN with a true age $\tau \approx 30\,\mathrm{kyr}$ derived by different values for N_{time}. A deviation at higher energies can be recognized. *Right:* Relative deviations between 500 bins and 10000 bins plotted against the energy.

with energy. The problem with a fixed number of time bins is that the spectra of very old PWNe may not be reproduced very well, as the step size gets rather large. For the oldest pulsar of the sample (PSR J1554−5512 with $\tau_c = 1740\,\mathrm{kyr}$) this effect is clearly visible (compare Fig. 5.7). Even a huge number of bins can not handle this parameter combination.

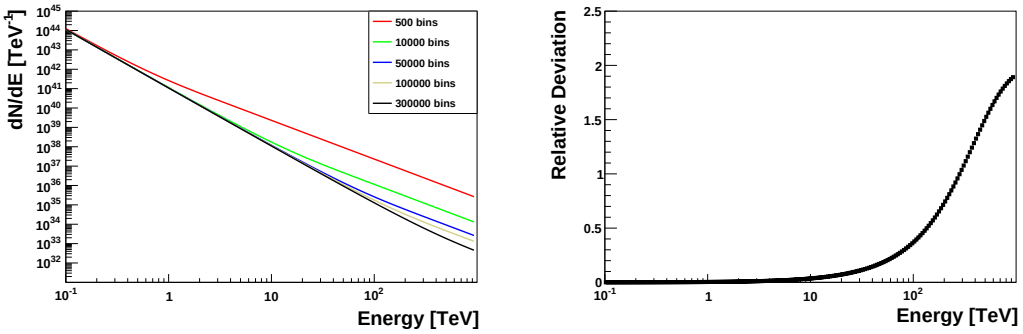

Figure 5.7.: The left figure shows the derived lepton spectra for different numbers of total steps of PSR J1554−5512. Parameters were $P_0 = 5\,\mathrm{ms}$, $B_0 = 500\,\mu\mathrm{G}$, $\eta = 0.2$ and $n = 1.4$ increasing the pulsars true age to $\tau \approx 8000\,\mathrm{kyr}$. The relative deviation between 100000 bins and 300000 bins is shown right.

The relative difference between two fine binned spectra exceeds 100 % for high energies. This deviation is not acceptable to derive unified lepton spectra without binning effects in a short time. Thus the method of equidistant time steps Δt must be rejected and another solution has to be found.

If the last few time steps are quite large they can affect the whole lepton spectrum especially at higher energies. Given an amount of leptons $Q(E,t)$ at the time $t = T_{\mathrm{age}} - \Delta t$, then the last step applying Eq. 5.10 is defined as

$$Q(E, T_{\mathrm{age}}) = Q(E,t) \cdot \exp\left(-\frac{\Delta t}{\tau_{\mathrm{eff}}(E,t)}\right) + \Phi(t, T_{\mathrm{age}}) \left(\frac{E}{1\,\mathrm{TeV}}\right)^{-2}. \tag{5.16}$$

In the case of an old pulsar $Q(E,t)$ might be much smaller than $\Phi(t, T_{\text{age}}) \cdot E^{-2}$. Thus the last time step is dominating the total number of electrons at this time. Only extremely small time steps can avoid this effect by a subsequent increase in calculation time. Therefore a method of adaptive binning was applied. Extensive studies revealed that one solution is to choose an equidistant time binning for $t = 0.95\,T_{\text{age}}$ and a finer binning for $t > 0.95\,T_{\text{age}}$. The limiting condition for the step size at $t > 0.95\,T_{\text{age}}$ is given by

$$\Phi(t, t+\Delta t)\left(\frac{E}{1\,\text{TeV}}\right)^{-2} \leq \kappa Q(E,t), \tag{5.17}$$

with $\kappa = 0.1$, i.e. newly injected leptons must account for at most 10 % of the relic particles. Thus the time step Δt can be decreased until the condition from Eq. 5.17 is met. Furthermore the energy output (see Eq. 5.2) can be approximated by

$$E_{\text{rel}}(t, t+\Delta t) \approx \dot{E}(t)\Delta t \tag{5.18}$$

$$\Longrightarrow \Phi(t, t+\Delta t) \approx \eta \dot{E}(t)\Delta t \cdot \left[\ln\left(\frac{E_{\text{max}}}{E_{\text{min}}}\right)\right]^{-1}, \tag{5.19}$$

which is a quite good assumption for small values of Δt. Combining Eq. 5.17 and Eq. 5.19 an expression for the new time step size can be derived

$$\eta \dot{E}(t)\Delta t \cdot \left[\ln\left(\frac{E_{\text{max}}}{E_{\text{min}}}\right)\right]^{-1}\left(\frac{E}{1\,\text{TeV}}\right)^{-2} \leq \kappa Q(E,t)$$

$$\Leftrightarrow \Delta t \leq \frac{\kappa Q(E,t)}{\eta \dot{E}(t)} \cdot \left[\ln\left(\frac{E_{\text{max}}}{E_{\text{min}}}\right)\right]\left(\frac{E}{1\,\text{TeV}}\right)^{2}. \tag{5.20}$$

This time step is also energy dependent, i.e. for every certain energy the last few time steps are different. The amount of equidistant time steps before the adaptive binning starts is chosen to be $N_{\text{time}} = 500$. This value allows fast computation speed and good accuracy.
To illustrate the advantage of adaptive binning both methods are compared in Fig. 5.8. A large number of equidistant time steps is necessary to get the same accuracy as the adaptive time binning. Hence last-mentioned method is applied to further simulations.

A simple one-zone model considering the spectral evolution of a PWN was presented in this Chapter. Its goal is the description the different evolutionary states of a PWN photon spectrum in the VHE regime. After the physical principles of the model were shown, the parameter influences were investigated in detail (Sect. 5.1). The subsequent Sect. 5.2 focused on the model systematics. Extensive studies revealed a method of adaptive binning which reduces computation time by increasing accuracy. The next Chapter discusses the results provided by the model.

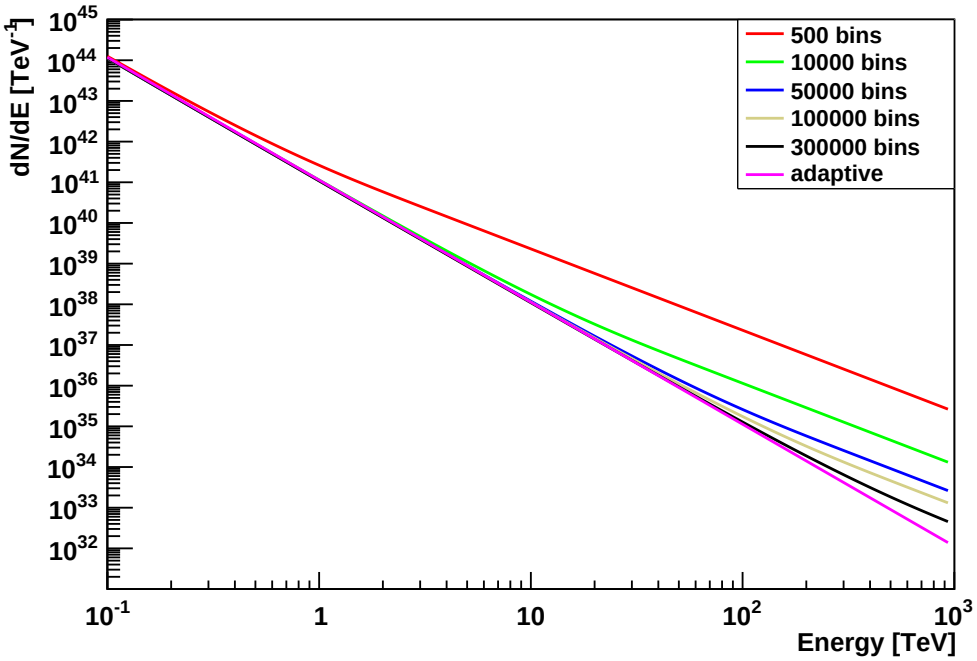

Figure 5.8.: Lepton spectra of PSR J1554−5512 derived by $P_0 = 5\,\mathrm{ms}$, $B_0 = 500\,\mu\mathrm{G}$, $\eta = 0.2$ and $n = 1.4$. The spectra calculated with different bin size are shown compared to the adaptive binning method.

6. Results of the model

The previous Chapter introduced a way to model the VHE photon spectrum of a PWN. Performance and physical principles of the model were discussed in detail. This Chapter applies the model to the measured H. E. S. S. data analyzed with the Model++ technique (see Sect. 3.3). The first Section shows the derived results and discusses their reliability. Subsequently an overview of the fitted spectral energy distributions is given. Moreover some predictions for the future development of PWNe simulated by the model are shown. The last Section of this Chapter tries to exclude or confirm PWN scenarios for the PWN candidates.

6.1. Fit values for the free parameters

The model as introduced in Chap. 5 was fitted to the known PWNe, as well as to the PWN candidates. To find the most suitable parameter set, (P_0, B_0, n, η) the minimization algorithm of ROOT[1] was used. The best fitting values of the parameters are determined via the minimization of the χ^2 defined by

$$\chi^2 = \sum_{i=0}^{N} \left(\frac{F(E_i) - M(E_i)}{\Delta F(E_i)} \right)^2 , \tag{6.1}$$

where $F(E_i)$ and $M(E_i)$ are the measured and the modeled flux at energy E_i, respectively. $\Delta F(E_i)$ is the corresponding uncertainty of the measured value. The goodness of a fit can be given by the value $\chi^2_{\mathrm{red}} = \chi^2/(N-m-1)$, where N is the number of measured values and m the number of the degrees of freedom of the fitting function. For some PWN there exist good estimates of the braking indices. In such a case the number of free parameters is reduced to three by setting the braking index to the measured value. Additionally, the Crab Pulsar with a known true age allows the determination of its initial period (Eq. 2.5).

The fitted parameters are investigated with respect to their abundances. Most of the fitted values reached the boundaries of the defined parameter limits. Fig. 6.1 shows the abundances of all four parameters, where PWN and PWN candidates are considered separately. The initial periods have small values in general. Many of the fitted values are only slightly larger than the lower limit of 5 ms. An initial magnetic field of 10 μG is the most common fitted value for B_0. Most of the candidates are explained with this value. As discussed in Sect. 5.1.2, the influence of the initial magnetic field does not change significantly with time. A small fitted magnetic field may occur due to bad-matching power-law spectra derived from Model++.This might be caused by low statistics on the specific source. The next discussed parameter, the braking index, has a much smaller impact on the spectrum than B_0 (Sect. 5.1.2). Therefore the resulting photon spectrum does not change much by varying this value and the fit is not constrained. A slight change in the initial period, e.g. can cause another good fitting braking index. Thus this value is not very reliable and is only considered to be part of the fine-tuning.

[1] `http://root.cern.ch/`

H. E. S. S. source	P_0 [ms]	B_0 [μG]	n	η	reduced χ^2
HESS J0534 + 220	18.5*	111.6	2.5[0]	0.054	1040.68
HESS J0536−691	5	55.8	3	0.125	7.53
HESS J0835−455	84.9	14.6	1.4[1]	0.037	3.3
HESS J1018−589	8.6	62.7	2.41	0.133	0.12
HESS J1119−614	21.4	406.1	2.91[2]	0.3	1.85
HESS J1303−631	8.4	10	1.54	0.3	5.89
HESS J1356−645	67	14.6	1.4	0.3	1.71
HESS J1418−609	15.8	84	2.25	0.259	0.51
HESS J1420−607	7.1	73.6	3	0.01	0.12
HESS J1514−591	32.8	132.5	2.84[3]	0.3	0.35
HESS J1708−443	92.4	53.5	2.22	0.3	0.35
HESS J1718−385	70.9	10	1.4	0.224	1.89
HESS J1747−281	9.5	86.8	3	0.01	2.81
HESS J1825−137	25	14.1	1.4	0.3	3.2
HESS J1833−105	48.6	163.5	1.44	0.3	0.23
HESS J1837−069	14.2	10	1.4	0.3	1.73
HESS J1846−029	41.1	498.6	2.65[4]	0.3	0.64
HESS J1857 + 026	18.5	10	1.43	0.3	4.79
HESS J1930 + 186	6.9	68.2	1.4	0.018	0.18

Table 6.1.: List of fitted parameters for every PWN of the sample. Errors on the fit parameters are negligible and therefore not listed. The column on the far right shows the goodness of the fit represented by $\chi^2_{\mathrm{red}} = \chi^2/\mathrm{d.o.f.}$. Observed values of braking indices fixed during the fit are marked by a reference note. Additionally the initial period of the Crab (HESS J0534 + 220), marked by a star, is given by its known true age of 956 yr (Eq. 2.5). References: [0] Lyne et al. (1988), [1] Lyne et al. (1996), [2] Camilo et al. (2000), [3] Kaspi et al. (1994), [4] Livingstone et al. (2006).

H. E. S. S. source	P_0 [ms]	B_0 [μG]	n	η	reduced χ^2
HESS J1406−613	19.4	10	1.71	0.3	0.14
HESS J1503−582	6.3	10	2.78	0.033	1.71
G327.1−1.1	9.8	59.4	3	0.3	9.5
HESS J1614−518	5	10	3	0.019	13.12
HESS J1616−508	9.6	13.9	1.4	0.04	0.19
HESS J1702−420	29.4	10	2.03	0.3	5.01
HESS J1745−303	10.2	10	3	0.01	22.01
HESS J1804−216	7.1	14.7	1.4	0.016	0.62
HESS J1809−193	54.2	14.1	2.92	0.205	0.03
HESS J1813−178	12.4	58.6	3	0.01	0.41
HESS J1831−095	58.3	32.2	1.79	0.3	0.18
HESS J1832−084	41.6	31.0	3	0.3	3.25
HESS J1834−087	20.8	10	2	0.3	3.77
HESS J1858 + 020	63.9	10	1.4	0.3	0.53
HESS J1908 + 063	50.8	12.1	1.4	0.3	3.29
HESS J1912 + 101	11.3	10	3	0.033	1.2

Table 6.2.: As shown in Tab. 6.1 the fitted parameters of the PWN candidates and the respective value of the reduced χ^2 representing the goodness of the fit.

A similar effect can be seen, considering the conversion efficiency η. This parameter is also mainly clustering at the definition boundaries. A slight change in the initial period or the magnetic field may cause strongly differing conversion efficiencies. Consequently the parameter η and n have a small influence on the resulting lepton spectrum an thus show a large range of fitted values. Setting these parameters to a fixed value during the fit could be a future project to enhance the model performance. The determination of the free parameters allows to derive other values of the pulsars. Tab. 6.3-6.4 show the true age τ (Eq. 2.5), the initial spin-down timescale τ_0 (Eq. 2.8) and the derived initial spin-down luminosity $\dot{E}_0$ (Eq. 5.1).

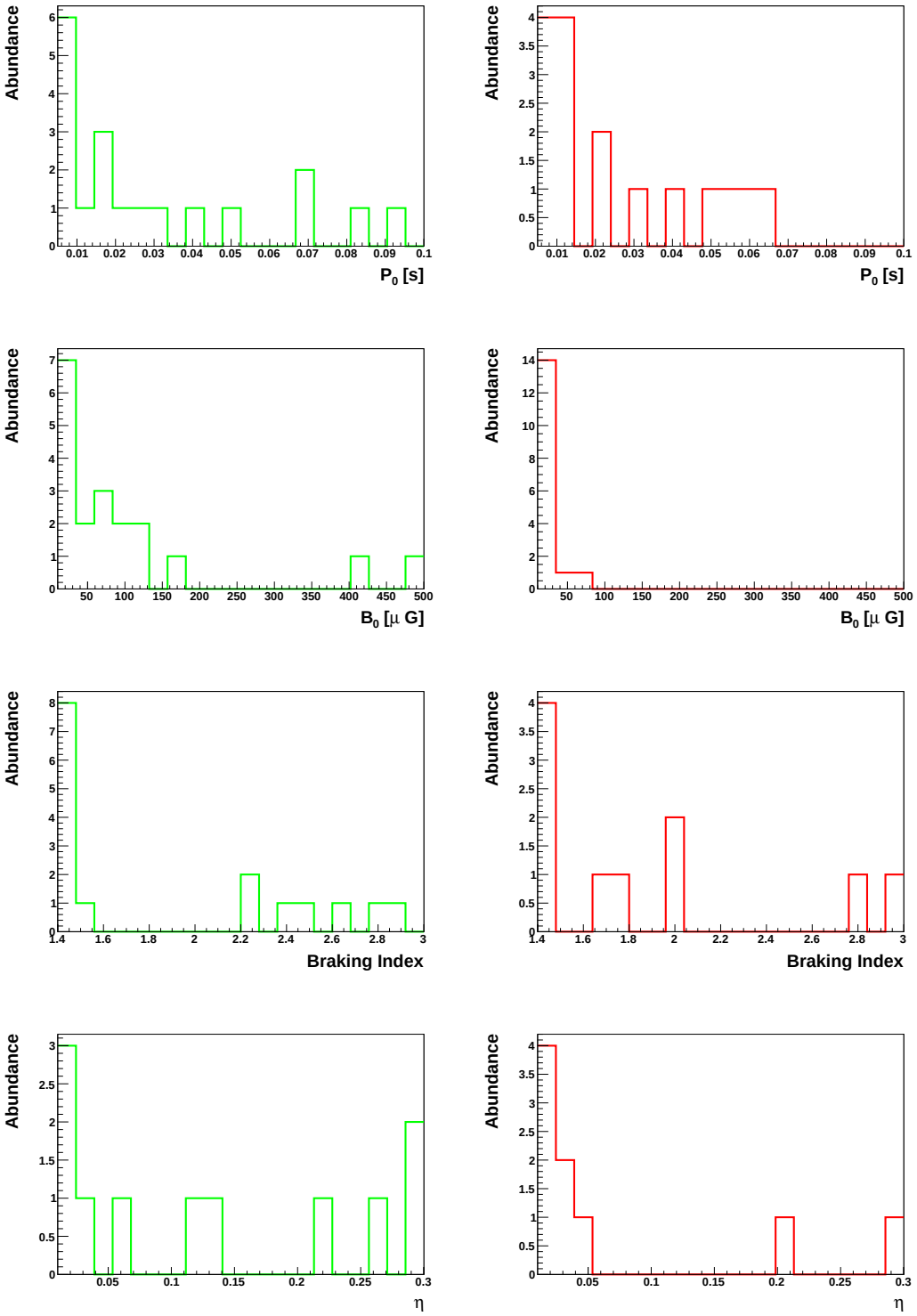

Figure 6.1.: The distribution of the fitted parameters from top to bottom: P_0, B_0, n, η. The left panels show the identified PWNe and the PWN candidates are depicted on the right column.

H. E. S. S. source	τ [kyr]	τ_0 [kyr]	$\dot{E}_0$ [erg/s]
HESS J0534 + 220	0.96	0.69	$3.5 \cdot 10^{39}$
HESS J0536−691	4.46	0.47	$5.3 \cdot 10^{40}$
HESS J0835−455	1.15	55.35	$7.8 \cdot 10^{36}$
HESS J1018−589	28.91	0.85	$1.4 \cdot 10^{40}$
HESS J1119−614	1.68	0.01	$2.3 \cdot 10^{41}$
HESS J1303−631	33.15	7.73	$4.4 \cdot 10^{39}$
HESS J1356−645	11.13	25.42	$2.7 \cdot 10^{37}$
HESS J1418−609	15	1.43	$2.8 \cdot 10^{39}$
HESS J1420−607	12.86	0.14	$8.5 \cdot 10^{40}$
HESS J1514−591	1.59	0.1	$6.3 \cdot 10^{39}$
HESS J1708−443	3.39	25.32	$4.7 \cdot 10^{36}$
HESS J1718−385	9.09	438.41	$1.5 \cdot 10^{36}$
HESS J1747−281	5.13	0.18	$3.9 \cdot 10^{40}$
HESS J1825−137	45.95	61.05	$8.1 \cdot 10^{37}$
HESS J1833−105	2.22	19.58	$6.1 \cdot 10^{37}$
HESS J1837−069	90.3	77.52	$2.0 \cdot 10^{38}$
HESS J1846−029	0.85	0.03	$1.5 \cdot 10^{40}$
HESS J1857 + 026	45.11	51.01	$1.7 \cdot 10^{38}$
HESS J1930 + 186	10.07	4.38	$1.6 \cdot 10^{40}$

Table 6.3.: The true age τ, the initial spin-down timescale τ_0 and the initial spin-down luminosity $\dot{E}_0$, derived by the fitted values.

The reliability of the fitted parameters has to be investigated carefully. Based on the decreasing spin-down luminosity with time the characteristic age can be replaced by the simulated true age and hence can be compared to the shape of Fig. 4.4. Fig. 6.2 shows the still the

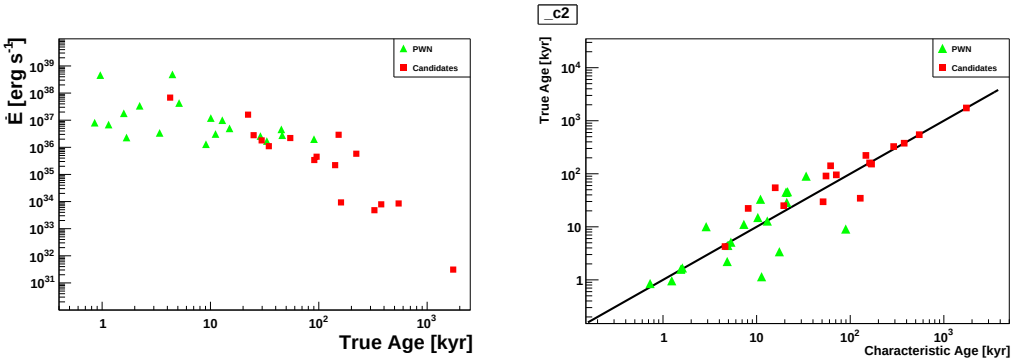

Figure 6.2.: The left plot shows the spin-down luminosities of the pulsars plotted against their simulated true age. The latter value compared to the estimated characteristic age is shown right. Shown in black is the case of equal characteristic and true age.

expected behavior of a decreasing $\dot{E}$. A strong correlation between the characteristic and the simulated age of the pulsar can be seen, too. Fitting a straight line to the values provides a slope of 1.003 ± 0.017. Thus the model reconstructs ages similar to the estimate given by Eq. 2.6. Consequently the constraints on the free parameters in Sect. 5.1.2 helped to determine physically relevant values. The difference between the characteristic age and the

H. E. S. S. source	τ [kyr]	τ_0 [kyr]	$\dot{E}_0$ [erg/s]
HESS J1406−613	141.51	31.25	$1.5 \cdot 10^{38}$
HESS J1503−582	326.06	0.08	$2.2 \cdot 10^{41}$
G327.1−1.1	1739.99	0.01	$4.5 \cdot 10^{41}$
HESS J1614−518	376.96	0.05	$5.5 \cdot 10^{41}$
HESS J1616−508	22.24	18.41	$1.9 \cdot 10^{39}$
HESS J1702−420	90.85	16.46	$8.5 \cdot 10^{37}$
HESS J1745−303	545.6	0.42	$1.4 \cdot 10^{40}$
HESS J1804−216	54.53	24.46	$2.5 \cdot 10^{39}$
HESS J1809−193	29.68	23.74	$9.4 \cdot 10^{36}$
HESS J1813−178	4.25	0.35	$1.1 \cdot 10^{40}$
HESS J1831−095	34.57	290.71	$1.6 \cdot 10^{36}$
HESS J1832−084	160.33	0.66	$5.5 \cdot 10^{3}$
HESS J1834−087	221.86	71.05	$4.0 \cdot 10^{37}$
HESS J1858 + 020	95.43	259.57	$2.9 \cdot 10^{36}$
HESS J1908 + 063	25.03	71.94	$1.7 \cdot 10^{37}$
HESS J1912 + 101	152.38	16.63	$3.0 \cdot 10^{38}$

Table 6.4.: Compared to Tab. 6.3 the derived values of the fitting procedure for the PWN candidates. Calculated are the true age τ, the initial spin-down timescale τ_0 and the initial spin-down luminosity.

simulated true age is very small for younger and also for extremely old pulsars. Since $P_0 \approx P$ for younger pulsars the relative deviation might be larger, but not visible on the logarithmic scale. For old pulsars $P_0 \ll P$ is a good approximation due to the long spin-down evolution. The reduced χ^2 values allow conclusions about the goodness of the fits. Large values reveal bad matching spectra, i.e. the model was not able to reproduce the measured signal properly. Either the model is not a good approximation for some evolutionary states of a PWN or the considered source is not powered by a pulsar. Most reduced χ^2 values have been determined between 0.1 and 10. But $\chi^2_{\text{red}} \approx 10$ is quite seldom. The most frequent values are in the order of 1 or smaller. A small value of χ^2_{red} reveals large errors in the spectrum fit itself. Fig. 6.3 shows the abundance of the reduced χ^2 and also the dependency of the age of the PWNe. There is no evidence that a certain true age or characteristic age is reproduced worse. It has to be noted that the spectra calculated by the Model++ analysis technique might not reflect the exact true shape of the photon energy distribution because only three different spectral models were applied in this thesis. Some spectra might have different shapes, but the χ^2 values of the spectrum fit usually hints to a good agreement of data and the used spectral model, given in Tab. 3.1. Fig. 6.4 and Fig. 6.5 show for two sources (HESS J1825−137 and HESS J1514−591) a comparison between th measured data and the results of the modeling. Both sources are well described by the model. Thus it seems that a simple time dependent one-zone model is to be a good approximation for these extended PWNe and their emission in the VHE regime. The young and energetic Crab Nebula (see Fig. 6.6), however, is badly reproduced by the model ($\chi^2/\text{d.o.f.} \approx 10^3$). An explanation can be given by the synchrotron self-Compton process (see Sect. 2.4), which is not included in the model calculations. Due to the bright synchrotron nebula in X-rays a non-negligible photon field might cause significant energy losses to the leptons by the Inverse Compton effect. Therefore the model will simulate the spectrum too flat for this source. This expectation is confirmed by Fig. 6.6. The model can not reproduce such a steep spectrum for that PWN. The source HESS J0536−691 which

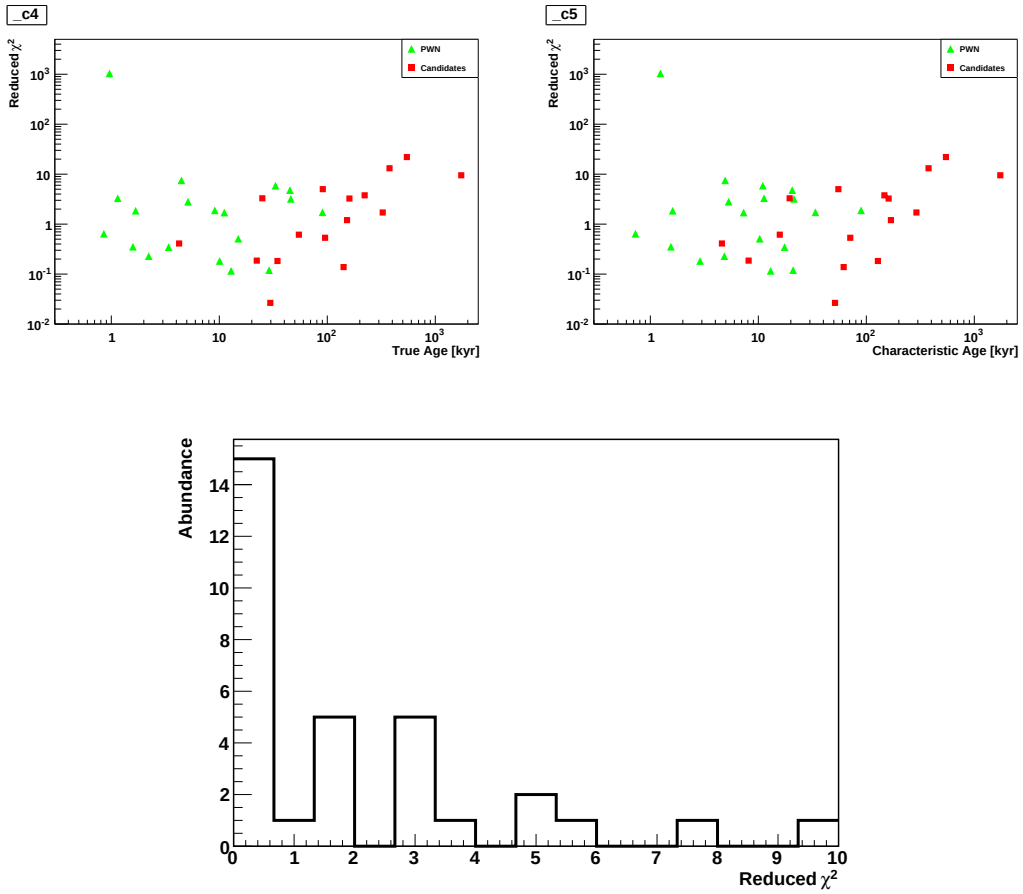

Figure 6.3.: The reduced χ^2 values of the fits are shown in both upper figures. Most identified PWN have values between 0.1 and 10. For comparison this value is plotted against the true age (right) and the characteristic age (left). The abundance of the χ^2_{red} values is plotted on the bottom. Most values are smaller than 1.

is also powered by a very young and energetic pulsar in the LMC shows indications of the same effect. Due the distance of this pulsar, the error bands are relatively large, leading to a better fit ($\chi^2_{\text{red}} = 7.53$) than for the Crab Nebula. More young fast-rotating neutron stars with high spin-down luminosities contributing to the sample are required to point out whether this is a systematic effect on this evolutionary state of PWNe. But it seems that SSC is a non-negligible process inside a young energetic PWN.

In this Section first results produced by the model were shown. Small values of the reduced χ^2 lead to the assumption that the model is a quite good approximation to the measured data for many sources. The following Section will show several spectral energy distributions. Furthermore the spectrum will be simulated to lower energies giving an additional view on X-ray emission.

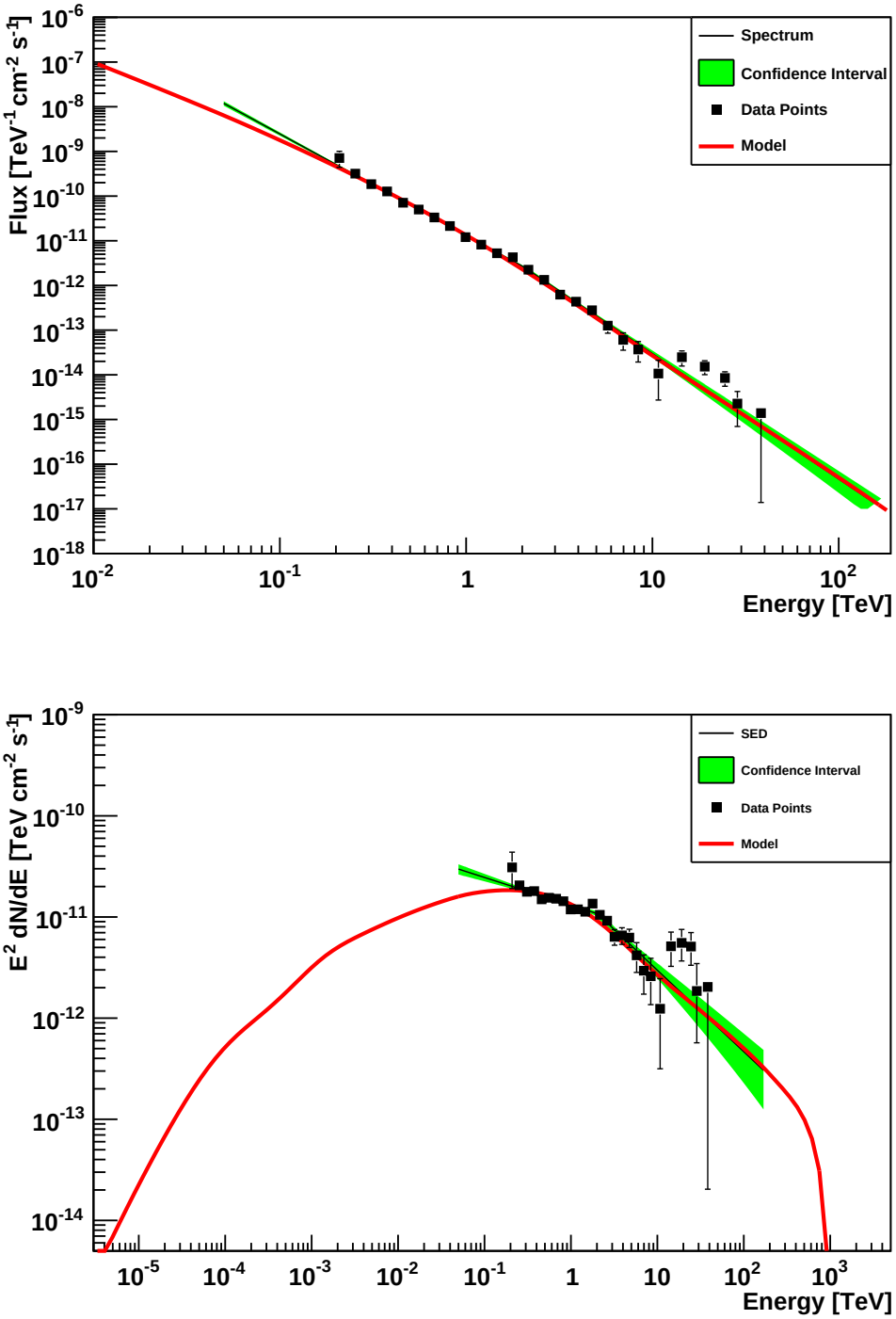

Figure 6.4.: The simulated spectra of HESS J1825 − 137 (upper panel) compared to the H. E. S. S. measurement. The free parameters were fit to a broken power law which is the most suitable spectral model of the source. Note: the data points are calculated by Model++ via forward folding, after the fit of the spectral model has converged. The spectral energy distribution (lower panel) shows how Inverse Compton emission behaves in the lower energy range.

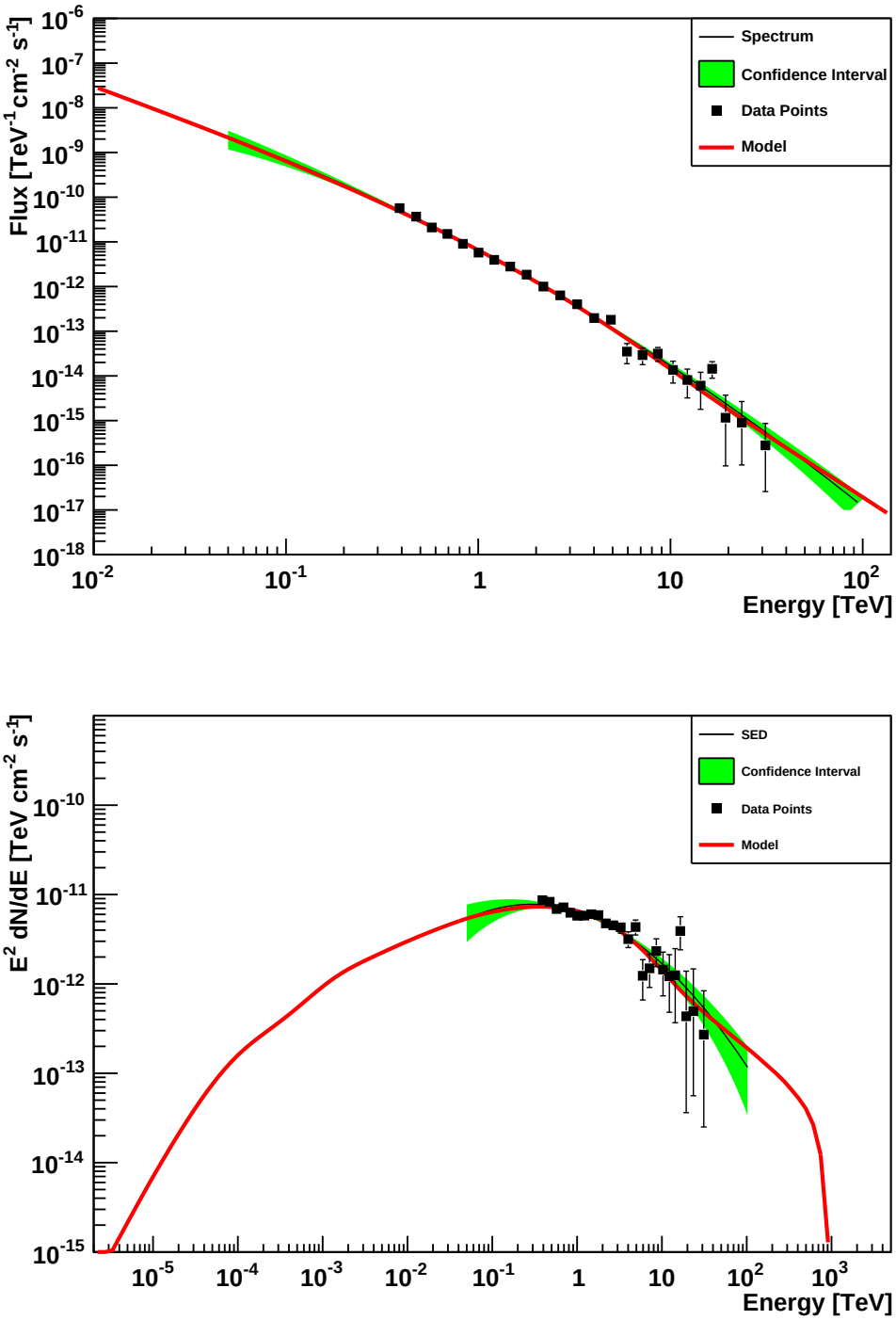

Figure 6.5.: The PWN MSH 15−52 (also called HESS J1514−591) with a curved power law spectrum and model simulations for a certain set of free parameters (top panel). A comparison of the model results to the spectral energy distribution is shown (lower panel).

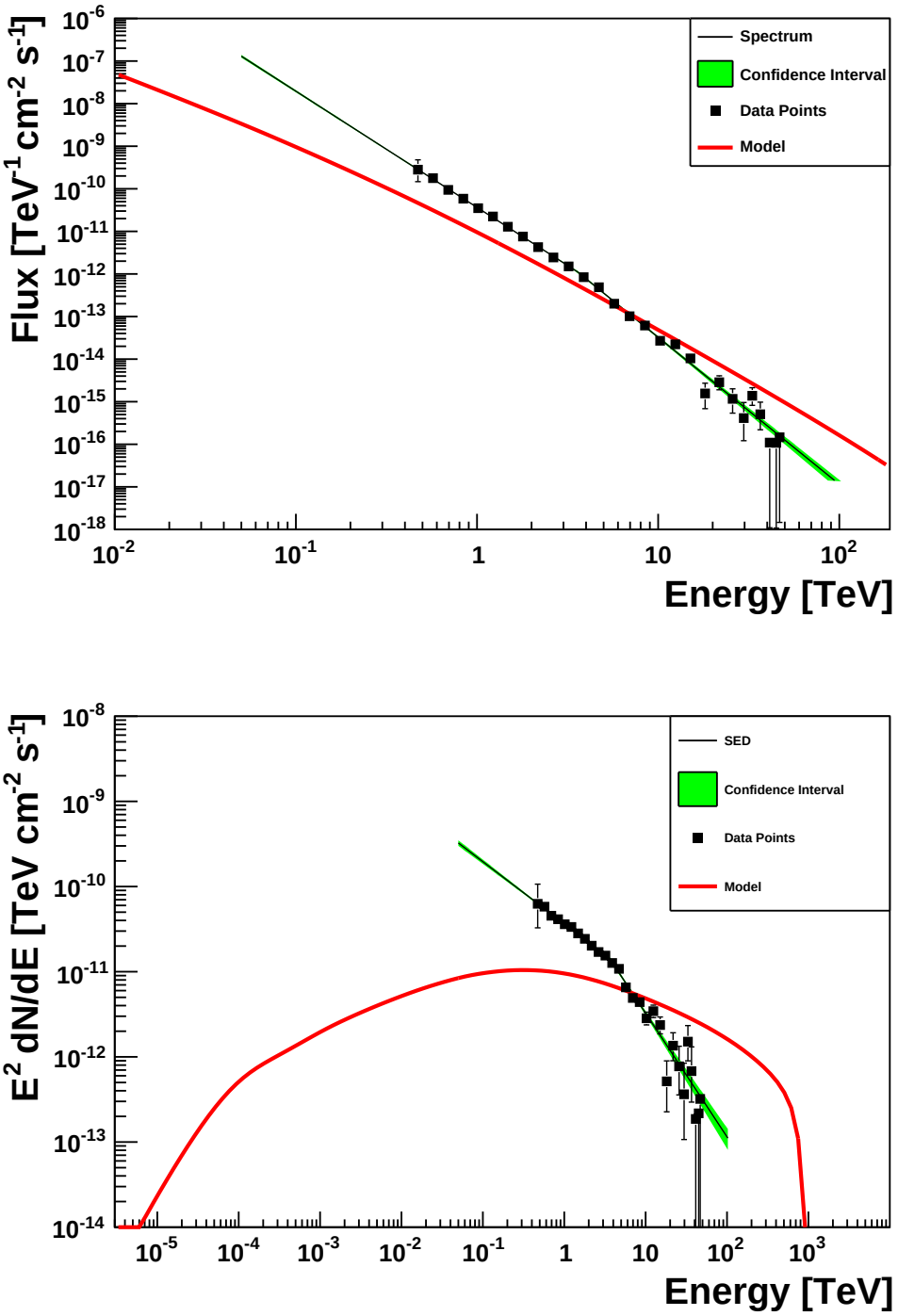

Figure 6.6.: The simulated spectrum of the Crab Nebula compared to the measured one (upper panel). A huge deviation in the steepness can be recognized. The spectral energy distribution of the Crab Nebula can be seen below. This figure reveals the wrongly reconstructed spectrum.

6.2. Spectral energy distribution compared to the measurements

In the previous Section results of extensive fits of the free parameters have been presented. The majority of the population of PWNe and their spectral behavior can be well described by the model (except the Crab Nebula and HESS J0536−691). Further spectral energy distributions are shown in this section to gain an overview of the analyzed and modeled sources. Fig. 6.7 shows four different sources with their data compared to the model. Different spectral

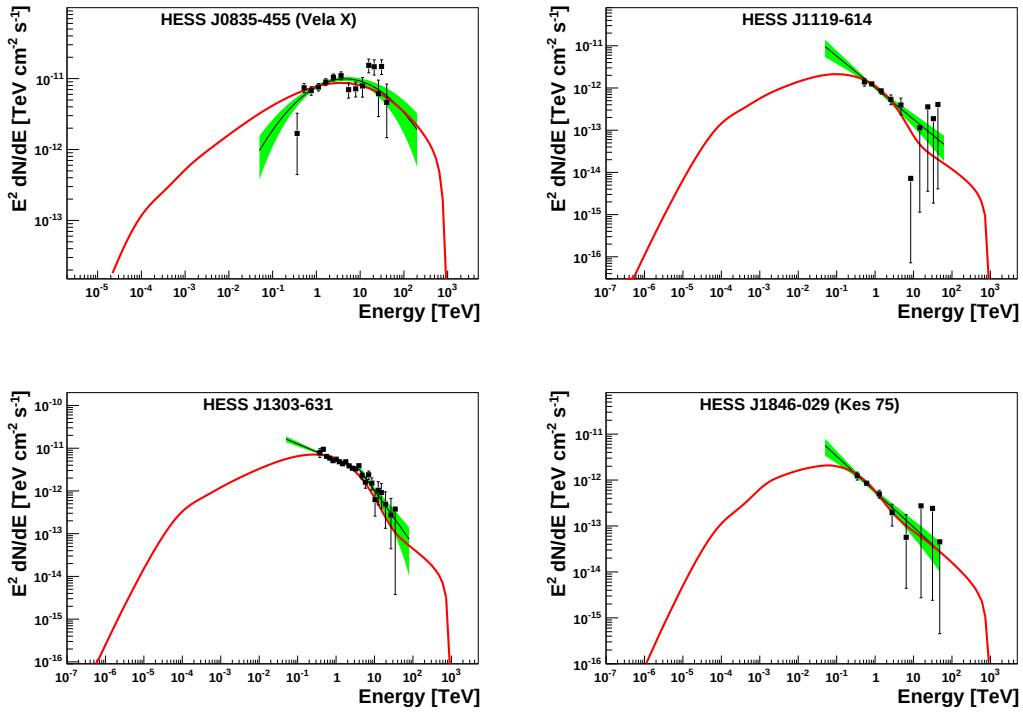

Figure 6.7.: Several spectral energy distributions of identified PWNe. The sources are HESS J0835−455 (top, left), HESS J1119−614 (top, right), HESS J1303−631 (bottom, left) and HESS J1846−029 (bottom, right). All simulated distributions fit well to the measured signals. The 1 σ confidence interval (green) represents the error bands on the spectral model (black line). The data points (black squares) are derived by the folding method after the fit (de Naurois 2010). Shown in red is the model calculation with the best fitting parameters.

shapes are well reconstructed by the model. The PWN candidates were also simulated with the model for the purpose of investigating their origin. HESS J1809−193 e.g. is well approximated by the model. A bad fit ($\chi^2 \gg 1$) with parameters reaching definition boundaries leads to the conclusions of a non-PWN scenario or a special PWN which is unique due to environmental facts and other physical processes not considered by the model. Four spectral energy distributions of PWN candidates are shown in Fig. 6.8 showing that some sources are not well explained by the model. Especially the sources HESS J1745−303 and G327.1−1.1 show a large deviation from the best model fit. The spectral shape can not be reproduced by the model without leaving the defined boundaries of the parameters. The PWN candidate HESS J1614−518 is also not well explained by a pulsar in this region. These sources may be

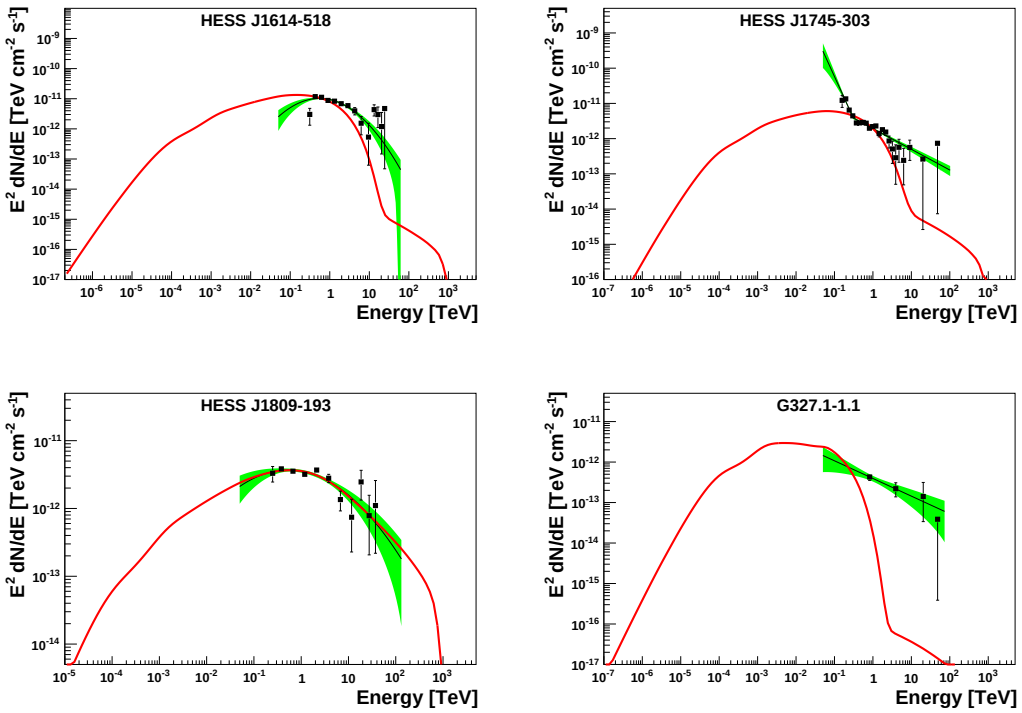

Figure 6.8.: Some spectral energy distributions of the sample of PWN candidates are shown. The sources are HESS J1614–518 (top, left), HESS J1745–303 (top, right), HESS J1809−193 (bottom, left) and G327.1−1.1 (bottom, right). Marked in green is the $1\,\sigma$ confidence interval of the spectral analysis. The black line represents the fitted spectral model. Derived by the method of forward folding the data points are shown in black squares. The theoretical shape provided by the model is depicted in red.

PWNe with more extreme start values, e.g. $P_0 < 5\,\mathrm{ms}$. Additionally, the distance estimate of the associated pulsars provided by radio data could contain large errors. A more obvious scenario is that other types of energy sources (e.g. molecular clouds or unresolved supernova remnants) are responsible for the observed emissions. Searching for counterparts in other wavelengths will allow further investigations.

The same energetic lepton population is assumed to be responsible for synchrotron radiation and Inverse Compton emission from a PWN. Therefore the simulated lepton spectrum allows to compute lower energy photons from the synchrotron component, too. This was included in the model following Blumenthal & Gould (1970). A first try to compare the synchrotron flux with the measured data is applied for the source HESS J1747−281 (G0.9+0.1). The X-ray, data taken by the XMM-Newton Satellite, was provided by Holler et al. (in prep.). Fig. 6.9 reveals that the modeled synchrotron flux has another spectral shape than the measured one. This might be an effect of the chosen energy range of the leptons. Extending the particle spectra to lower energies would cause a harder synchrotron spectrum of photons with a spectral index smaller than 2. Nevertheless, the model reproduces the measured order of magnitude of the flux quite well with the fitted parameters, though they were only optimized

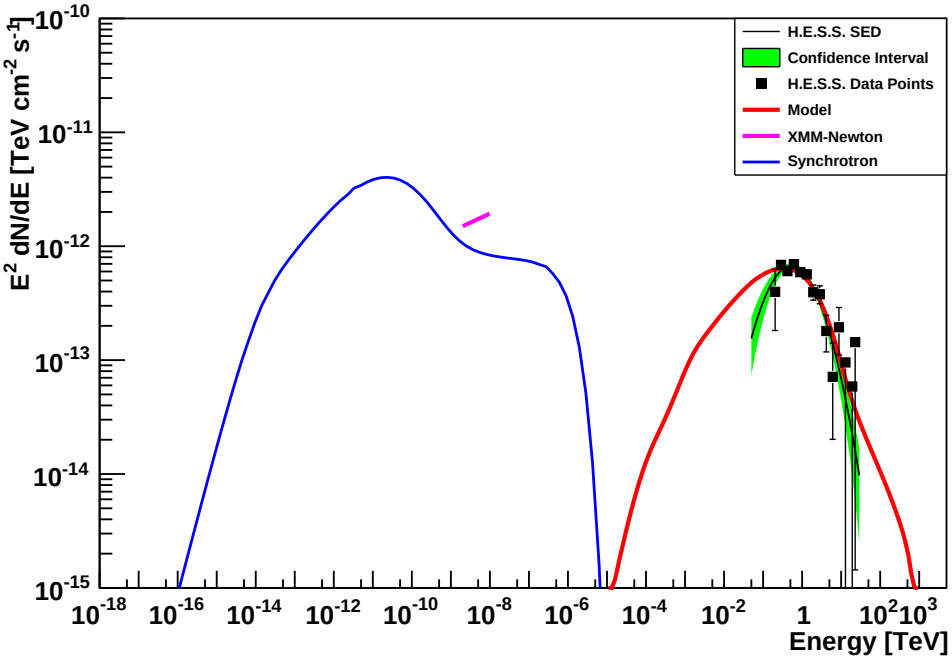

Figure 6.9.: The spectral energy distribution of the source HESS J1747−281 also called G0.9+0.1. Shown in blue is the modeled X-ray emission of the PWN. The purple line represents the spectral energy distribution measured by the XMM-Newton Satellite within $[2, 10]$ keV. X-ray data was provided by Holler et al. (in prep.).

to the VHE γ-rays. Indeed the model might have several good fitting parameter combinations which describe the X-ray and the γ-ray flux properly. For instance, another set of parameters with a different magnetic field might reproduce the measured VHE flux as well as the X-ray emission more accurately. Therefore parameters fitted by the model to VHE data can not be used as physical facts but only as suggested scenarios. More reasonable results can be obtained by fitting the model to X-ray data, too. The hump at about 10 eV is an effect of low energy relic electrons. To explain such a shape of the spectral energy distribution and also the hump in the VHE regime (as seen in Fig. 5.4) current dynamical models of PWNe introduce more complex scenarios. Venter & de Jager (2007) assumed an additional power-law component of leptons with another spectral index. However, Spitkovsky (2008) simulated a maxwell distribution of low energy particles with a power law component containing an exponential cut off of high energy leptons to explain the abovementioned humps. The model described in this thesis obtains similar results with a much simpler approach, e.g. a single lepton population.

Several results produced by the model have been shown in the previous Sections. The model has been established to reproduce VHE spectra of PWNe in a quite efficient way. Obviously, there are several good fitting parameter combinations. The fitted values can be considered as one possible solution to explain the emission in the H. E. S. S. energy range. The information provided by the fit can be used to make predictions for the future development of PWNe.

6.3. Model predictions

Based on model simulations, this Section tries to explain some of the measured PWN parameters shown in Chap. 4. As mentioned in Sect. 5.1 the model can simulate the photon spectrum beyond the true age. Illustrated in Fig. 5.1, the amount of leptons is increasing for a young pulsar. After some 10 kyr the relativistic particles are dominated by the cooling effects. Thus a young PWN is expected to increase its luminosity in the VHE regime steadily followed by a slow decrease after about 10 kyr. To visualize the predictions the sources HESS

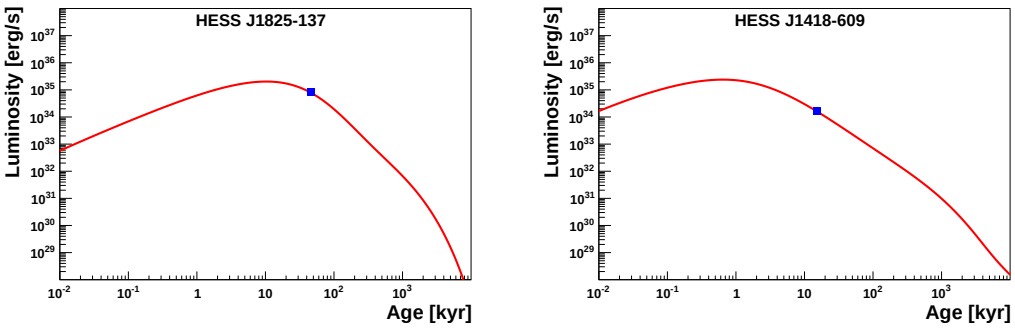

Figure 6.10.: The evolution of the luminosity of the PWN. The development of this value for HESS J1825−137 is shown left. The PWN HESS J1418−609 and its evolution simulated by the model is plotted right. The blue points represent the current measured value of the respective source.

J1825−137 (see Fig. 6.4) and HESS J1418−609 serve as example. They represent different types of spectral evolution for all PWNe. The model fitted the spectral energy distributions of both sources quite well ($\chi^2_{\mathrm{red}} \approx 3.2$ and $\chi^2_{\mathrm{red}} \approx 0.5$, respectively). The simulated evolution of the luminosities of these PWNe is shown in Fig. 6.10, including the current values for the luminosity measured with the H. E. S. S. experiment. The luminosity of each source is supposed to follow the different extrapolated evolution of the luminosity with time. A reason for the different shapes of this evolution between the individual PWNe is the initial spin-down timescale calculated by the model. This value affects the spin-down evolution of the pulsar influencing the energy output.

The time-dependent spin-down luminosity $\dot{E}(t)$ is compared to the simulated luminosity $L_\gamma(t)$ for both sources in Fig. 6.11. After a certain age, which is different for each considered source, $L_\gamma(t)$ exceeds $\dot{E}(t)$. This results in an efficiency ϵ larger than 100 % which was usually thought to be unrealistic for a PWN. But relic leptons in high numbers can contribute to the old Pulsar Wind. Therefore the efficiency seems significantly higher. After some time in this evolutionary state ($\epsilon > 1$), $L_\gamma(t)$ decreases rapidly by falling again below $\dot{E}(t)$. All relic particles are cooled and only newly injected particles ($\propto \dot{E}(t)$) dominate the spectrum. This evolutionary state, however, can not be seen by H. E. S. S. or any other IACT with similar sensitivity because the luminosity has then already fallen far below the detection threshold. H. E. S. S. can detect a source with a flux of 1 % of the Crab Nebula within 25 h, assuming a zenith angle of 90°, with a significance of 5 σ. In order to have a rough estimate of the detection threshold, it was assumed that the energy flux of the source must be 1 % of the Crab

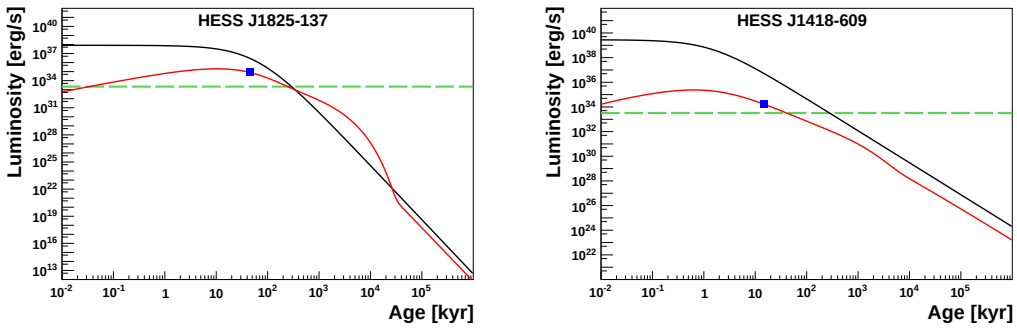

Figure 6.11.: The evolution of the luminosity of the PWNe (red) compared to their corresponding spin-down luminosity (black). HESS J1825–137 (left) shows a point of intersection of the spin-down luminosity and the source luminosity while HESS J1418–609 (right) does not. The approximated detection threshold of H. E. S. S. is represented by a green dashed line. Note: The scale of the luminosity axis is different for both sources.

Nebula in $[0.5, 5]$ TeV. However this threshold must be treated with reserve, as it neglects different spectral shapes and thus different effective areas. Scaled by the distance a universal luminosity threshold can be approximated. The efficiency must, as the luminosity, also evolve with time.

$$\epsilon(t) = \frac{L_\gamma(t)}{\dot{E}(t)}. \tag{6.2}$$

Model calculations for this value are depicted in Fig. 6.12. Both sources show a steady in-

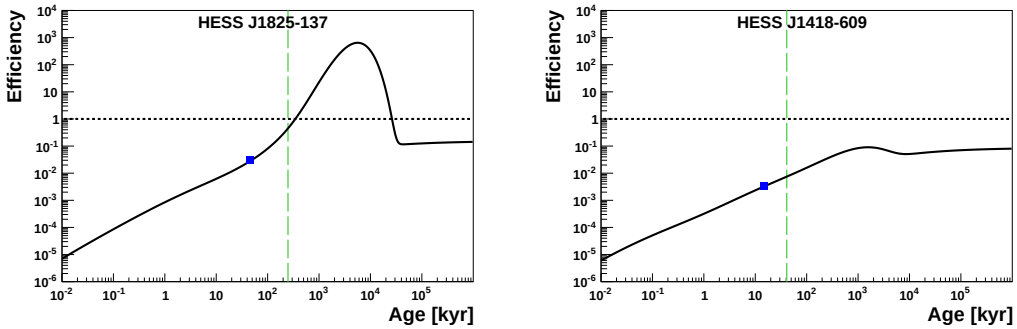

Figure 6.12.: The time-dependent efficiency of two PWNe HESS J1825−137 (left) and HESS J11418−609 (right). The latter source will not exceed 100 %. The blue points show the current efficiency of the two PWNe in this example. Marked with a long-dashed line (green) is the time when the respective source disappears below the H. E. S. S. detection threshold. An efficiency of 100 % is shown by the black-dotted line.

crease of the efficiency with time. HESS J1825−137 exceeds the value of 100 % after about 200 kyr with a peak at $5 \cdot 10^3$ kyr. The PWN HESS J1418–609 shows a similar shape reaching

its peak efficiency already after $1 \cdot 10^3$kyr. But the latter source will not exceed a value of 100 %. Consequently a high value of the efficiency is not predicted for every source. That depends on the initial parameters which affect the energy output. After about 10^4 kyr the efficiency stays constant with time for both sources. If there are no more relic leptons left inside the PWN and only the fresh injected particles dominate the particle spectrum, the efficiency corresponds to the parameter η of the model. A future experiment with a sensitivity similar to H. E. S. S. could detect HESS J1825−137 until its efficiency reaches approximately 100 %. Afterwards the source luminosity is too low to lead to a significant signal after usual observation times. HESS J1418−609 can be seen until a true age of about 40 kyr, i.e. this source will be visible for the next 25 kyr.

This Section gave an overview of the possible calculations of the model. The simulations are capable of computing spectral evolution for extreme high ages. Thus the behavior of some parameters, e.g. the luminosity of a PWN in the future, can be described by the model. Based on two examples of bright PWNe the temporal development of the conversion efficiency from spin-down luminosity to VHE emission was shown in detail. Remarkably, this value can exceed 100 % in specific cases. Thus a PWN scenario can not be excluded for some unidentified sources detected with H. E. S. S. featuring this attribute. The next Section tries to establish a connection between the PWN candidates of the sample and the already identified PWN.

6.4. Trends for the source type determination

The results of the modeling of several sources of the whole sample have been presented in this Chapter. The model introduced in Chap. 5 proved to be capable to describe the measured VHE emission of many PWNe quite well. However, some spectra of the PWN candidates could not be reproduced. Already identified PWNe allow to constrain the properties of sources which are suggested to be powered by a pulsar. Considering the evolutions of the efficiencies of all PWNe allow conclusions about the possible values of this parameter. Fig. 6.13 shows all PWNe and their time-dependent efficiency. Superimposed are the current values of PWN and PWN candidates. The inferred efficiencies for all PWN candidates lie in the range accessible for this model. According to the model prediction also the highest measured efficiency of $\epsilon \approx 120$ for G327.1−1.1 might be realistic for a specific set of model parameters. A PWN scenario can not be excluded for all sources of the sample considering this simulated evolution of efficiency. The source luminosity is also compared to the current values of the PWN candidates. Fig. 6.14 reveals three PWN candidates which are brighter than explained by the PWN population. These VHE sources are HESS J1503−582, HESS J1614−518 and G327.1−1.1. The PWN candidate HESS J1745−303 is also reaching the boundaries of the possible PWN luminosities. Most of the fitted parameters of these sources reached their definition limit indicated by high values of χ^2_{red}. Assuming the model to be a good approximation of PWNe of different evolutionary states, a PWN scenario of this sources is at least questionable. Compared to Fig. 4.7, the radius of G327.1−1.1 is smaller than the rest of the population ($R_{\mathrm{G327.1}} \approx 1\,\mathrm{pc}$). Possibly the visible part of a PWN decreases again with age for old pulsars. Investigating the spectral energy distribution of this source shown in Fig. 6.8 reveals that the model is not able to reproduce the spectral shape of that source. Either the model does not consider physical relevant processes for an old PWN or a PWN scenario is excluded and the possible origins of the source can be constrained. Nevertheless, a recently

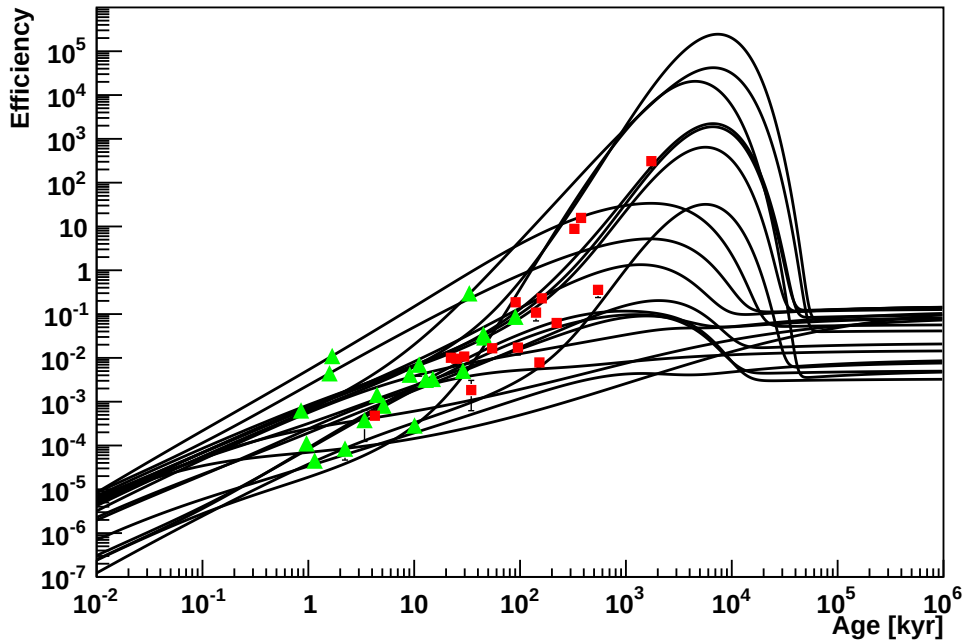

Figure 6.13.: Possible values of the efficiency of all 19 identified PWN. The black lines show the evolution of this parameter with respect to the single PWN. Green triangles are current efficiencies of PWNe, while the red squares represent the PWN candidates at their simulated true ages.

detected X-ray nebula in the source region (Slane 2010) in turn, gives rise to a possible PWN origin. Another pulsar, closer to the Earth, which is located in front of PSR J1554 − 5512 may be responsible for the emission. Probably, its light cone does not sweep across the Earth and therefore it was not detected by radio surveys. The spectra of the candidates HESS J1614−518 and HESS J1745−303 are also not reproduced properly ($\chi^2_{\mathrm{red}} \approx 13$ and $\chi^2_{\mathrm{red}} \approx 22$, respectively). Other parameters of both sources, e.g. radius or efficiency, do not differ significantly from the rest of the population. Due to model calculations only, a PWN scenario can not be excluded for both sources. For the rest of the population of PWN candidates the model and the measured parameters fit well into the scheme of already identified PWNe. Thus a PWN scenario is quite possible for most of the candidates. Further investigations and more detailed observations providing statistically significant data are required for clearer identifications.

A detailed review of the results produced by the model was given in this Chapter. Some spectral evolutions of PWNe could be well reconstructed. Further simulations for future predictions were also presented in Sect. 6.3. The model calculations revealed evidence for possible efficiencies larger than 100 % generated by a large contribution of relic leptons to the particle spectrum. Finally PWN candidates were compared to the identified PWNe in order to get evidence for the source origin. For three sources the possibility of a PWN scenario decreased based on model calculations. Especially G327.1 − 1.1 is difficult to connect with the PWN population due to its high age and its spectral appearance. As discussed, a wrong

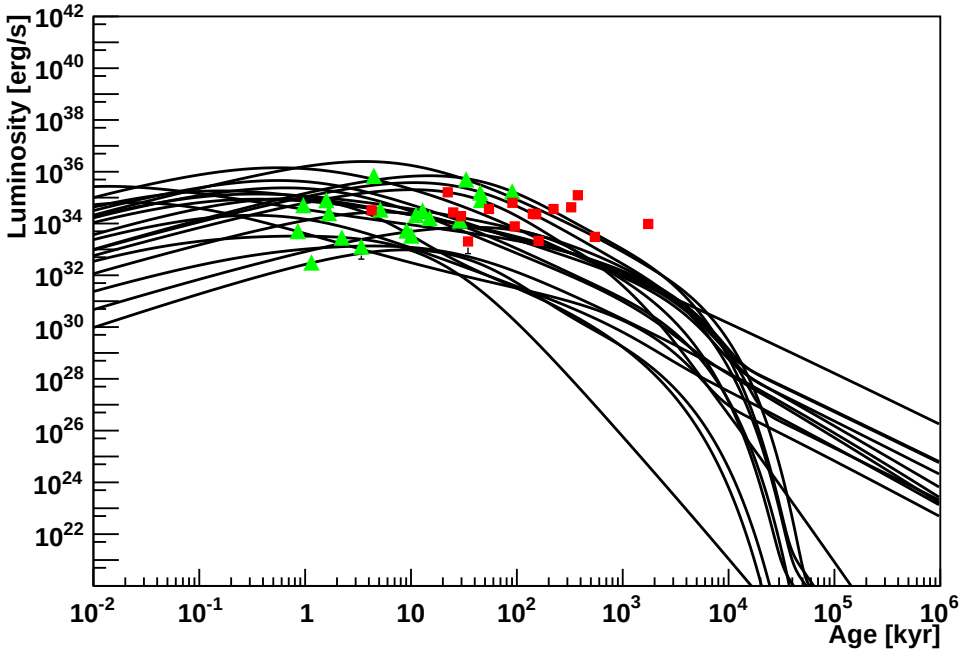

Figure 6.14.: The black solid lines show the possible evolution of identified PWNe. Superimposed in red and green are the current values of the PWN candidates and PWNe, respectively.

pulsar might be considered in this case. All results should be interpreted carefully. The model is a simple try to explain the spectral evolution of PWN and can not reflect reality in detail. Consequently there is no clear evidence to reject a PWN scenario for some candidates.

7. Summary and outlook

This thesis presented a detailed study of the whole population of PWNe in the VHE regime. After introducing pulsars as accelerators of relativistic particles, the origin of non-thermal radiation from their vicinity was discussed. The data analyzed in this work was taken by the H. E. S. S. telescopes. A brief summary of the detection technique of this experiment was presented, followed by the methods of data analysis used in this thesis. Subsequently the analysis results for every considered PWN and PWN candidate were presented and evaluated. The properties and the temporal evolution of pulsars which generate observable VHE nebulae were investigated in detail. Afterwards, to improve the understanding of the PWN population, a simple one-zone model of the spectral evolution of a PWN was introduced. Based on this model, further investigations on the sample of PWN and PWN candidates were performed.

All known pulsars show evidence for a spin-down evolution. Investigating the type of pulsars, that are able to generate TeV nebulae, it becomes clear that only the most energetic pulsars are able to produce detectable emission. Additionally these pulsars must have a small period as well as a high period derivative. Due to interactions with the SNR Reverse Shock, the free expansion of a PWN is constrained to about 10 kyr. No evidence for a change of the spectral shape is given by the sample. The conversion efficiency from spin-down energy to VHE γ-rays however, emerged to increase with time. Simulating the spectral evolution and understanding the temporal behavior of characteristic parameters of a PWN resulted in a time-dependent one-zone model (Chap. 5). It proved to be suitable to describe several photon spectra of PWNe precisely. To produce general results, the model and its calculation precision have to be independent from parameter influences. Therefore a method of adaptive binning was developed which allows fast computation with best possible accuracy. The model was fitted to the spectra measured by the H. E. S. S.experiment. The results for every PWN and PWN candidate were shown in Chap. 6. Several spectral energy distributions of well and also of badly fitting sources were investigated. The Crab Nebula in particular revealed the missing SSC component in the model. The X-ray flux of the synchrotron emission was compared with data from the XMM-Newton Satellite for the PWN HESS J1747−281. The model is able to reproduce the order of magnitude of the X-ray emission but its shape is not well described. Simulations of the future development of a PWN resulted in an efficiency exceeding 100 % for some of these objects. Thus a smaller value is not a criterion for a source to be powered by a pulsar. Finally the PWN scenario of some PWN candidates was questioned. Differing from the rest of the population, HESS J1503−582, HESS J1614−518, HESS J1745−303 and G327.1−1.1 do not fit well to the model simulations. However, no source can be excluded to originate from a pulsar.

More than six years of data-taking with H. E. S. S. allow population studies on this particular source class. However, due to low γ-ray fluxes the measurements of many PWNe in the VHE regime are statistically limited. Larger detectors, more sensitive in a broader energy range are planned for the future. The Cherenkov Telescope Array (CTA) will discover a large

number of PWNe emitting VHE γ-rays which allow to enhance these studies. A further step in the development of the model is be to include morphological evolutions, too. For a further constraint on the model parameters it is necessary to investigate X-ray emission of the PWNe in detail. The synchrotron cut off allows to draw conclusions about the present magnetic field inside the PWN and also on the maximum energy of leptons. A general view on the multi-wavelength spectra of PWNe enables to fit the spectra more properly with enhanced physical significance of the parameters.

A. Spectral energy distribution of the rest of the population

In the following all analyzed sources with the respective spectral energy distribution (SED) are illustrated. Already showed SEDs are omitted. Every image is superimposed by the respective model simulation for the source.

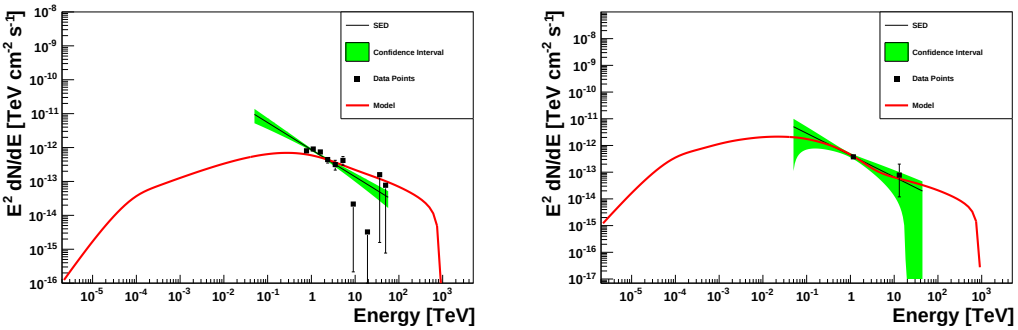

Figure A.1.: SED for HESS J0536−691 (left) and HESS J1018−589 (right).

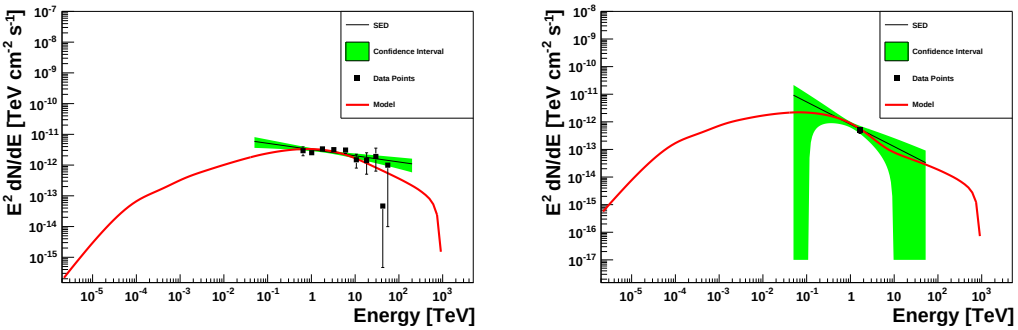

Figure A.2.: SED for HESS J1356−645 (left) and HESS J1406−613 (right).

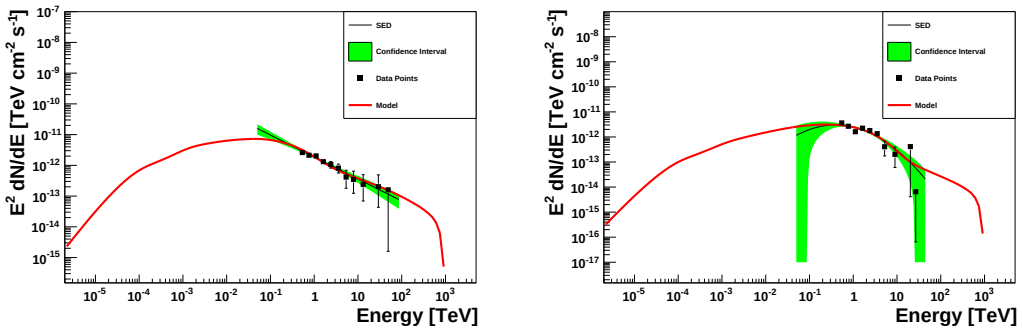

Figure A.3.: SED for HESS J1418−609 (left) and HESS J1420−607 (right).

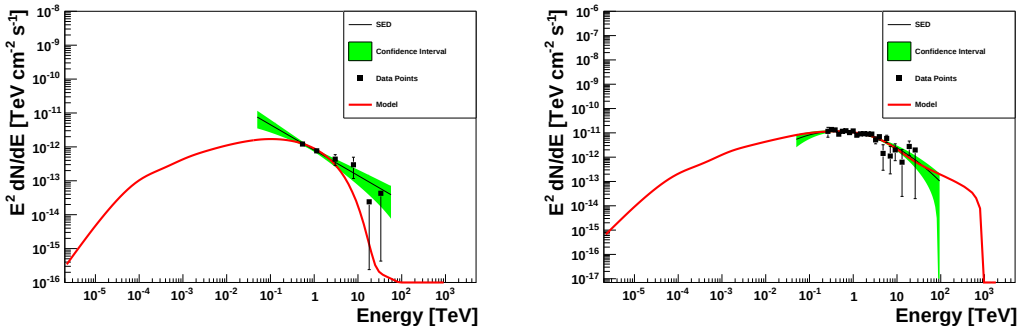

Figure A.4.: SED for HESS J1503−582 (left) and HESS J1616−508 (right).

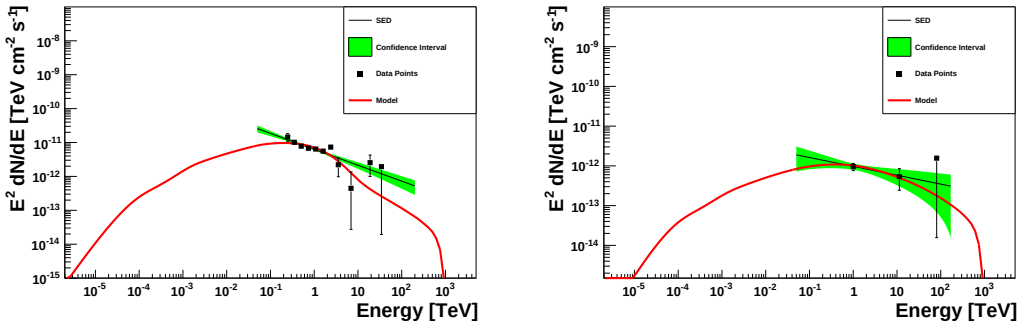

Figure A.5.: SED for HESS J1702−420 (left) and HESS J1708−443 (right).

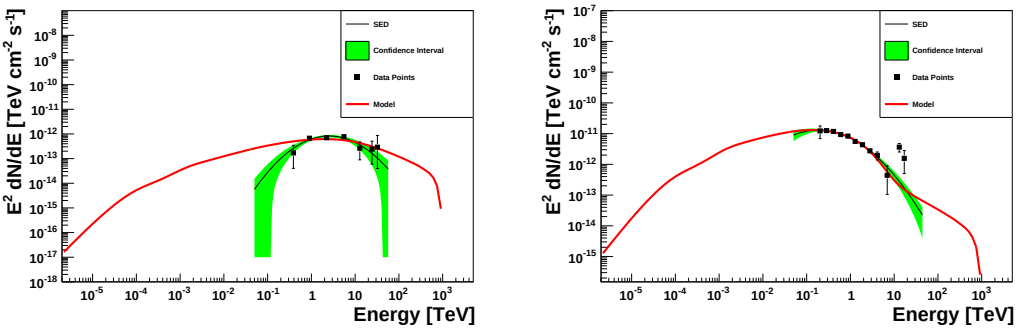

Figure A.6.: SED for HESS J1718−385 (left) and HESS J1804−216 (right).

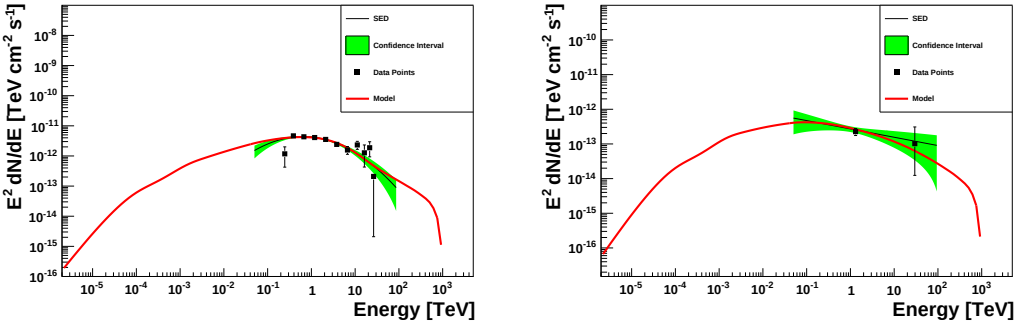

Figure A.7.: SED for HESS J1813−178 (left) and HESS J1831−095 (right).

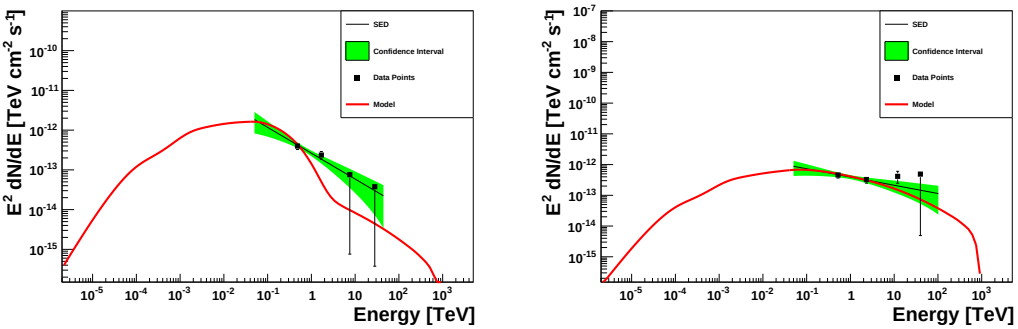

Figure A.8.: SED for HESS J1832−084 (left) and HESS J1833−105 (right).

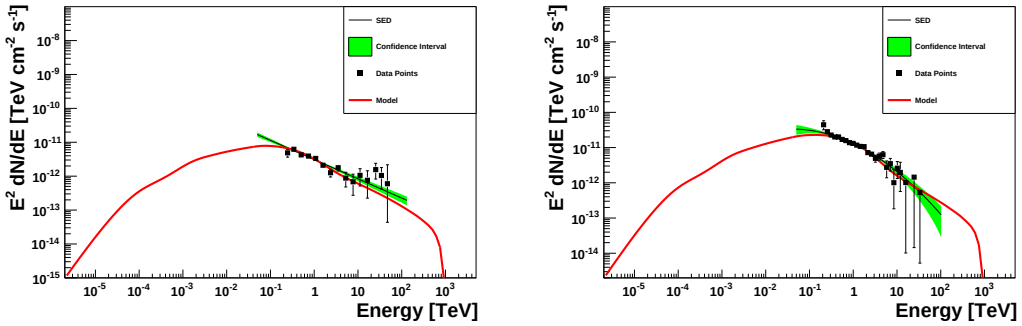

Figure A.9.: SED for HESS J1834−087 (left) and HESS J1837−069 (right).

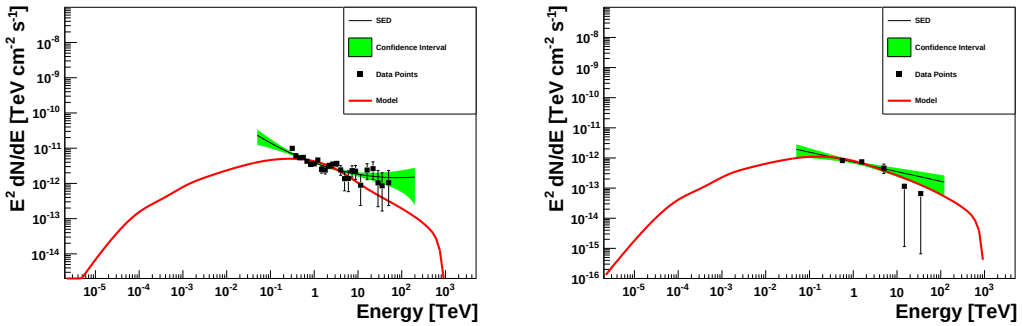

Figure A.10.: SED for HESS J1857 + 026 (left) and HESS J1858 + 020 (right).

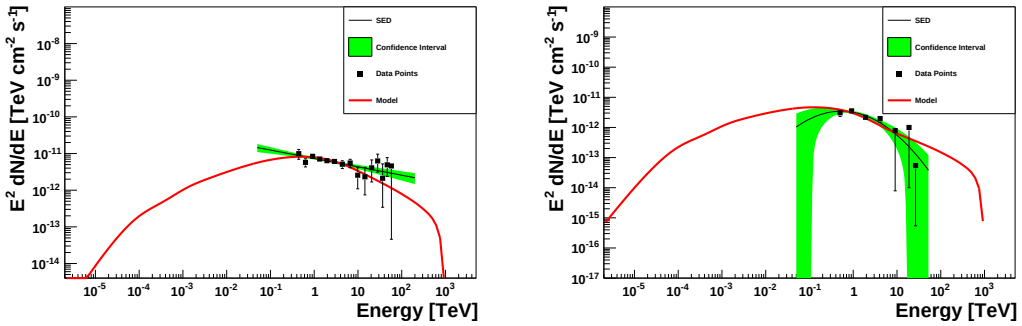

Figure A.11.: SED for HESS J1908 + 063 (left) and HESS J1912 + 101 (right).

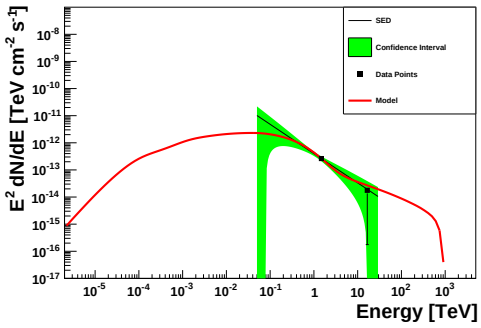

Figure A.12.: SED for HESS J1930 + 186.

B. Distribution of model parameters

Some distributions, not shown in the text, are illustrated subsequently.

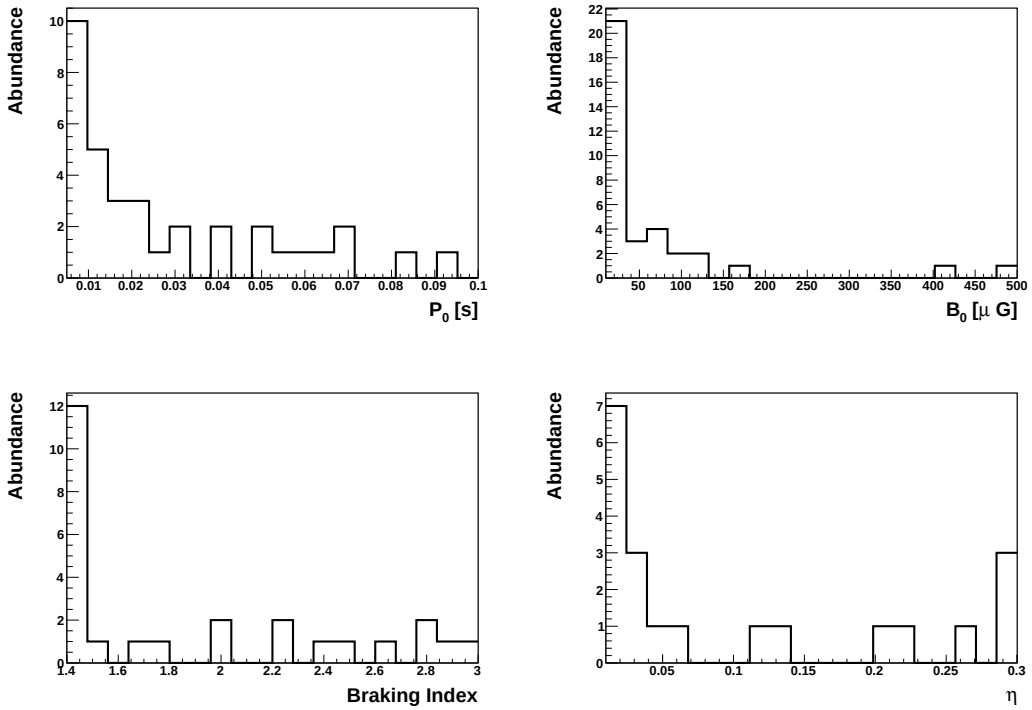

Figure B.1.: The upper left panel shows the distribution of the fitted initial periods. The initial magnetic field is shown on the upper right. The fitted braking indices are shown in the lower left panel while the abundance of the conversion efficiencies is depicted in the lower right panel.

List of Figures

List of Tables

Bibliography

Acciari, V. A., Aliu, E., Arlen, T., et al. 2010, ApJ, 719, L69

Aharonian, F., Akhperjanian, A. G., Aye, K., et al. 2005a, Science, 307, 1938

Aharonian, F., Akhperjanian, A. G., Aye, K., et al. 2005b, A&A, 439, 1013

Aharonian, F., Akhperjanian, A. G., Aye, K., et al. 2005c, A&A, 435, L17

Aharonian, F., Akhperjanian, A. G., Bazer-Bachi, A. R., et al. 2007, A&A, 472, 489

Aharonian, F., Akhperjanian, A. G., Bazer-Bachi, A. R., et al. 2006a, A&A, 457, 899

Aharonian, F., Akhperjanian, A. G., Bazer-Bachi, A. R., et al. 2006b, A&A, 448, L43

Aharonian, F., Akhperjanian, A. G., Bazer-Bachi, A. R., et al. 2006c, ApJ, 636, 777

Aharonian, F., Akhperjanian, A. G., Bazer-Bachi, A. R., et al. 2006d, A&A, 460, 365

Aharonian, F., Akhperjanian, A. G., Bazer-Bachi, A. R., et al. 2006e, A&A, 456, 245

Baade, W. & Zwicky, F. 1934, Phys. Rev., 46, 76

Balzer, A. 2010, Diploma thesis, Friedrich-Alexander-Universität, Erlangen, Germany

Berge, D. 2006, Dissertation, Ruprecht-Karls-Universität, Heidelberg, Germany

Berge, D., Funk, S., & Hinton, J. 2007, A&A, 466, 1219

Bernlöhr, K. 2010, Monte-Carlo Images of Air Showers, Website, `http://www.mpi-hd.mpg.de/hfm/~bernlohr/HESS/MC_images/`

Blondin, J. M., Chevalier, R. A., & Frierson, D. M. 2001, ApJ, 563, 806

Blumenthal, G. R. & Gould, R. J. 1970, Reviews of Modern Physics, 42, 237

Brucker, J. in prep., Dissertation, Friedrich-Alexander-Universität, Erlangen, Germany

Camilo, F., Gaensler, B. M., Gotthelf, E. V., Halpern, J. P., & Manchester, R. N. 2004, ApJ, 616, 1118

Camilo, F., Kaspi, V. M., Lyne, A. G., et al. 2000, ApJ, 541, 367

Carrigan, S. 2007, Dissertation, Ruprecht-Karls-Universität, Heidelberg, Germany

Chandrasekhar, S. 1931, ApJ, 74, 81

Chaves, R. & Djannati-Atai, A. in prep.

Chevalier, R. A. 1977, in Astrophysics and Space Science Library, Vol. 66, Supernovae, ed. D. N. Schramm, 53–+

de Jager, O. C. & Djannati-Ataï, A. 2009, Neutron Stars and Pulsars, ASSL 357, Springer, ed. Becker, W., 451

de Naurois, M. 2010, Internal Documentation, Website

de Naurois, M. & Rolland, L. 2009, Astroparticle Physics, 32, 231

Djannati-Ataĭ, A., de Jager, O. C., Terrier, R., & et al. 2008, in International Cosmic Ray Conference, Vol. 2, International Cosmic Ray Conference, 823–826

Fermi, E. 1949, Phys. Rev., 75, 1169

Funk, S. 2005, Dissertation, Ruprecht-Karls-Universität, Heidelberg, Germany

Gaensler, B. M. & Slane, P. O. 2006, ARA&A, 44, 17

Göring, D. 2008, Diploma thesis, Friedrich-Alexander-Universität, Erlangen, Germany

Gotthelf, E. V. & Halpern, J. P. 2008, ApJ, 681, 515

Hessels, J. W. T., Nice, D. J., Gaensler, B. M., et al. 2008, ApJ, 682, L41

Hewish, A., Bell, S. J., Pilkington, J. D. H., Scott, P. F., & Collins, R. A. 1968, Nature, 217, 709

Hinton, J. A. & Hofmann, W. 2009, ARA&A, 47, 523

Holler, M., Eger, P., Kiessling, D., Schöck, F. M., & Stegmann, C. in prep., in preparation

Hoppe, S., de Oña-Wilhemi, E., Khélifi, B., et al. 2009, ArXiv e-prints

Horns, D. & Aharonian, F. A. 2004, in ESA Special Publication, Vol. 552, 5th INTEGRAL Workshop on the INTEGRAL Universe, ed. V. Schoenfelder, G. Lichti, & C. Winkler, 439–+

Kargaltsev, O. & Pavlov, G. G. 2010, in American Institute of Physics Conference Series, Vol. 1248, American Institute of Physics Conference Series, ed. A. Comastri, L. Angelini, & M. Cappi, 25–28

Kaspi, V. M., Manchester, R. N., Siegman, B., Johnston, S., & Lyne, A. G. 1994, ApJ, 422, L83

Klein, O. & Nishina, T. 1929, Zeitschrift für Physik, 52, 853

Livingstone, M. A., Kaspi, V. M., Gotthelf, E. V., & Kuiper, L. 2006, ApJ, 647, 1286

Lyne, A. G. & Graham-Smith, F. 2006, Pulsar Astronomy, ed. Lyne, A. G. & Graham-Smith, F.

Lyne, A. G., Pritchard, R. S., Graham-Smith, F., & Camilo, F. 1996, Nature, 381, 497

Lyne, A. G., Pritchard, R. S., & Smith, F. G. 1988, MNRAS, 233, 667

Manchester, R. N., Hobbs, G. B., Teoh, A., & Hobbs, M. 2005, VizieR Online Data Catalog, 7245, 0

Porter, T. A. & Strong, A. W. 2005, in International Cosmic Ray Conference, Vol. 4, International Cosmic Ray Conference, 77

Qiao, W., Zhang, L., & Fang, J. 2009, Research in Astronomy and Astrophysics, 9, 449

Slane, P. 2010, ArXiv e-prints

Spitkovsky, A. 2008, ApJ, 682, L5

Strong, A. W., Moskalenko, I. V., & Reimer, O. 2000, ApJ, 537, 763

van der Swaluw, E., Achterberg, A., Gallant, Y. A., & Tóth, G. 2001, A&A, 380, 309

Venter, C. & de Jager, O. C. 2007, in WE-Heraeus Seminar on Neutron Stars and Pulsars 40 years after the Discovery, ed. W. Becker & H. H. Huang, 40–+

Zhang, L., Chen, S. B., & Fang, J. 2008, ApJ, 676, 1210

Acknowledgement/Danksagung

"Nichts beflügelt die Wissenschaft so, wie der Schwatz mit Kollegen auf dem Flur."
Arno Penzias (amerikanischer Physiker)

Diese letzte Seite möchte ich nutzen, um allen zu danken, die mich während des letzten Jahres im Büro und auch auf dem Flur tatkräftig unterstützt haben.

Mein erster Dank gilt Prof. Dr. Christian Stegmann. Mit motivierenden Ratschlägen und zwei offenen Ohren für meine Anliegen, hat er mir immer wieder neue Anregungen und nicht zu letzt ein interessantes und vielsprechendes Thema gegeben, das mich nach wie vor begeistert.

Julia Brucker hat mir mit guter Betreuung und einer besonders aufmerksamen Korrektur zur Seite gestanden. Ich danke ihr für das vermittelte know-how, ein PWN-Modell anzufertigen. Außerdem hat sie einen wesentlichen Teil zum - vor allem sprachlichen - Erscheinungsbild der Diplomarbeit beigetragen.

Ich danke Peter Eger für den besonderen Einsatz und die konstruktive Kritik, um meine Diplomarbeit in eine lesbare Form zu bringen. Vor allem Mittagspausen und Kollaborationsmeetings wurden durch seine humorvolle Art bereichert und "durch- bzw. neigwuchtet".

Desweitern möchte ich mich bei Dr. Kathrin Valerius für ihr besonderes Engagement bedanken, welches sie weder vor dem fehlerhaften Spektrummodul der Paris Analyse, noch vor nächtlichen Korrekturen zurückschrecken ließ.

Markus Holler hat mir die Augen für das niederenergetische Universum geöffnet und mich menschlich, sowie fachlich unterstützt, Jawoi! Ihm, wie auch Neli, Steffi und Anton danke ich für die angenehme Büroatmosphäre.

Ich danke der gesamten Erlanger H. E. S. S.-Gruppe, für die netten Kaffee-, Tee- und Kuchenpausen, die die Pulsarwindnebel für kurze Zeit gelichtet haben.

Zu guter letzt gilt mein größter Dank meiner Freundin Bine, die mich das ganze Jahr über bei Laune gehalten hat. Bei ihr konnte ich neue Kraft tanken und meine Zeit außerhalb vom Institut genießen.

Erklärung

Ich bestätige hiermit, dass ich die vorliegende Diplomarbeit selbständig verfasst und keine anderen als die angegebenen Quellen und Hilfsmittel verwendet habe.

Erlangen, den 1. Dezember 2010